

# Numerical Assessment of the Residual Stress Formation in Rotary Friction Welding

---

Dissertation  
zur Erlangung des akademischen Grades

**Doktoringenieur (Dr.-Ing.)**

von M. Sc. Christoph Rößler  
geboren am 27. Januar 1992 in Haldensleben

genehmigt durch die Fakultät für Maschinenbau  
der Otto-von-Guericke-Universität Magdeburg

Gutachter:  
Prof. Dr.-Ing. Elmar Woschke  
Prof. Dr.-Ing. habil. Thorsten Halle

Promotionskolloquium am 10. Mai 2023



# Abstract

The present work addresses the estimation of residual stresses in rotary friction welded components using a structural simulation. The starting point is a process simulation for friction welding, which has been elaborated in prior works to predict the temperatures and the material flow. This model is unsuitable for residual stress predictions, however, due to its underlying material model among other reasons. Therefore, the material simulation is a major focus of this work. Because of their wide use in friction welding applications, the focus shall be on steels. In this work, a practical parameterization for a phenomenological phase transformation model is proposed and the flow properties of the material are derived based on the phase transformation points. The predicted phase transformations are validated by hardness measurements, and the flow properties by non-isothermal hot tensile testing. The developed model is capable of reproducing various examples and phenomena from literature and from industrial applications that are associated with high residual stresses. In addition, general recommendations for a residual stress compliant design have been derived.

*Die vorliegende Arbeit befasst sich mit der Abschätzung der Eigenspannungen in reibgeschweißten Bauteilen mithilfe einer Struktursimulation. Den Ausgangspunkt bildet eine Prozesssimulation für das Reibschweißen, welche in vorangegangenen Arbeiten entwickelt worden ist, um die Temperaturen und den Materialfluss zu prädictieren. Unter anderem durch das zugrundeliegende Materialmodell ist diese jedoch zur Eigenspannungsvorhersage ungeeignet, weshalb die Materialsimulation einen wesentlichen Arbeitsschwerpunkt darstellt. Angesichts der hohen industriellen Verbreitung liegt der Fokus hier auf Stählen. In der Arbeit wird eine praktische Parametrisierung für ein phänomenologisches Phasenumwandlungsmodell vorgeschlagen und es werden ausgehend von den Phasenumwandlungspunkten die Fließeigenschaften des Stahls abgeleitet. Die Validierung der prädictierten Phasenumwandlungen erfolgt anhand von Härtemessungen, die der Fließeigenschaften anhand von anisothermen Warmzugversuchen. Das erstellte Modell ist in der Lage verschiedene Beispiele und Phänomene aus der Literatur und Praxis abzubilden, die im Zusammenhang mit hohen Eigenspannungen stehen. Darüber hinaus sind allgemeine Empfehlungen für eine eigenspannungsgerechte Gestaltung abgeleitet worden.*





---

# Contents

<b>1</b>	<b>Introduction</b>	<b>1</b>
1.1	Aims and objectives . . . . .	2
1.2	Scope . . . . .	3
1.3	Outline . . . . .	3
<b>2</b>	<b>State of the art</b>	<b>5</b>
2.1	Rotary friction welding . . . . .	5
2.1.1	Process stages . . . . .	7
2.1.2	Process simulation . . . . .	9
2.2	Residual stresses . . . . .	12
2.2.1	Measurement methods . . . . .	12
2.2.2	Rotary friction welding investigations . . . . .	14
2.3	Material modeling . . . . .	16
2.3.1	Microstructural transformations . . . . .	16
2.3.2	Hardening . . . . .	19
2.4	Need for further research . . . . .	22
<b>3</b>	<b>Simulation model</b>	<b>25</b>
3.1	Material simulation . . . . .	25
3.1.1	Microstructural transformations . . . . .	25
3.1.2	Consistently-assessed Carreau fluid model . . . . .	33
3.1.3	Transformation hardening . . . . .	35
3.1.4	Elastoplasticity . . . . .	36
3.2	Finite element modeling . . . . .	42
3.2.1	Small displacements . . . . .	42
3.2.2	Principle of virtual displacements . . . . .	43
3.2.3	Element formulation . . . . .	44
3.2.4	Contacts and bonding . . . . .	45
3.2.5	Solver and time integration . . . . .	49

<b>4</b>	<b>Material examination</b>	<b>51</b>
4.1	Hardness measurements in welds . . . . .	52
4.2	Uniaxial tensile testing . . . . .	57
4.2.1	Full heating and cooling evaluation . . . . .	60
4.2.2	Approximated cooling evaluation . . . . .	63
<b>5</b>	<b>Application cases</b>	<b>65</b>
5.1	Overlap friction welding . . . . .	65
5.1.1	Overlap friction welding of sheets . . . . .	67
5.1.2	Planetary carrier . . . . .	71
5.2	Heat throttle design . . . . .	73
5.2.1	Constant velocity joint . . . . .	73
5.2.2	Hybrid brake disc . . . . .	80
5.3	Hybrid welds . . . . .	85
5.3.1	Welding of Al-Fe alloy rods . . . . .	85
5.3.2	Lightweight gear wheel . . . . .	89
5.4	Inertia friction welding of large rings . . . . .	92
<b>6</b>	<b>Conclusion</b>	<b>97</b>
6.1	Added value to the RFW simulation . . . . .	97
6.2	Guidelines for residual stress compliance . . . . .	98
6.3	Outlook . . . . .	98

# 1 Introduction

The present work is intended to contribute to a better understanding of the residual stress phenomena in rotary friction welding (RFW). RFW is prone to cause residual stresses, being a solid-state welding process that utilizes frictional heat generated by performing a relative movement while applying an axial force.

RFW is used for the manufacturing of reproducible, high-quality joints at large-scale, including automotive and aviation applications for instance. Especially in the powertrain of modern vehicles a high number of components is friction welded, like pistons or drive shafts, but also components like airbag inflators and seat belt tensioners. Although technical guidelines for RFW by the German Welding Society (DVS) exist, those can understandably not cover all possible application cases. To be more precise, the guidelines for RFW are limited to shafts and tubes made of the same alloy. Forced by the demand for lighter components that carry higher loads at the same time, however, the designs are often more advanced.

The process simulation provides a helpful tool that assists to analyze more complex geometries and material mixes already in early design stages. Schmicker [1] elaborated a RFW process simulation model to predict the temperature field and the material flow in diverse RFW applications, which has been offered for consulting to the industry starting in 2015. Typical tasks include the RFW design for new components and the transfer of the existing RFW solution of one component into a modular system. Other projects are aiming to identify fundamentally different RFW solutions, made possible by the advancements in the RFW machine design among others.

Referring back to the prior statement about advanced designs, components generally tend to become thinner by using stronger materials made by special heat treatments. At the high temperatures in the RFW process, however, the strength advantage of those materials typically vanishes and what remains are fragile structures. This makes the RFW development more challenging, because the RFW process design has to take the product design into account to a greater extent and vice versa. Along with large deformations harming the functional integrity, the occurrence of cracks in the macrographs is a recur-

ring challenge. At times a failure can already be perceived as crackling and cracking in the RFW machine while the components are cooling. A material transfer indicate that a bond must have existed at least temporarily nevertheless, which fails due to the residual stress formation.

Unfortunately, the prediction of residual stresses exceeds the limits of the RFW process simulation model – this is what the following work is intended to resolve.

## 1.1 Aims and objectives

Analogously to the RFW process simulation model, a RFW structural simulation model, which allows for *qualitative predictions of residual stresses* due to RFW, is to be set up, to enhance the design of the RFW process and of the components to be joined.

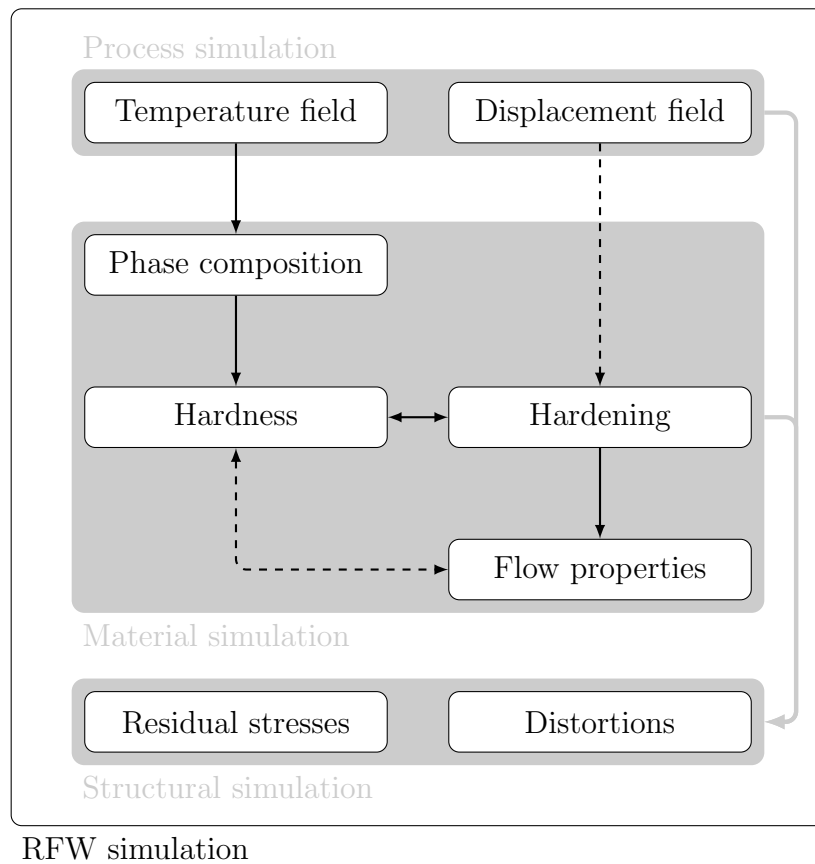


Figure 1: Subdivision of the RFW simulation with the process simulation as the starting point and material and the structural simulation as post-processing steps

---

The RFW structural simulation shall be performed as a post-processing step that takes the temperature and displacement fields from the RFW process simulation as a starting point as illustrated in Figure 1. Within this framework, the ideal viscoplastic material model is converted to an elastoplastic model, extended by the capability to take phase composition changes of steels into account and by linking hardness to flow property changes. Physical interpretability and reasonable complexity of the material model are necessary for its acceptance. Because the resources for material testing in the context of RFW simulations are often restricted, all of the newly introduced model parameters shall be accessible or retrievable from commonly available data.

## 1.2 Scope

The approaches are general, so that they can also be applied to linear or orbital friction welding, for example. The implementation in this work, however, is limited to the RFW process and axisymmetric components.

It is obvious that the RFW material simulation in the scope of this work can not cover all alloys suitable for RFW. The RFW material simulation is therefore tailored for steels, which are requested the most. For non-ferrous alloys, smeared material properties depending on the temperature are used in the viscoplastic model, which is generally suited in all RFW applications. Only first order residual stresses are estimated, as to be explained in Section 2.2.

Because own residual stress measurements are not realizable to an adequate extent, two RFW examples from literature are recreated using the RFW process simulation, for which the residual stress field measurements have been published. The other examples focus primarily on the failure of the welds due to high residual stresses. Although damaging and crack propagation are not included in the simulation, the plastic strain provides a good indicator for these.

## 1.3 Outline

A detailed description of the RFW process, its unique selling points and the RFW process simulation is provided in Chapter 2. All aspects of the material modeling are presented in Chapter 3 and validated exemplarily for a carbon steel in Chapter 4. In Chapter 5 the RFW structural simulation model is then used to investigate several applications. Since lightweight designs and hybrid constructions are en vogue and friction welding allows for such without connecting elements, hybrid welds of aluminum alloys and steels are included as well. Based on the abstracted findings in Chapter 5, guidelines for the residual stress compliant RFW design are deduced in Chapter 6.



## 2 State of the art

Friction welding differs in several aspects from fusion welding processes, which is advantageous in certain aspects and challenging in others. In addition to a general introduction to RFW and residual stresses, various residual stress investigations of RFW joints are reviewed, some of which are reproduced in Chapter 5 to validate the RFW simulation.

### 2.1 Rotary friction welding

Defined by ISO 15620:2019 [2], rotary friction welding is a pressure welding process, within of which two or more components are axially pressed together, while moving at high relative rotational speeds, as illustrated in Figure 2. Thereby, frictional heat is generated and the material plasticizes. Due to the axial pressure, the heated up material of the interfaces is getting crushed, twisted and radially extruded, forming a distinctive weld flash. There are several other pressure welding processes that are based on the same basic concept as RFW, but use a different relative motion.

#### RFW-affected zone

In contrast to conventional welds, Ruge [3] distinguishes three RFW-affected zones in the joints due to the severe deformations, as shown in Figure 3. The *weld center zone* (WCZ) includes the weld interface and is characterized by a fine-grained microstructure due to recrystallization induced by the local temperature, contact pressure and plastic deformation

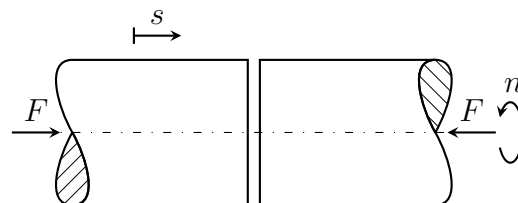


Figure 2: Basic concept of the RFW process to join two components by applying an axial force  $F$ , while rotating relative to one another with rotational speed  $n$  (resulting in an axial feed  $s$ )

(*local action*). The evaluation of the local action in the WCZ is an integral component to estimate the weld quality, which is described later on in Section 3.2.4. In mixed welds, diffusion processes are inevitable and intermetallic compounds are formed, whose layer thickness Humphreys [4] advises to keep thin due to their brittleness. The equivalent plastic strain in the WCZ can easily exceed 100 %. The further away from the weld interface, the material is less prone to soften and to deform. Just as in fusion welding, there is a *heat affected zone* (HAZ), in which only thermal effects are observed. In-between the HAZ and WCZ is the so-called *thermo-mechanically affected zone* (TMAZ), in which the material fibers are deflected in radial and tangential directions by the applied forces. The individual layer thicknesses and the properties of the zones can be adjusted by modifying the process parameters.

### Advantages and disadvantages

Thanks to *superior mechanical properties* of the RFW-affected zone in reference to the base material, safety relevant components are preferably to be joined using RFW. Contributing to this is the *self-cleaning* of the weld interface within the process by extruding existing surface impurities, like contaminations or oxide layers. Hence, thorough surface preparations are less essential than in competing processes. The RFW process can also be *highly automated and well monitored* in the RFW machine. An ecological benefit of RFW is the *absence of filler materials and inert gases*.

Other advantages result from the *self-regulating heat input in the weld interface*, where the energy is needed, discussed in more detail in Section 2.1.1. Thus, RFW allows for a *wide range of material combinations*, that are considered not possible by conventional fusion welding. Moreover, the energy introduced uniformly along the circumference causes *axisymmetric shrinkage* during cooling. Because the weld interface temperatures are typically in the solidus and liquidus temperature interval there is *no solidification shrinkage* in RFW, which would result in additional shrinkage respectively residual stresses.

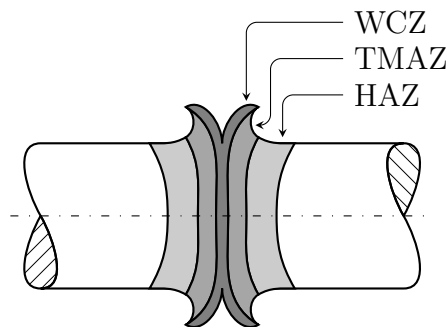


Figure 3: Subdivision of the RFW-affected zone in the weld center zone (WCZ), the thermo-mechanically affected zone (TMAZ) and the heat affected zone (HAZ)



A disadvantage is the *time and cost expensive process parameter identification*, making the process less attractive for low volume production. Furthermore, the *high process forces* must be considered in the component designs, too, which is especially true for lightweight components. The drum compressor discussed in Section 5.4 for instance is specifically designed to sustain the RFW process forces. The high process forces may induce *undesired residual stresses and deflections* outside of the RFW-affected zone.

### 2.1.1 Process stages

Figure 4 depicts typical RFW process curves. The main process parameters are the axial force  $F$ , the rotational speed of the spindle  $n$  and the axial feed  $s$ , also called burn-off length. Their recommended values depend on the material as well as the geometry of the components to be welded. The basic concept of the RFW process is rather simple, but there are many challenges in the implementation. For more information about practical RFW design experiences it shall be referred to the books of Ellis [5], Schäfer et al. [6] and Neumann and Schober [7].

#### Technical description

The RFW process consists of two main stages, called friction stage and forging stage. In both stages, two different axial forces  $F_1$  and  $F_2$  are applied and the switch can either be triggered by reaching a time  $t_2$  or a rotational speed  $n_2$  criterion, the latter being the more common one. In case of the direct drive friction welding (DDFW), the rotational speed of the spindle is held at a constant level  $n_0$  by a motor until reaching the friction time  $t_3$  or friction feed  $s_3$  criterion for braking to end the friction stage. Another concept is inertia friction welding (IFW), in which a flywheel inertia  $J$  is accelerated to  $n_0$  before the components are making contact and then decelerated in the RFW process due to the friction in-between the rotating and resting component.

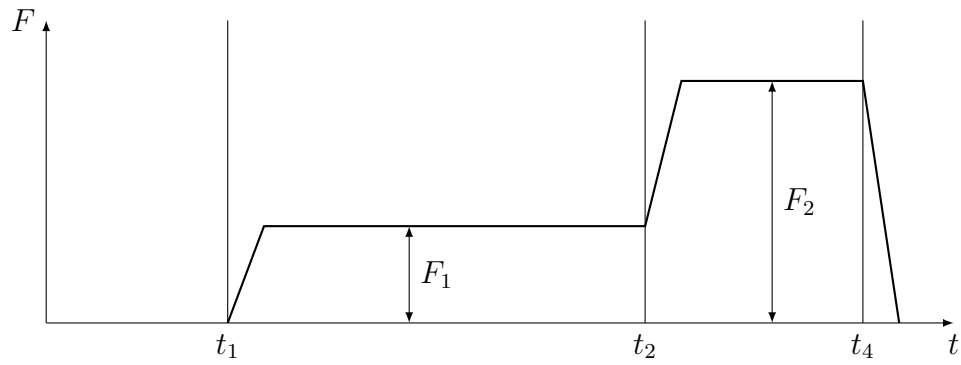
#### Physical description

In the friction stage, the required energy for the bond formation shall be generated and the weld interface is cleaned by extruding material, forming the weld flash. The kinetic energy of the rotating components is transformed into frictional heat

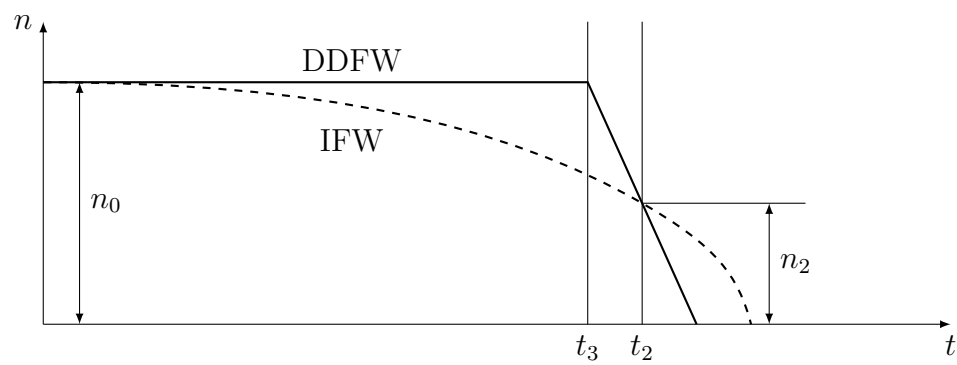
$$Q = \int T \, d\varphi \quad (1)$$

directly in the weld interface. The frictional torque

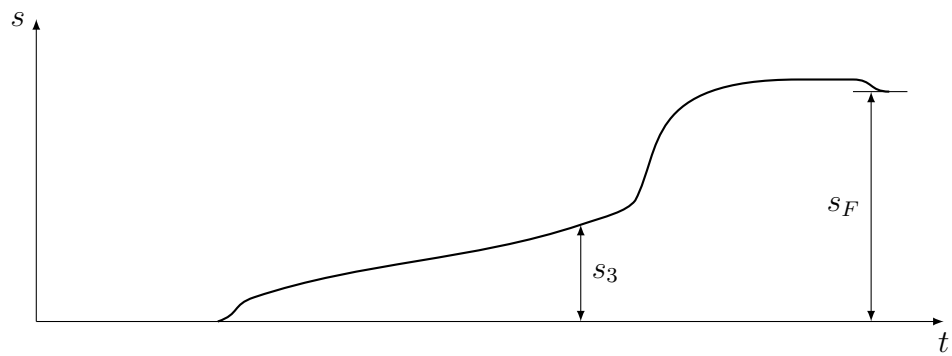
$$T = \int \tau r \, dA \quad (2)$$



(a) Axial force



(b) Rotational speed



(c) Axial feed

Figure 4: Idealized process curves for RFW processes

in this is limited by the capability of the material to transfer shear stresses  $\tau$  in the weld interface, which is the aforementioned self-regularization effect. If the shear strength  $k(\theta)$  approaches a sufficiently small value, no further heat is generated and the material is extruded due to the axially applied force. Thus, the weld interface temperatures are typically just below the melting temperature  $\theta_M$  of the lower melting material. Contrary to intuition,  $Q$  can not be significantly increased by increasing  $n_0$ , because  $T$  simultaneously sinks due to the self-regularization effect. Therefore,  $Q$  is primarily determined by the friction time  $t_3$ . Ellis [5] has identified  $t_3$  to be linearly dependent on  $s_3$  and  $F_1$  in turn. The higher  $F_1$ , the more material is extruded. High rotational speeds are advantageous to the extent that more symmetrical weld flashes might be obtained and smaller RFW machines are eventually sufficient to provide the necessary torque. If  $n_0$  is too high, though, a polishing effect of the faying surfaces is documented by Vill' [8] instead of the intended seizing. The plastic dissipation energy is small compared to  $Q$  [1].

The forging stage is supposed to remove the last remaining impurities from the weld interface, to assist the bond formation and to shape the RFW-affected zone. Therefore,  $F_2$  is usually maintained while the component cools down to a certain temperature interval. Futamata and Fuji [9] show that  $F_2 > F_1$  is beneficial for the RFW bond quality, but successful weldings made with no forging stage at all are also reported by Ellis [5], demonstrating the process robustness and allowable parameter ranges. In general, it is essential to ensure that not all previously heated up material is extruded while forging, so that sufficiently high temperatures and contact pressures are simultaneously present for metallic bonding. For an improved superposition, it is possible to increase the force while the spindle is still rotating at  $n_2 > 0$ , at the expense of a higher  $T$  and a higher process sensitivity due to the increase of  $\dot{s}$ .

### 2.1.2 Process simulation

Equations like (1) and (2) help to understand the basic relationships in RFW, but analytical solutions only exist for special cases and by establishing further simplifications. Contrary to this, the RFW process simulation model by Schmicker [1] allows quantitative predictions for arbitrary RFW processes and geometries through applying the finite element method. The physically motivated model is established on the principles of virtual velocities and temperatures and is capable of calculating the transient temperature field  $\theta$  as well as the displacement field  $\mathbf{u}$ . Besides both fields being coupled, the RFW simulation is challenging in multiple other aspects, including the material description, the frictional modeling and the large deformations. A brief description of the most relevant features is provided subsequently. For a complete description of the model details it is referred to Schmicker [1].

## Distinctive simulation features

The wide temperature range up to the melting temperature occurring in RFW has to be accounted for in the material description. In the so-called *consistently assessed Carreau fluid model* in use, later explained in Section 3.1.2 in more detail, the strain rates and the flow stresses are linked by a non-linear viscosity that depends on the temperature. The exponential approach of the Norton-Bailey constitutive model is adopted and combined with the assumption that material always deforms easier at higher temperatures for all deformation rates to allow for a consistent interpolation and a reduced amount of parameters. The model has proven to be highly accurate for hot deformation processes involving steels and non-ferrous alloys [10, 11, 12].

The material flow properties are also the restricting factor for the temperatures and torques in RFW as stated prior. Hence, the weld interface interactions are linked to the material flow properties in the so-called *exponential decay transition friction law*, which is an extension of the conventional Coulomb friction law as the shear stresses in the interface are limited by the yield stress of the material. The model includes one fitting parameter, a translation strain rate, which accommodates, for instance, for slip, like in the observed polishing at high rotational speed. Earlier models such as of Wang et al. [13] are less sophisticated and depend on specifying the (frictional) energy input to bypass the frictional modeling and thus are only partially applicable for predictive simulations.

To avoid the excessive element distortion due to the aforementioned high strains in RFW, the model is adaptively remeshed multiple times by an *implicit geometry mesher* [14, 15]. The model is remeshed as soon as the ratio of the in- and excircle of the quadrilateral triangular elements fall below a critical value and transfers in-between meshing instances are made by evaluating the shape functions of the elements, discussed in more detail in Section 3.2.3.

## Bonding condition

Unfortunately, a measure for the bond quality is not implemented by Schmicker [1] in the RFW process simulation yet. A literature review for solid-state aluminum weldings by Cooper and Allwood [16] shows that high contact pressures, temperatures and plastic deformations increase the bond quality.<sup>1</sup> To form a bond in solid-state welding processes, two main types of theories have been proposed.

The *film hypothesis* states that it is necessary to bring the base materials into close contact to form a sound bond [17]. To achieve this, oxide films and contamination layers of the surface, like in Figure 5, have to be extruded, which is achieved by sufficiently high

---

<sup>1</sup>This is equal to a high local action.

surface strains

$$\varepsilon_{pl} \geq \varepsilon_{\min}, \quad (3)$$

in which  $\varepsilon_{\min} \approx 0.5$  is an assumption for roll bonding processes [16]. In case of mixed weldings, such as of aluminum alloys and steels, it is clear that such high plastic deformations are not achievable on both sides of the weld interface. It is also evident that  $\varepsilon_{\min}$  varies depending on the surface preparation. Thus, Ashfaq et al. [18] among others [4, 19] contribute great importance to the surface cleanliness for this sort of material combinations for the bond quality. To guarantee an adequate surface cleanliness, the surfaces can be machined off directly in the RFW machine, just before welding. Regarding RFW in specific, the tracking of the material extrusion out of the WCZ as presented later in Section 3.2.4, shall be interpreted as a more conservative version of this kind of hypothesis.

According to the *energy barrier hypothesis*, clean surfaces are not the only criterion for bonding. An additional threshold energy input  $U_{\min}$  is required to form metallic bonds, which can be achieved by interchangeable amounts of pressure, plastic deformation and temperature [20]. The fulfillment of the time integral of the contact pressure  $\sigma_n$

$$\int \frac{\sigma_n}{\sigma_y} dt \geq U_{\min} \quad (4)$$

has been proposed for solid-state welding, which is similar to the void closure criterion used for forging processes [21, 22, 23]. A subgroup of models is based on the *diffusion hypothesis*, in which diffusion processes are considered to be the driving force for bonding [24]. A comprehensive model to estimate the bond properties based on this particular theory, incorporating the self-cleaning in the RFW process is to be developed by Heppner et al. [25] in parallel to this work.

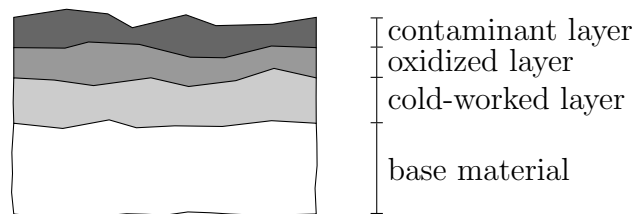


Figure 5: Metal surface structure consisting of multiple layers by Y. Zhou [24], which have to be extruded during RFW for an optimal bond quality

## 2.2 Residual stresses

Reißner [26] defines residual stresses as those that are present within a body without any external loads. Therefore, residual stresses have to be in equilibrium with themselves. Stresses caused by external loads are referred to as load stresses [27]. Both types, residual stresses and load stresses, have to be considered in the product design process. Residual stresses are often difficult to access upfront, however, as they are just introduced in the manufacturing process steps.

In general, residual stresses arise due to inhomogeneous, permanent inelastic deformations and due to newly formed bonds fixating elastic deformations [3, 28, 29]. Inelastic deformations are for instance plastic deformations caused by sufficiently high forces. Thermal expansion due to elevated temperatures alone does not cause residual stresses, but they can cause the local exceeding of the yield stress, too. High temperatures might also trigger phase transformations, leading to *transformation plasticity*, which is discussed in more detail in Section 3.1.4. A subdivision of residual stresses is made by their considered scale, in which first order residual stresses are the macroscopic ones, that are subsequently only referred to as residual stresses. The higher order stresses are those within individual grains or at a dislocation for instance (second or third order residual stresses).

With regard to RFW, high process forces are involved and high plastic deformations are intended to ensure the self-cleaning of the WCZ. High temperatures in the WCZ while bonding are also desired, whereas the rest of the components is comparatively cold. Fortunately, because the self-regularization effect limits the temperatures by the melting point, solidification shrinkage does not occur. Another positive aspect of RFW is that due to the axisymmetric heat input, the residual stress fields are axisymmetric as well.

### 2.2.1 Measurement methods

The experimental determination of residual stresses is per se based on strain measurements<sup>2</sup>, which can be destructive or non-destructive, as stresses can not be measured directly in a body.

The idea of destructive measurement techniques is to determine the deformations that result from the removal of material, which releases residual stresses. For the measurement of stresses at the surface of a component, the *hole drilling method*, the *ring core method* or *sectioning method* are applicable [28]. To identify all stresses at the surface in one spot, the strains due to the material removal have to be identified in at least three directions, for instance by strain gages. A drawback of this method is that the stresses have to

---

<sup>2</sup>Less common methods are based on ultrasonic or magnetization measurements.

be decently homogenous to be applied. The analytical solutions to calculate the residual stresses are also limited to simple geometries like plates, whereas for other geometries, the finite element method might have to be used. Nickola [30] further advises that the residual stresses shall not exceed 70 % of the yield stress to avoid the introduction of errors due to localized yielding during the drilling. Weiss [31] presents drill hole method results for rotary friction weldings, but points out the difficulties of having steep stress gradients due to RFW and the weld flash blocking the accessibility of the surface. Machining the weld flash off affects the results, though.

To map residual stress fields within a body, the *contour method* is applicable, for which the component is cut in the plane of interest. The displacements perpendicular and within this plane due to the stress relief are visually measured, based on which the stresses are calculated that force all displaced points back to their position prior to the cut using the finite element method [32].

For non-destructive residual stress mappings, the *X-ray diffraction method* and *neutron diffraction method* have been developed. Both have in common that the residual stresses are determined by comparing the lattice spacing under the influence of the residual stresses to the lattice spacing in the stress-free state. Preuss et al. [33, 34] show that the stress-free lattice spacing can change within the welding process due to microstructural transformations. The X-ray diffraction method is based on Bragg's law

$$\frac{2d_L \sin(\vartheta)}{\lambda} \in \mathbb{N} \quad (5)$$

which evaluates the different travel distances of scattered X-rays, an illustration of which is shown in Figure 6. For certain angles  $\vartheta$ , the X-rays – scattered by the atoms of the lattice of spacing  $d_L$  – are in phase, as the travel distance difference is a multiple of the wave length  $\lambda$ , depicted by the waves in Figure 6. While X-rays only allow measurements close to the surface, neutron beams also allow to carry out measurements within the body, as neutrons are scattered by the atomic nuclei. The evaluation of the results of this method is complicated by factors like the crystal orientation in polycrystalline materials. An in-depth description is provided by Hauk and Behnken [27].

A method to evaluate residual stresses outside of the field of measurement is presented by Korsunsky et al. [35, 36]. In the *inverse eigenstrain analysis* framework, permanent inelastic strains (eigenstrains) are iterated in a finite element model to match a measured field of residual stresses respectively strains. In this, the eigenstrains are artificial strains that can be introduced similar to thermal expansion to the model. A major advantage over residual stresses is that eigenstrains do not redistribute during cutting operations [37].

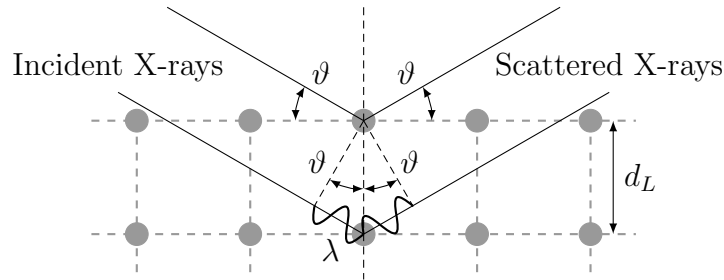


Figure 6: Diffraction of the incident X-rays at angle  $\vartheta$  by a crystalline structure with lattice spacing  $d_L$  and visualization of additional travel distance of X-rays of wave length  $\lambda$  according to Bragg's law

## 2.2.2 Rotary friction welding investigations

Only a limited number of publications address the residual stresses due to RFW. Suthoff et al. [38] note that compressive residual stresses are part of the reason for the exceptional bond strength of RFW components. This statement, however, shall not be dismissed as universally true, given the variety of geometries and materials. Hence, various publications address issues related to residual stresses caused by RFW [34, 39]. A series of publications in-between 2002 and 2015 related to Rolls Royce plc is to be highlighted, investigating possibilities to reduce residual stresses by post-weld heat treatment (PWHT) in depth. Those are mainly dealing with inertia friction welded high pressure compressor drums made of a nickel based superalloy<sup>3</sup>, but low alloy ferritic steels are discussed as well. A summary of the findings will be provided within this section. In Section 5.4, one of these examples will be used to validate the RFW structural simulation of this work.

### Investigations related to nickel-based super alloys

Starting with Preuss et al. [33, 34], the efficiency of PWHT<sup>4</sup> for RFW has been experimentally researched. To compare several results for different temperatures, the residual stress fields have been mapped by neutron diffraction, for which the weld flash have been machined off. Challenges for the stress measurements are, for one, the high neutron absorption coefficient of nickel and, for another, that the microstructural changes in the HAZ affect the stress-free lattice parameter. The measurement results are addressed in detail in Section 5.4. While the overall shape of the residual stress fields remains unaffected by PWHT, the tangential residual stresses are reduced from 1500 MPa down to 400 MPa. In a follow-up publication [40], residual stress mappings by the neutron diffraction method for three nickel based superalloys are compared. The results show that the fields are comparable for all alloys, but the magnitudes of the residual stresses differ. It is suggested that the high residual stresses are related to the flow properties during

<sup>3</sup>Powder-processed, high strength nickel-based superalloy RR1000 has been investigated.

<sup>4</sup>The exact thermal cycle of the PWHT is not provided, but information in a subsequent publication by Preuss et al. [40] suggests a temperature of about 800 °C.



---

cooling, as the yield stress of the material limits the residual stresses. An experimental study carried out by Iqbal et al. [41] shows that the initial microstructure of the material on the other hand has no significant impact on the residual stresses found after RFW. Wang et al. [13] present a finite element model to simulate RFW, including residual stress predictions. In order to make the simulations the most efficient, the temperature field is predicted using a viscous material model and only after the spindle completely stops, the model is exchanged for a viscoelastic material model, as high temperatures allow quick stress relaxation prior to this stage. While the radial residual stresses are underestimated, the axial and tangential residual stresses are overestimated by up to 35 % by the model, which might be due to the lack of reliable material properties at above 750 °C. There is also a noticeable radial offset of the calculated axial residual stresses compared to the neutron diffraction method measurements. Grant et al. [42] refined the model of Wang et al. [13] by using a viscoplastic material model and through access to more reliable material data. Hence, the radial offset of the axial residual stresses is eliminated, but the axial and radial residual stresses are now both underestimated. Especially the radial gradients of all residual stress fields are too low.

### **Investigations related to steels**

Regarding RFW of steels, Bennett et al. [43] conducted a simulative study of dissimilar rotary friction welds of a martensitic steel to a nickel based super alloy for aero-engine drive shafts. Same as Wang et al. [13], a viscous material model is used for the process simulation, which is replaced by a model including elasticity for the residual stress formation during cooling, after the spindle stopped. The model also includes the martensitic transformation based on the thermal history, which is shown to have a significant impact on the results, due to the associated volume change. When the transformation is included, the residual stresses in the RFW-affected zone are reduced by approximately 50 %. The simulative results have been later confirmed by Bennett et al. [44] by X-ray and neutron diffraction method measurements. Just as by Preuss et al. [34], high tensile tangential residual stresses are found. In subsequent model iterations, Bennett [45] further included the volume change due to austenitization for a low-alloy steel and Iracheta et al. [46] included flow property changes due to the phase transformations and strain hardening in the model, which has been prior neglected as the deformation takes place at high temperatures in RFW. The presented results show that reliable material parameters, including the elastic material properties, are necessary for accurate predictions.

### **Investigations related to hybrid welds**

Other investigations focus on the residual stresses in mixed material combinations, which are made possible by RFW. In order to predict the weld strength of mixed welds of an

aluminum alloy and a ceramic material, Weiss [31] predicts residual stresses using the finite element method. Same as Wang et al. [13], who investigated the combination of aluminum and steel, the residual stress calculations start after the spindle stops with a pre-calculated temperature distribution. Unlike Wang et al. [13], however, the forging force is neglected and the calculated residual stresses only depend on the mismatch of the thermal expansion coefficients. The WCZ side of the aluminum alloy is mainly covered by tensile residual stresses in radial direction up to 300 MPa, as the ceramic material shrinks less during cooling, having a smaller thermal expansion coefficient. The WCZ side of the ceramic material is covered by compressive radial residual stresses, but seems to be overestimated due to the linear elastic material model. Overall, these results by Weiss [31] for mixed welds seem coherent with the residual stress field mappings determined using the neutron diffraction method in the aluminum alloy and steel welds carried out by Gan et al. [47]. The WCZ of the aluminum alloy side is covered by tensile residual stresses in all directions, while the steel side is covered by compressive residual stresses. This example will be continued in more detail in Section 5.3.1.

## 2.3 Material modeling

In order to reliably calculate residual stresses using the structural simulation, a thorough material description is required that captures the macroscopic relationship of stresses and strains with sufficient accuracy. The mechanical properties of a material are primarily determined by its chemical composition and its microstructure. Due to temperatures close to the melting point in RFW, microstructural transformations occur and the material properties change. The majority of steels undergo several solid-state phase transformations during welding, which depend on the temperature, the time spent in a temperature range, plastic deformations and more. The individual influences are interdependent, meaning that deforming at 500 °C has a different impact on the transformations than when deforming at a temperature close to the melting point. Special attention will be paid to the transformations in steels as those are the most relevant for RFW applications. In aluminum alloys, the transformation kinetics are different, but they are documented in similar continuous cooling precipitation (CCP) diagrams and they have been successfully modeled using the same equations that are applied for steels [48, 49, 50].

### 2.3.1 Microstructural transformations

In general, two different categories of material modeling can be distinguished: the models based on empirical observations and the physically motivated models based on balance equations. The latter models are typically applied to representative volume elements to improve the understanding of material characteristics. For the numerical simulation of

the microstructural evolution, several models were proposed in the recent decades and the derivation of sophisticated models is an on-going research mission.

### Empirical models

Starting in the 1930s, first empirical models were developed to mathematically describe the transformation kinetics observed in experiments. A model to calculate the phase amount  $\xi$  formed from austenite  $\xi_\gamma$  in a diffusive transformation at a constant temperature  $\theta$  at the time  $t$  is given by Avrami [51, 52, 53] in general form

$$\xi(t) = 1 - e^{-k(\theta)t^n}, \quad (6)$$

which inspired several subsequent models and is typically referred to as JMAK<sup>5</sup> equation. If the nucleation rate of new particles and their growth rate is known, the material specific parameters  $k$  and  $n$  can be calculated analytically. Otherwise, the parameters can be fitted, so that the amount  $\xi$  at different incubation times at the same temperature matches to an isothermal time-temperature-transformation (TTT) diagram as depicted in Figure 7. For the temperature-dependent parameter  $k(\theta)$  multiple approaches are published, like a normal distribution function [54]. To apply the JMAK equation in non-isothermal processes, Umemoto et al. [55] incorporated the additivity rule by Scheil [56]. The additivity rule

$$\int_{(\theta)} \frac{1}{t(\xi, \theta)} \frac{1}{\theta} d\theta = 1 \quad (7)$$

treats an arbitrary temperature curve as a series of isothermal steps, the evaluation of which begins after the eutectoid temperature is reached. The function to calculate the amount  $\xi$  at the time  $t$  in non-isothermal conditions is obtained by substituting  $t$  from Equation 6 into Equation 7.

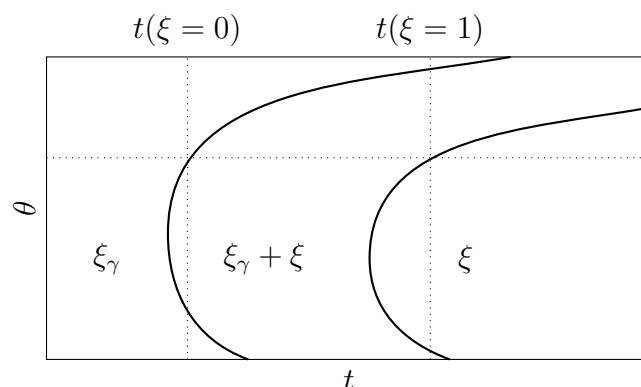


Figure 7: Schematic section of an isothermal TTT diagram for the determination of the material parameters  $k(\theta)$  and  $n(\theta)$  in Equation 6

<sup>5</sup>Johnson-Mehl-Avrami-Kolmogorov

Another popular approach has been proposed by Kirkaldy and Venugopalan [57] for diffusive transformations in form of the evolution equation

$$\dot{\xi}(t) = f(\theta, d_G, c) \left( \frac{\xi}{\xi_\infty} \right)^m \left( 1 - \frac{\xi}{\xi_\infty} \right)^n, \quad (8)$$

which includes the effects of  $\theta$ , the grain size  $g$  and the chemical composition  $c$  [58]. The parameters  $m$  and  $n$  are functions of the current phase fraction  $\xi$  as well as the temperature-dependent phase fraction in equilibrium  $\xi_\infty$ . The amount of material parameters allows for good approximations, but also complicates their identification.

Around the same time Leblond and Devaux [59] proposed an evolution equation for non-isothermal processes and arbitrary thermal cycles,

$$\dot{\xi}(t) = \frac{\xi_\infty(\theta) - \xi(t)}{\tau(\theta)}. \quad (9)$$

Here,  $\xi_\infty$  also denotes a temperature-dependent equilibrium phase fraction. The denominator  $\tau(\theta)$  represents a transformation delay time. A major advantage of this model is its validity for the displacement-based martensitic transformation, if the right function for  $\xi_\infty$  is used. Same as in the previously presented models, the adaptability of the model arises from the arbitrariness of the material parameters. Leblond and Devaux [59] do not explicitly provide a function for  $\tau(\theta)$ , which can therefore be defined depending on the temperature, the rate of temperature change and any other variable – at the expense that all these must be identified by replicating experimental data. Because Equation 9 is a first-order differential equation, though, it is fairly easy to assess the impact of  $\tau(\theta)$  on the transformation. Other than the model by Umemoto et al. [55], the time integration of Equation 9 can be effectively performed using the well-established Runge-Kutta method [60]

$$\xi(t + \Delta t) = \xi(t) + \Delta t \sum_{j=1}^s w_j \dot{\xi}_j. \quad (10)$$

### Physically based models

The above presented equations describe the transformations on a phenomenological level. Recent approaches as by Kertsch and Helm [61], solve the balance equations for linear momentum, energy and entropy on the mesoscopic level by a mean-field or a full-field approach, like phase-field method to handle grain boundaries [62]. Compared to the prior discussed empirical model by Leblond, the computational costs are comparatively high and the different length scales must be considered. Another challenging part is the occurrence of both, diffusive and displacive transformations, which involve different energy density functions.

### 2.3.2 Hardening

Conventional plasticity in metals is caused by the generation and movement of dislocations at stresses above the yield stress

$$\sigma_y = f(\dot{\varepsilon}, \varepsilon, \theta, \dots) \quad (11)$$

as discussed in Section 3.1.2. In order to change  $\sigma_y$ , the material can be hardened, which is based on the introduction of impediments that reduce the mobility of aforementioned dislocations. A schematic illustration is provided in Figure 8 (a). The purpose of presenting the individual hardening concepts is to show how the different hardening mechanisms work and how they can be incorporated in the material model. For establishing a hardening model, it is desirable to use data that is widely available for different steels and approaches that involve as few fitting parameters as possible.

#### Multiplicative and additive approaches

One approach to include hardening is by altering the reference stress  $\sigma_0$  in multiplicative approaches. The hot deformation model applied by M. Spittel and T. Spittel [63]

$$\sigma_y = \sigma_0 \underbrace{\exp(m_1\theta)}_{K_\theta} \underbrace{\varepsilon^{m_2} \exp\left(\frac{m_4}{\varepsilon}\right) (1 + \varepsilon)^{m_5\theta} \exp(m_7\varepsilon)}_{K_\varepsilon} \underbrace{\dot{\varepsilon}^{m_8\theta}}_{K_{\dot{\varepsilon}}} \quad (12)$$

includes the material parameters  $m_i$  for this. The subgrouped terms for temperature  $K_\theta$ , for strain  $K_\varepsilon$  and for strain rate  $K_{\dot{\varepsilon}}$  are interdependent in this case. Similar multiplicative models are that by Johnson and Cook [64] and the Carreau model, later presented in Section 3.1.2, which lacks  $K_\varepsilon$ . An issue is the occurrence of the factor zero, which is not relevant in the additive approaches

$$\sigma_y = \sigma_0 + \sum_i \sigma_{K,i}, \quad (13)$$

in which  $\sigma_0$  is raised by different contributors  $\sigma_{K,i}$ .

#### Work hardening

Due to plastic deformation, an increasing number of dislocations as in Figure 8 (b) prevent each other from their further propagation. Ludwik [65] models the resulting increase of yield stress as

$$\sigma_{K,\varepsilon} = K_\varepsilon \varepsilon_{pl}^n. \quad (14)$$

in which the coefficient  $K_\varepsilon$  and exponent  $n$  are material parameters that depend on the temperature. The model is identical to the strain dependent term of the model by

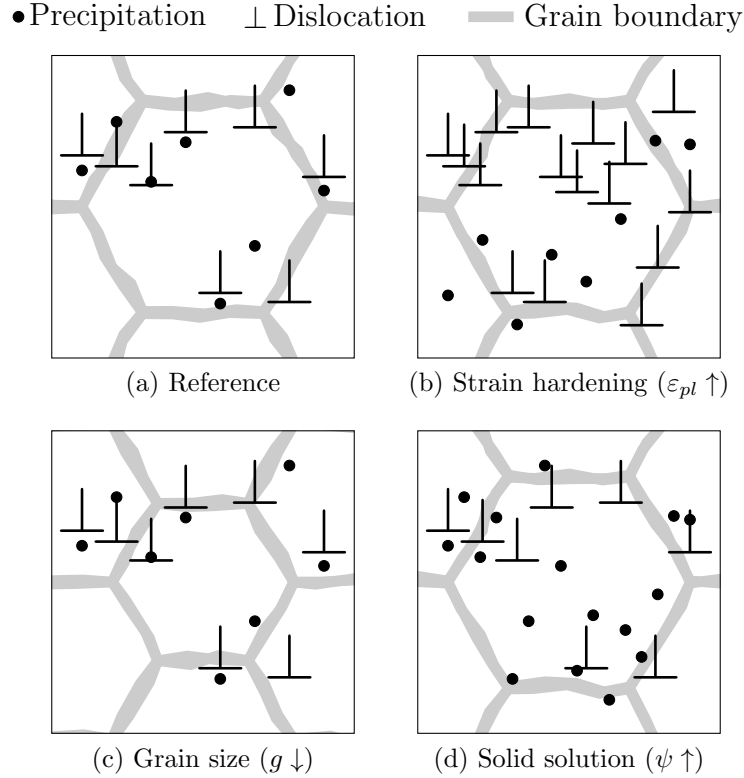


Figure 8: Visualization of different hardening mechanisms based on the density of dislocations and precipitation

Johnson and Cook [64]. If the analytical expression does not represent the work hardening properly, piecewise linear segments

$$\sigma_{K,\varepsilon} = \sum_j K_{\varepsilon,j} \Delta \varepsilon_{pl,j} \quad (15)$$

can be used for the modeling [66]. Although RFW involves severe plastic deformations, those take place at elevated temperatures. At these temperatures, this form of hardening is nullified by recovery and recrystallization processes and cold deformations should not occur either, unless the RFW process is not well designed.<sup>6</sup> Therefore the Carreau model is not extended by work hardening at this point.

### Grain refinement

RFW produces a fine-grained microstructure. Similar to the dislocations among each other, grain boundaries also block any further movement of the dislocations. The smaller the grains, the more boundaries there are to interact with, as in Figure 8 (c). Hall [67] has identified that the change of  $\sigma_y$  is proportional to the inverse of the square root of

<sup>6</sup>It is not desired to cold work the RFW affected zone, so the maximum force shall not exceed the flow stress in the lower temperature range.

the grain size  $g$

$$\sigma_{K,g} = \frac{K_g}{\sqrt{g}}. \quad (16)$$

Experimental results indicate that the material parameter  $K_g$  depends on  $\theta$  as well as  $\varepsilon$  [68, 69]. To estimate the austenite grain growth during heat treatment, Leblond and Devaux [59] derived the evolution equation

$$\dot{g} = c \exp\left(-\frac{Q_g}{R\theta}\right) - \frac{\dot{\xi}_\gamma}{\xi_\gamma} g^a, \quad (17)$$

for a variable austenite content, which involves the material parameters  $a$ ,  $c$  and  $Q_g$  that must be experimentally identified. Equation 17 is less suited for hot deformation processes, however, because it does not take deformation effects into account, which lead to a finer, rather than a coarser, microstructure.

### Solid solution strengthening

An increased amount of interstitial solute carbon atoms as in Figure 8 (d) aggravate the movement of dislocations, too. For solid solution strengthening, Fleischer [70, 71] and Labusch [72] establish hardening

$$\sigma_{K,\psi} = K_\psi \psi^a \quad (18)$$

based on the atomic concentration  $\psi$  of an obstacle element with two different exponents  $a$ . The material parameter  $K_\psi$  has to be determined for the exact element combination as a function of  $\theta$  [73]. The thickness of diffusion layers is several magnitudes lower than the width of the RFW-affected zone and the element length in the RFW simulations.<sup>7</sup>

### Transformation hardening

Another hardening mechanism is transformation hardening, which is also called martensitic hardening. Depending on the carbon content and the thermal history, different types and amounts of martensite are formed [74]. This results in an increase in hardness in the HAZ, which, other than the diffusion depth, can be several millimeters deep. Prandtl [75] analyzed the stress state and the material flow in indentation tests and derived a linear relationship<sup>8</sup> in-between the applied indenter testing force relative to the indenter imprint,

<sup>7</sup>The material properties are evaluated at the element Gauss points as shown in Section 3.2.3. The diffusion is assumed to not reach such depths.

<sup>8</sup>Hardness  $H$  exclusively refers to the Vickers hardness as standardized in ISO 6507-1:2018 [76]. This relationship can not be applied directly to other hardness scales, but ISO 18265:2013 [77] contains conversion tables.

the so-called *plastic hardness*  $\sigma_H$ , to the critical shear stress  $k$

$$\sigma_H = 2k \left(1 + \frac{\pi}{2}\right), \quad (19)$$

here determined by the Mises yield criterion

$$k = \frac{\sigma_y}{\sqrt{3}}. \quad (20)$$

Cahoon et al. [78] validated this linear relationship of hardness and yield stress experimentally for 6061 aluminum alloy and C40 carbon steel. Saeed [79] provides the more general formulation

$$\sigma_y = a_H H + b_H, \quad (21)$$

in which however only  $b_h = 0$  is physically meaningful. The validity of Equation 21 has been proven for steels, aluminum alloys and other metals [80, 81, 82]. The material parameter  $a_h$  must be fitted for known pairs of  $\sigma_y$  and  $H$ .

## 2.4 Need for further research

In a number of RFW joints designed using the RFW process simulation, failures of components have occurred. It is indicated that residual stresses caused by RFW can reach critically high values and that they have to be taken into account in the RFW design. Even though the RFW process simulation model elaborated by Schmicker [1] is well capable to simulate the RFW process and give an insight in the temperatures and the plastic material flow in many applications, it is not designed to predict residual stresses. In fact, no sign nor magnitude of residual stress are part of the RFW process simulation output. All stresses are zero, because of the viscous material formulation, the neglecting important aspects such as elasticity or thermal expansion, and due to the lack of bonding in-between the welded components. Hence, the goal of this work is to extend the RFW simulation to include the capability to calculate residual stresses. With such a simulation model, guidelines for the residual stress compliant RFW design shall be formulated, assisting in advance, before performing any simulation.

For simple geometries such as solid shafts, it has been proven that residual stress fields can be reproduced using the finite element method. What is missing is a general, fast and robust approach, so that the RFW simulation takes residual stresses a priori into account in the early development stages of advanced RFW designs. One promising approach in terms of performance and accuracy is to only consider the forging phase and the subsequent cooling, based on a temperature distribution, which can either be assumed or predetermined using a RFW process simulation. A thermo-mechanically coupling of



the structural simulation to predict the residual stresses and the process simulation to estimate the temperatures does not appear to be essential and the heat of deformation and the heat of transformation are to be neglected in the structural simulation.

Nonetheless, besides including elasticity and thermal expansion, the mechanical effects of phase transformations of steels due to the thermal history shall be incorporated in the material model as well, as steels are currently the most relevant material for RFW applications. The empirical model by Leblond and Devaux [59] is to be implemented and a generalized approach for the material parameter identification is to be proposed. Hardness and hardening are closely linked.<sup>9</sup> Knowing the hardness, other material properties can be assessed, which is used to determine the local yield stresses or the ultimate tensile stresses in non-homogeneous samples. By predicting the phase transformations, the flow properties of steels shall be altered according to the formed microstructure, which shall be incorporated in the consistently-assessed Carreau fluid model. Instead of splitting the properties for each phase, the properties shall be smeared based on the phase fractions.

For bonding, the film hypothesis is to be implemented for the time being and a permanent bond is assumed, when the bonding condition is fulfilled. A bond shall result in higher residual stresses than a destroyed bond, leading to conservative RFW designs using the RFW simulation.

---

<sup>9</sup>This reflects in expressions such as “hard to deform” or in referring to strengthening as hardening.



## 3 Simulation model

In the following, the key elements of the simulation model will be outlined. An essential part of the RFW structural simulation is the extension of the consistently-assessed Carreau fluid model, for which a detailed description is given in Section 3.1. Compared to own prior works [83], the model has been generalized and phase transformations are included. The phase transformation model is specifically tailored for steels as most RFW applications are involving these. The model parameters are all fitted to replicate the transformation paths in continuous cooling transformation (CCT) diagrams. The finite element model, including the contact and bonding mechanics, is described in detail in Section 3.2.

### 3.1 Material simulation

A key element is the accessibility of material information for the wide range of steels applicable for friction welding. The presented approach takes advantage of the relationship of the material flow stress  $\sigma_y$  and the material hardness  $H$

$$\sigma_y \propto H, \quad (22)$$

which is presented more detailed in Section 3.1.3, after explaining the hardness prediction using the simulation in Section 3.1.1 and the reference flow stress in Section 3.1.2.

#### 3.1.1 Microstructural transformations

Balancing out the material simulation purpose to reproduce the observations correctly based on existing experiments, the model complexity, the effort to determine the material parameters and the calculation costs, Equation 9 by Leblond and Devaux [59] is to be favoured and implemented to model the phase transformations, which will be subsequently described in more details. Thanks to its versatility, Equation 9 is applicable for the transformations during heating and during cooling. Furthermore, the model is extensible and necessary material information is broadly available for the most relevant

steels in CCT diagrams, which include similar cooling paths to those in RFW.<sup>10</sup>

### Heat-up stage

Information about the equilibrium amount of austenite  $\xi_\gamma$  at a constant temperatures is found in the binary iron-carbon (Fe-C) phase diagram, whereas the dependence on the heating rate is found in time-temperature-austenitization (TTA) diagrams. Congruent with Equation 9, the austenitization is described by

$$\dot{\xi}_\gamma(t) = \frac{\xi_{\gamma,\infty}(\theta) - \xi_\gamma(t)}{\tau_\gamma(\theta)}. \quad (23)$$

In the beginning, the transformation is only starting slow, which is guaranteed by a low equilibrium amount  $\xi_\gamma$  and a high delay time  $\tau_\gamma$ . Towards the completion of transformation,  $\dot{\xi}_\gamma$  decreases, because the numerator becomes automatically smaller. The material parameters

$$\xi_{\gamma,\infty} = \begin{cases} 0 & \text{for } \theta < A_{c1} \\ 1 & \text{for } \theta > A_{c3} \\ \frac{\theta - A_{c1}}{A_{c3} - A_{c1}} & \text{else} \end{cases} \quad (24)$$

and

$$\tau_\gamma = \tau_3 + \frac{\tau_1 - \tau_3}{2}(1 - \tanh(\sigma_\gamma(\theta - \theta_\gamma))) \quad (25)$$

with

$$\theta_\gamma = \frac{A_{c3} + A_{c1}}{2} \quad (26)$$

$$\sigma_\gamma = \frac{2}{A_{c3} - A_{c1}} \quad (27)$$

are fitted to match the experimental austenitization start and finish temperatures for different heating rates  $\dot{\theta}$  extracted from the TTA diagram.<sup>11</sup> The sigmoid function for the delay time  $\tau_\gamma$  involves two fitting constants  $\tau_{1,3} > 0$  that are identified in a gradient based optimization (Figure 9). The austenitization process start is mainly determined by  $\tau_1$  and  $\tau_3$  affects its end. The parameters  $\sigma_\gamma$  and  $\theta_\gamma$  are fixed to minimize the optimization effort for this model and are calculated based on the  $A_{c1}$  and  $A_{c3}$  temperatures of the steel for the thermodynamic equilibrium.<sup>12</sup> Equation 24 is also implemented as a smooth function and does not involve any fitting parameters. Due to the neglecting of deformation effects on the grain size, the differential equation for grain growth at elevated temperatures

<sup>10</sup>The cooling curves are similar to the Newtonian cooling curves.

<sup>11</sup>To determine  $\xi_{\gamma,\infty}$ , a linear relation to  $\theta$  has been used as by Leblond and Devaux [59]. For plain carbon steels, using the Fe-C phase diagram and applying lever rule might be an even more precise approximation.

<sup>12</sup>The temperatures  $A_{c1}$  and  $A_{c3}$  are often included in CCT diagrams like in Figure 10 or can be determined using the Fe-C phase diagram or can be assumed to match the start and finish temperatures in the corresponding TTA diagram for a sufficiently slow heating rate.

by Leblond and Devaux [59] is not solved at this point. The effect of deformation is discussed separately later in this section.

### Cool-down stage

The transformations during cooling are more complex, because diffusive based and displacive based transformations have to be distinguished – the former are denoted by the index  $\alpha$  and the latter by index  $\alpha'$ . Depending on the cooling rate, the austenite ( $A$ ) transforms into different fractions of ferrite ( $F$ ), pearlite ( $P$ ), bainite ( $B$ ) and martensite ( $M$ ), which is documented in CCT diagrams such as in Figure 10. Whereas ferrite and pearlite are formed by diffusion processes – just like austenite – the martensite formation is displacive and can only occur at sufficiently high cooling rates, so the carbon becomes trapped. For bainite both transformation types are documented and lower and upper bainite are distinguished [84, 85]. As CCT diagrams do not include this differentiation, the bainitic transformations are handled like being one diffusive transformation, regardless of the temperature. During cooling, the formations highly depend on the cooling rate, which is taken into account in a modified version of Equation 9

$$\dot{\xi}_\alpha = \frac{\xi_{\alpha,\infty}(\theta) - \xi_\alpha(t)}{\tau_\alpha(\theta, \dot{\theta})} \quad (28)$$

by including a temperature rate dependent  $\tau_\alpha(\theta, \dot{\theta})$ . For  $\tau_\alpha(\theta, \dot{\theta})$  the normal distribution inspired function

$$\tau_\alpha(\theta, \dot{\theta}) = k_\alpha(\dot{\theta})\sqrt{2\pi}\sigma_\alpha e^{\frac{1}{2}\left(\frac{\theta-\theta_\alpha}{\sigma_\alpha}\right)^2} \quad (29)$$

including

$$\theta_\alpha = \frac{\theta_{\alpha,s}(\dot{\theta}) + \theta_{\alpha,f}(\dot{\theta})}{2} \quad (30)$$

$$\sigma_\alpha = \frac{\theta_{\alpha,s}(\dot{\theta}) - \theta_{\alpha,f}(\dot{\theta})}{4} \quad (31)$$

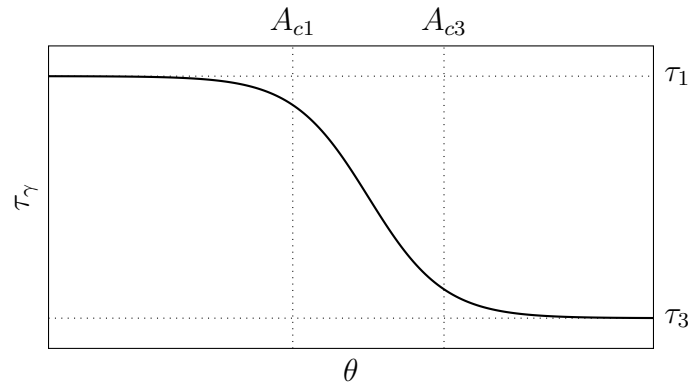


Figure 9: Smoothly defined function for the temperature-dependent delay time  $\tau_\gamma$  for Equation 23 by Leblond and Devaux [59]

is proposed, which has its minimum at  $\theta_\alpha$ , right between the phase transformation start and finish temperatures of the diffusive transformations  $\theta_{\alpha,s}(\dot{\theta})$  and  $\theta_{\alpha,f}(\dot{\theta})$ . Other than in Equation 25,  $\sigma_\alpha$  and  $\theta_\alpha$  in Equation 29 establish a rate dependency. If the fitting parameter  $k_\alpha$  is increased, the transformation is slowed down and smaller fractions of  $\xi_\alpha$  are formed. The inverse function of  $\tau_\alpha$  is plotted in Figure 11.

### Displacive transformation

For the displacement-based martensite formation,  $\dot{\xi}_{\alpha'}$  being formulated analogue to  $\dot{\xi}_\alpha$ ,

$$\xi_{\alpha',\infty} = 1 - e^{-\beta(\theta_{\alpha',s}-\theta)} \quad (32)$$

by Koistinen and Marburger [87] is used to calculate a fictitious equilibrium content  $\xi_{\alpha',\infty}$  for the current temperature, making Equation 28 applicable for diffusive transformations, too. Assuming 1 % of retaining austenite at the (martensite) finish temperature  $\theta_f$ , Equation 32 can be re-written to determine  $\beta$  as<sup>13</sup>

$$\beta = \frac{\ln 100}{\theta_{\alpha',s} - \theta_{\alpha',f}}. \quad (33)$$

Totten [88] provides information about  $\theta_{\alpha',f}$  and  $\theta_{\alpha',s}$  of martensite and their dependence on the chemical composition, in which the carbon content in particular is found to be relevant. For the delay time  $\tau_{\alpha'}$  a small, fixed value is assumed. A transformation delay is effectively non-existent for the displacive transformations.

### Model calibration

The model parameters in Section 3.1.1 have to be calibrated to match TTA and CCT diagrams, which are available for a variety of steels for the design of heat treatment purposes. In addition to information on the microstructural composition for different cooling paths, it also contains information about the transformation temperatures and the resulting microstructural hardnesses.

Even though the qualitative trends of adjusting the introduced model parameters are well predictable, their analytical derivation has not been successful and they have to be determined in a gradient based optimization [89]. Within this optimization, the model parameters  $k_\alpha(\dot{\theta})$  are identified as such that the mean squared error

$$Z = \left( \xi_{\alpha,CCT}(\dot{\theta}) - \xi_{\alpha,DGL}(\dot{\theta}, k_\alpha(\dot{\theta})) \right)^2 \quad (34)$$

is minimized in the objective function  $Z$ .

---

<sup>13</sup> $\ln 0.01 = -\ln 100$

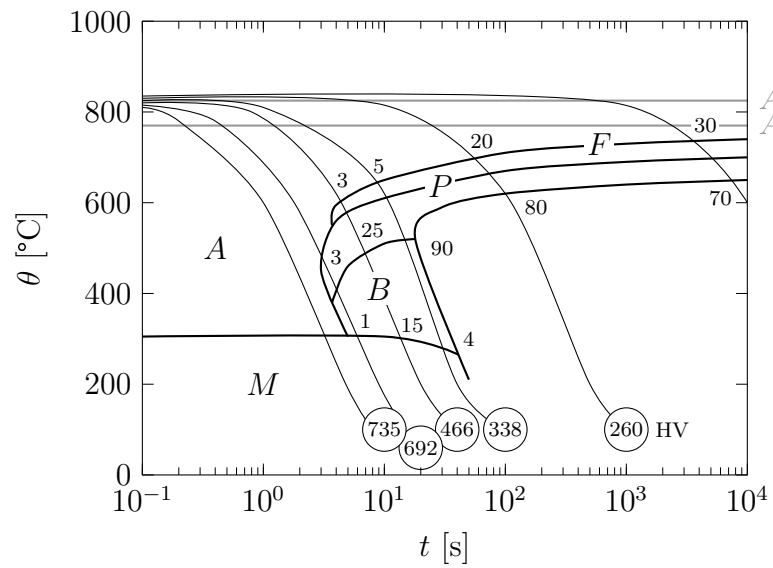


Figure 10: Example of a CCT diagram containing several information about phase transformations during cooling (austenitization at 840 °C) [86]

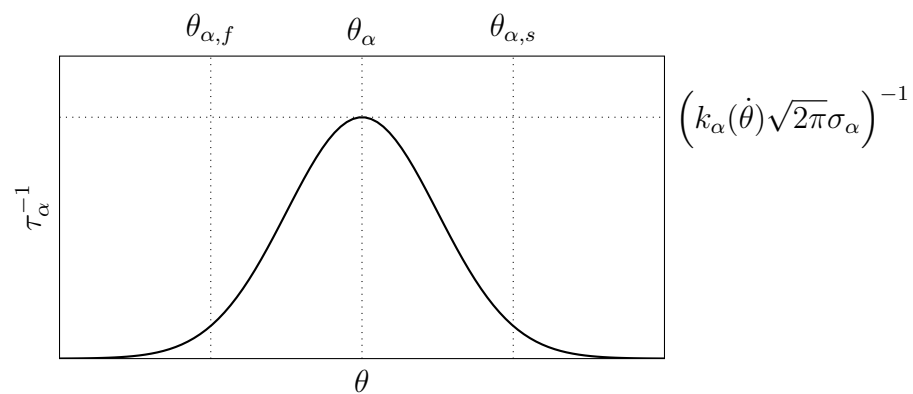


Figure 11: Smoothly defined function for the temperature- and cooling rate-dependent delay time  $\tau_\alpha$  for cooling transformations in Equation 28

## Deviating peak temperatures and deformations

To calibrate the model, it is important to consider that the CCT diagrams are created for certain thermal (and deformation) histories as briefly discussed in the following. Mathematically, further effects can be included fairly easy by extending  $\tau_i$  respectively manipulating  $\xi_{i,\infty}$ , but experimental data for validation is only available in few cases.

Higher austenitization temperatures lead to coarser grains, which affects the transformations during cooling. Seyffarth et al. [90] present a collection of welding CCT diagrams. In order to produce these, the material samples have been heated up to 1350 °C (instead of about 800 °C used for conventional CCT diagrams for heat treatment). A several minutes long holding phase is also eliminated. The coarser grains have a lower surface energy, which delays the transformation during cooling, because the necessary transformation energy becomes only available at lower temperatures. As a result, the transformation curves of the CCT diagram are shifted rightwards, to lower temperatures [90]. To transfer a CCT diagram for the austenitization temperature  $\theta_\gamma$  to a higher austenitization temperature  $\theta'_\gamma$ , the approach by Piekarska et al. [91] is adopted. The time scale of the CCT diagram

$$t'_i = \frac{\theta'_\gamma - \theta_\delta}{\theta_\gamma - \theta_\delta} \cdot t_i \quad (35)$$

is shifted, while the CCT diagram temperatures

$$\theta'_i \equiv \theta_i \quad (36)$$

are unchanged. This approximation is well capable to reproduce the trends found in experiments. The higher the austenitization temperature, the bigger the shift. This multiplicative approach affects the transformations at slow cooling rates more than at fast rates and overall pushes the transformations temperatures to be lower – except for the martensite start temperature  $\theta_{\alpha',s}$ . The back transformation temperature  $\theta_\delta$  is determined from the CCT for  $\theta_\gamma$  for the cooling rate

$$\dot{\theta}_\delta = \frac{\theta'_\gamma - \theta_\gamma}{1 \text{ s}}, \quad (37)$$

which is likely to result in  $\theta_\delta = \theta_{\alpha',s}$ .

High degrees of deformation just have the opposite effect of elevated austenitization temperatures – the reference CCT is shifted more to the left, which is referred to as *deformation induced ferrite transformation* [92]. By deforming at temperatures above 800 °C, the austenite grains are refined and the diffusive transformations during cooling are triggered earlier [92, 93, 94, 95]. The higher the deformation temperature is, the higher the required degree of deformation becomes to trigger this effect [93]. The results



by Nürnbergger et al. [96, 97], however, indicate that the deformation impact is much less severe than that of the cooling rate. In Figure 12, the hardnesses of 42CrMo4 alloy steel after different cooling paths and deforming at different temperatures are plotted. Referring to the RFW process, the plastic deformation  $\varepsilon_{pl}$  can easily exceed 100 %, because the material is getting compressed by the axial force, as well as twisted and sheared off in the WCZ due to the frictional torque. At the same time, the deformation temperatures are typically close to the melting point of the material, in which case the effect of deformation is becoming less as stated earlier. The effects of high temperatures and high degrees of deformations shall be both accommodated the same way in the transformation model and are combined in a single CCT diagram time corrector  $\delta_{RFW}$ . Combining both effects, the CCT diagram times  $t_i$  are horizontally shifted by multiplying with  $\delta_{RFW}$  as

$$t'_i = \delta_{RFW} \cdot t_i. \quad (38)$$

For peak temperatures below  $A_{C1}$  that are insufficient to cause the formation of austenite, prior hardened areas might lose part of their hardness during RFW, because the elevated temperatures allow the martensitic lattice to relax. To account for such tempering effects, the local maximum temperature of the material point history might be compared to data documented in tempering diagrams, which is neglected at this point.

### Hardness determination

Ion et al. [98] suggest that the overall hardness of the microstructure of a steel can be determined by a simple law of mixture containing the hardnesses of martensite  $H_M$ , bainite  $H_B$ , perlite  $H_P$ , ferrite  $H_F$  and austenite  $H_A$ , multiplied with the corresponding phase fractions

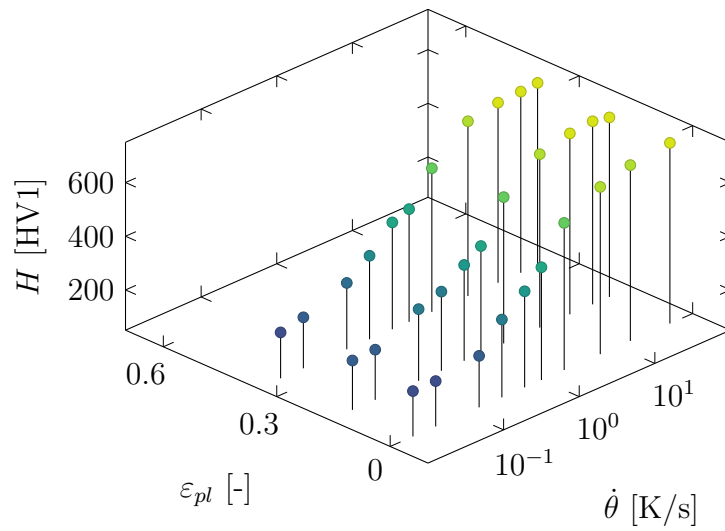
$$H(\dot{\theta}) = \xi_M(\dot{\theta})H_M + \xi_B(\dot{\theta})H_B + \xi_P(\dot{\theta})H_P + \xi_F(\dot{\theta})H_F + \xi_A(\dot{\theta})H_A \quad (39)$$

that works “surprisingly well” and has been used later by Khorral [99] for instance. To estimate the hardness of the individual phases  $H_i$ , the hardness values known for several different phase compositions  $j$  from a CCT diagram is decomposed. The resulting linear system is typically overdetermined, thus the least squares method

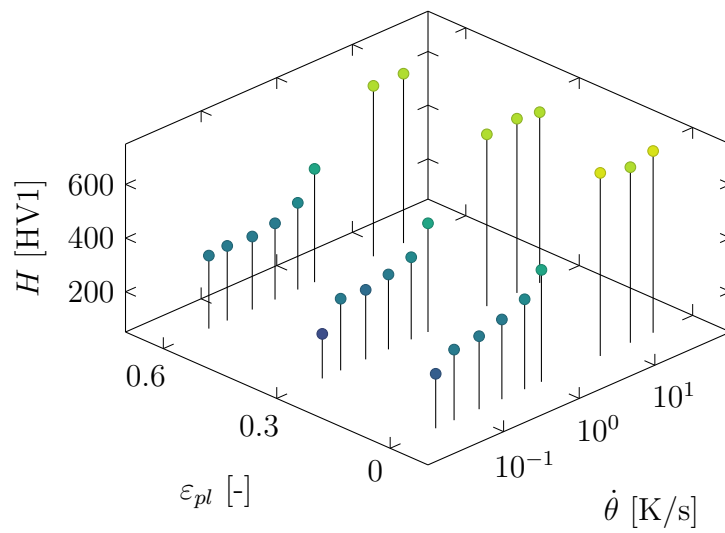
$$\min_{H_i} \sum_j \left( \sum_i (\xi_{i,j} H_i) - H_j \right)^2 \quad (40)$$

is applied, with the boundary conditions

$$H_{P,F,A} \leq H_B \leq H_M. \quad (41)$$



(a) Deformed at 850 °C



(b) Deformed at 1200 °C

Figure 12: Hardnesses measurements of 42CrMo4 steel after cooling with different rates after deforming at two different temperatures by Nürnbergger et al. [96, 97]

If a CCT diagram is not available or insufficient for fitting, Maynier et al. [100] provide the empirical equations

$$H_M = 127 + 949 C + 27 \text{ Si} + 11 \text{ Mn} + 8 \text{ Ni} + 16 \text{ Cr} + 21 \log \frac{1}{\Delta t_{8/5}} \quad (42)$$

$$H_B = -323 + 185 C + 330 \text{ Si} + 153 \text{ Mn} + 65 \text{ Ni} + 144 \text{ Cr} + 191 \text{ Mo} \\ + (89 + 53 C - 55 \text{ Si} - 22 \text{ Mn} - 10 \text{ Ni} - 20 \text{ Cr} - 33 \text{ Mo}) \log \frac{1}{\Delta t_{8/5}} \quad (43)$$

$$H_{P,F,A} = 42 - 223 C + 53 \text{ Si} + 30 \text{ Mn} + 12.6 \text{ Ni} + 7 \text{ Cr} + 19 \text{ Mo} \\ + (10 - 19 \text{ Si} + 4 \text{ Ni} + 8 \text{ Cr} + 130 \text{ V}) \log \frac{1}{\Delta t_{8/5}} \quad (44)$$

for low alloy steels that include the chemical composition and the cooling time  $\Delta t_{8/5}$  from 800 to 500 °C.

### 3.1.2 Consistently-assessed Carreau fluid model

The described material model elaborated by Schmicker [1] is an essential part of the RFW process simulation, which is subsequently extended. A transformation-based hardening mechanism is introduced in Section 3.1.3 and more strain components are added to the plastic strain in Section 3.1.4. A detailed description of the hot tensile testing routine is provided in Section 4.2.

The consistently-assessed Carreau fluid model, in the following only referred to as Carreau model, describes a viscous material characteristic, in which a non-linear dependency of the current plastic strain rate  $\dot{\epsilon}_{pl}$  to the current temperature  $\theta$  and the current stress deviator  $\boldsymbol{\sigma}'$  in the form of

$$\dot{\epsilon}_{pl} = \frac{1}{2\mu} \boldsymbol{\sigma}' \quad (45)$$

exists. Based on the assumptions of isotropic and ductile material characteristics, the Mises stress

$$\sigma_v = \sqrt{\frac{3}{2} \boldsymbol{\sigma} : \boldsymbol{\sigma}} \quad (46)$$

and the Mises strain rate

$$\dot{\epsilon}_{pl,v} = \sqrt{\frac{2}{3} \dot{\boldsymbol{\epsilon}}'_{pl} : \dot{\boldsymbol{\epsilon}}'_{pl}} \quad (47)$$

are used to describe an uniaxial state, which can be represented by a single damper element of non-linear viscosity  $3\mu$ , as illustrated in Figure 13. The subscript  $v$  is subsequently omitted in all scalar functions. Like the model of Sellars and Tegart [101] or the Norton-Bailey model [102], the parameters of the Carreau model are fairly expedient. Major advantages of the Carreau model are that it fits the full temperature range better and that it involves less cryptic parameters.

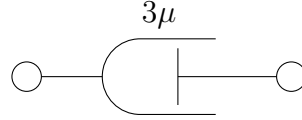


Figure 13: Single Newton element of non-linear viscosity  $\mu$  relating the Mises stress to the Mises strain rate

Identical to the Norton-Bailey model, in the double logarithmic depiction, the relation of the Mises stresses and Mises strain rate is linear, formulated as

$$\frac{\dot{\epsilon}_{pl}}{\dot{\epsilon}_0} = \left( \frac{\sigma}{\sigma_0} \right)^n, \quad (48)$$

which is applicable for a wide range of materials and strain rates. In Equation 48, the reference stress  $\sigma_0$  is to be defined for a fixed strain rate  $\dot{\epsilon}_0$ . The reference stress  $\sigma_0$  and the exponents  $n$  are functions of  $\theta$ . Encyclopedias like by Doege et al. [103] or by M. Spittel and T. Spittel [63, 104, 105] provide material deformation data for the most common materials. To overcome the inconvenience to determine  $n(\theta)$  for every temperature, Schmicker et al. [10] assume that all isotherms are intersecting in one characteristic point  $(\sigma_C, \dot{\epsilon}_C)$

$$n = \frac{\log\left(\frac{\dot{\epsilon}_C}{\dot{\epsilon}_0}\right)}{\log\left(\frac{\sigma_C}{\sigma_0}\right)} \quad (49)$$

as illustrated in Figure 14. It is intuitive that increasing  $\theta$  or  $\sigma$  shall increase  $\dot{\epsilon}_{pl}$  in most cases<sup>14</sup>, which is guaranteed by

$$\sigma_C > \max(\sigma_0(\theta)), \quad (50)$$

$$\varepsilon_C > \varepsilon_0. \quad (51)$$

Additionally, the viscosity  $\mu$  is restricted as

$$\mu = \left[ 1 + \left( \left( \frac{\sigma_0}{3\dot{\epsilon}_0\mu_0} \right)^{\frac{n}{1-n}} \frac{\dot{\epsilon}_{pl}}{\dot{\epsilon}_0} \right)^2 \right]^{\frac{1-n}{2n}} (\mu_0 - \mu_\infty) + \mu_\infty \quad (52)$$

by upper and lower saturation viscosities  $\mu_0$  and  $\mu_\infty$ , which shall be interpreted as numerical parameters of the Carreau model. Within the working range,  $\mu$  is kept unchanged, but the intersection in  $(\sigma_C, \dot{\epsilon}_C)$  is prevented.

<sup>14</sup>An exclusion is the Portevin–Le Chatelier effect observed in some materials at temperatures below the temperatures at which the deformations during RFW are typically generated.

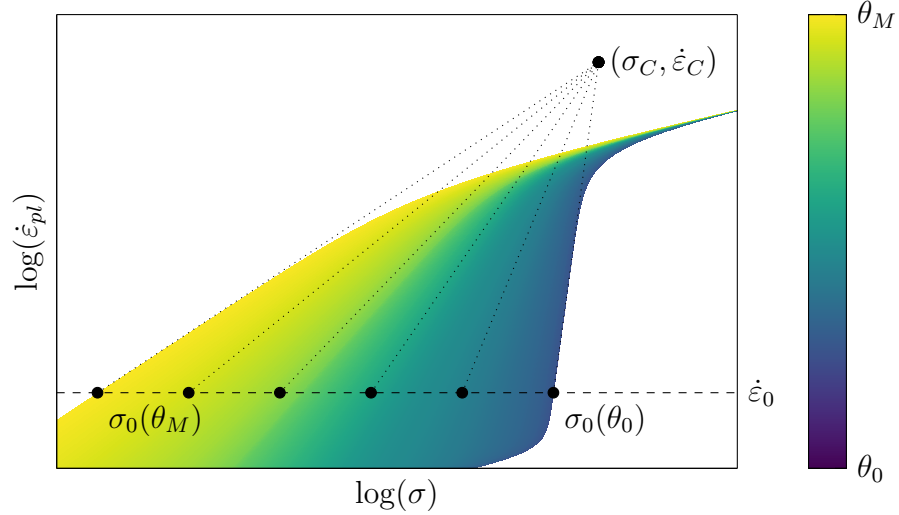


Figure 14: Depiction of the consistently-assessed Carreau fluid model, describing the full temperature and strain rate range experienced in RFW

### 3.1.3 Transformation hardening

To account for hardening and softening of steels due to phase transformations, it is proposed to alter the Carreau model of each material point based on the hardness, which in turn is based on the phase composition, based on the thermal history.

#### Approach based on the hardness

At room temperature  $\theta_0$ ,

$$\sigma_y(\theta_0) = K_H \sigma_0(\theta_0) \quad (53)$$

can be derived from Equation 21 by Saeed [79], which involves the factor

$$K_H = \frac{H'_0}{H_0} \quad (54)$$

that is the quotient of the Vickers hardness  $H_0$  corresponding to the reference stress  $\sigma_0$  and  $H'_0$  to the yield stress of the hardened material  $\sigma_y = \sigma'_0$ . The hardnesses are evaluated based on the calculated microstructures as in Section 3.1.1.

#### Extension to the full temperature range

A modification is necessary, so that martensitic hardening, occurring at temperatures at around 300 °C,  $K_H > 1$ , does not affect the yield stress at the melting temperature  $\theta_M$ . To extent the approach to the full temperature range experienced in RFW in this work,

$$\sigma'_0(\theta, \dot{\theta}) = \kappa \sigma_0(\theta + \theta_\kappa) \quad (55)$$

is proposed. Through Equation 55,  $\sigma'_0$  and  $\sigma_0$  are not necessarily identical, but remain similarly shaped. A visualization of the introduced model parameters and their extraction from the CCT diagram for a fast and a slow cooling rate is given in Figure 15. The newly introduced *hardening factor*

$$\kappa(\theta, \dot{\theta}) = \begin{cases} 1 & \text{for } \theta > A_{c1} \\ K_H & \text{for } \theta < \theta_\delta \\ K_H \frac{\theta - A_{c1}}{\theta_\delta - A_{c1}} & \text{else} \end{cases} \quad (56)$$

vertically scales the flow stress curve as  $K_H$  does, but the temperature range for hardening is split in three regimes. Similarly defined is the *hardening offset*

$$\theta_\kappa(\theta, \dot{\theta}) = \begin{cases} 0 & \text{for } \theta > A_{c1} \\ A_{c1} - \theta_\delta & \text{for } \theta < \theta_\delta \\ (A_{c1} - \theta_\delta) \frac{\theta - A_{c1}}{\theta_\delta - A_{c1}} & \text{else} \end{cases} \quad (57)$$

since a horizontal shift is also to be expected. Reason for this is that at high cooling rates the softer austenitic phase is present at lower temperatures [106]. The definitions of  $\kappa$  and  $\theta_\kappa$  in Equation 56 and Equation 57 ensure that no hardening happens above  $A_{c1}$ , since no phase transformation, which alters the hardness, takes place yet. The hardening shall only be applied below the back transformation temperature  $\theta_\delta$  at which the back transformation starts. In-between  $A_{c1}$  and  $\theta_\delta$  is a linear transmission range, which ensures that  $\sigma'_0$  is continuous. The shift from  $\sigma_0$  to  $\sigma'_0$  is seen in Figure 16. To keep the material law consistent, the strain rate sensitivity exponents  $n(\theta)$  have to be adjusted, too, denoted as  $n'(\theta, \dot{\theta})$ . At  $\theta_M$ , the phase transformations shall have no effect on the flow properties, so that  $n'(\theta_M, \dot{\theta})$  matches  $n(\theta_M)$ . At  $\theta_0$ , the low strain rate sensitivity is maintained by setting  $n'(\theta_0, \dot{\theta})$  to match  $n(\theta_0)$ .

### 3.1.4 Elastoplasticity

As previously indicated, the constitutive approach by Schmicker et al. [10] is ineligible for residual stress predictions. Therefore, the single Newton element is replaced by a combination of Prandtl bodies with elastic and plastic elements arranged as in Figure 17, which allows for the inclusion of the effects of phase transformations.

#### Rheological modeling and conventional plasticity

In the partially austenitized area in the transition to the base material it is necessary to treat the material as a binary mixture of material of the amount of transformed fraction  $\phi$

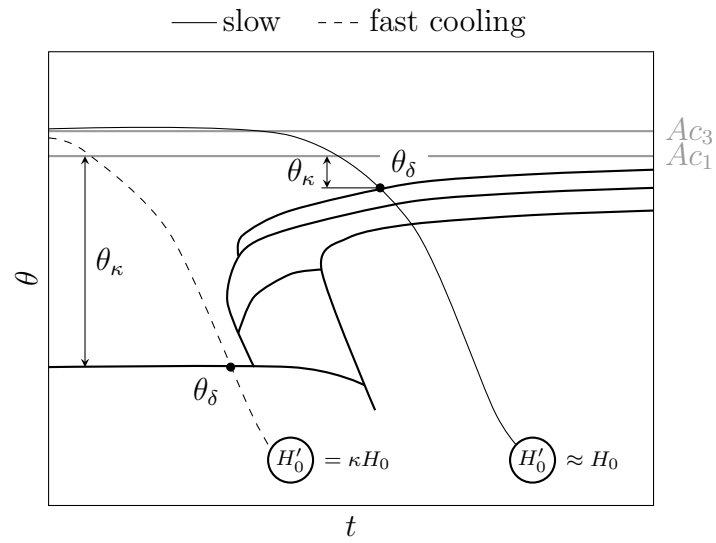


Figure 15: Extraction of  $\kappa$  and  $\theta_\kappa$  in Equation 55 for fast and slow cooling rates from the CCT diagram

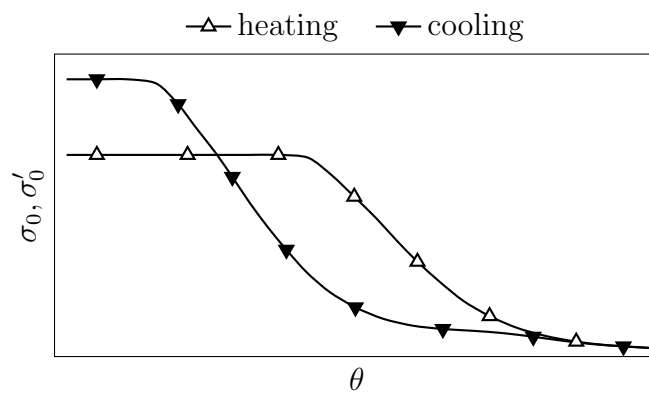


Figure 16: Different flow properties due to the microstructural changes induced by heating and subsequent cooling

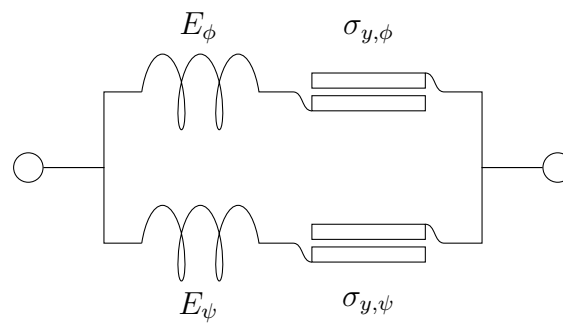


Figure 17: Binary combination of two Prandtl bodies to distinguish the material properties of the transformed  $\phi$  and the remaining phase fraction  $\psi$

and of the untransformed fraction  $\psi = (1 - \phi)$ .<sup>15</sup> On macroscopic level, the phases are assumed to be uniformly distributed and randomly oriented, resulting in macroscopic isotropy concerning all thermomechanical properties. Referring to Equation 45, the same stress deviator direction is assumed in both fractions. Due to these assumptions, only first-order residual stresses can be evaluated by the model.

Considering that stresses are relieved quickly at sufficient high temperatures and no permanent bonds can be formed while the components are moving relative to each, only the end of the RFW process is evaluated in the RFW structural simulation. Assuming only small deformations during cooling, the additive decomposition of total macroscopic strain

$$\boldsymbol{\varepsilon} = \boldsymbol{\varepsilon}_{el} + \boldsymbol{\varepsilon}_{pl} \quad (58)$$

is utilized. Severe deformations are undesirable at this RFW process stage, because the newly formed bonds are likely to be damaged. The transition from the single Newton body in Section 3.1.2 to the Saint-Venant bodies is achieved by performing the time integration using the explicit Euler method

$$\boldsymbol{\varepsilon}_{pl}(t + \Delta t) = \boldsymbol{\varepsilon}_{pl}(t) + \dot{\boldsymbol{\varepsilon}}_{pl}(t)\Delta t. \quad (59)$$

Homogenization assumptions are the isostress and the isostrain concepts [107, 108, 109]. The former assumes uniform stress and the latter uniform strain across the constituents. As demonstrated by Naumenko et al. [110], the isostrain ansatz

$$\boldsymbol{\varepsilon}_{\phi} = \boldsymbol{\varepsilon}_{\psi} = \boldsymbol{\varepsilon} \quad (60)$$

with the stresses distributed based on the phase fractions

$$\boldsymbol{\sigma} = \phi\boldsymbol{\sigma}_{\phi} + (1 - \phi)\boldsymbol{\sigma}_{\psi} \quad (61)$$

for the uniaxial case is adopted. In addition to the elastic strains  $\boldsymbol{\varepsilon}_{el}$  and plastic strains  $\boldsymbol{\varepsilon}_{pl}$ , thermal expansion strains  $\boldsymbol{\varepsilon}_{th}$  and transformation plasticity  $\boldsymbol{\varepsilon}_{tr}$  are also included

$$\boldsymbol{\varepsilon}_{\phi} = \boldsymbol{\varepsilon}_{el,\phi} + \boldsymbol{\varepsilon}_{pl,\phi} + \boldsymbol{\varepsilon}_{th,\phi} + \boldsymbol{\varepsilon}_{tr,\phi} = \frac{\boldsymbol{\sigma}_{\phi}}{E_{\phi}} + \boldsymbol{\varepsilon}_{pl,\phi} + \boldsymbol{\varepsilon}_{th,\phi} + \boldsymbol{\varepsilon}_{tr,\phi} \quad (62)$$

$$\boldsymbol{\varepsilon}_{\psi} = \boldsymbol{\varepsilon}_{el,\psi} + \boldsymbol{\varepsilon}_{pl,\psi} + \boldsymbol{\varepsilon}_{th,\psi} + \boldsymbol{\varepsilon}_{tr,\psi} = \frac{\boldsymbol{\sigma}_{\psi}}{E_{\psi}} + \boldsymbol{\varepsilon}_{pl,\psi} + \boldsymbol{\varepsilon}_{th,\psi} + \boldsymbol{\varepsilon}_{tr,\psi}. \quad (63)$$

---

<sup>15</sup>The subscript  $\phi$  is equivalent to the apostrophe in Section 3.1.3, which has been replaced here for a better readability.



For the same elastic modulus,  $E_\phi = E_\psi = E$ , Equations (60–63) are combined to

$$\sigma = E(\varepsilon - \varepsilon_{pl} - \varepsilon_{th} - \varepsilon_{tr}) \quad (64)$$

$$\varepsilon_{pl} = \phi\varepsilon_{pl,\phi} + (1 - \phi)\varepsilon_{pl,\psi} \quad (65)$$

$$\varepsilon_{th} = \phi\varepsilon_{th,\phi} + (1 - \phi)\varepsilon_{th,\psi} \quad (66)$$

$$\varepsilon_{tr} = \phi\varepsilon_{tr,\phi} + (1 - \phi)\varepsilon_{tr,\psi} . \quad (67)$$

The rate form of Equation 65 is identical to the model by Leblond et al. [111, 112] based on the Hill-Mandel condition.<sup>16</sup> To evaluate the plastic strain rates  $\dot{\varepsilon}_{pl,\phi}$ ,  $\dot{\varepsilon}_{pl,\psi}$  according to Equation 45, the stresses of the phases are calculated as

$$\sigma_\phi = E(\varepsilon - \varepsilon_{th,\phi} - \varepsilon_{pl,\phi} - \varepsilon_{tr,\phi}) \quad (68)$$

$$\sigma_\psi = E(\varepsilon - \varepsilon_{th,\psi} - \varepsilon_{pl,\psi} - \varepsilon_{tr,\psi}) . \quad (69)$$

## Elasticity

Like the melting temperature  $\theta_M$ , the elastic modulus  $E$  is determined by the interatomic forces. Both values depend on the chemical composition and there is a linear relationship between them [113]. For steels,  $E$  is typically in the range of 200 to 210 GPa. Assuming linear elasticity in the elastic region,  $E$  is defined as a temperature-dependent function according to EN 1993-1-2:2005 [114] for steels and EN 1999-1-1:2007 [115] for aluminum alloys as in Figure 18 (a). For the three-dimensional case,

$$\boldsymbol{\sigma} = \mathbf{C}\boldsymbol{\varepsilon}_{el} = \mathbf{C}(\boldsymbol{\varepsilon} - \boldsymbol{\varepsilon}_{pl} - \boldsymbol{\varepsilon}_{th} - \boldsymbol{\varepsilon}_{tr}) \quad (70)$$

is applied, using the Voigt notation. The material stiffness matrix  $\mathbf{C}$  and the vector representations of the stress  $\boldsymbol{\sigma}$  and strain  $\boldsymbol{\varepsilon}$  are provided in Appendix A.

## Thermal expansion

The thermal expansion strains are calculated using

$$\varepsilon_{th} = \sum_i \xi_i \boldsymbol{\alpha}_i (\theta - \theta_0) \quad (71)$$

and thermal coefficient

$$\boldsymbol{\alpha}_i = \left[ \alpha_i \quad \alpha_i \quad \alpha_i \quad 0 \quad 0 \quad 0 \right]^T . \quad (72)$$

<sup>16</sup>The averaged internal work on the microscale is identical to the work on the macroscale.

For each phase a separate, temperature-dependent thermal expansion coefficient  $\alpha_i$  can be considered [116, 117]. Figure 18 (b) includes the uniaxial thermal expansion of steels and aluminum alloys depending on the temperature according to Eurocode [114, 115]. The different phases in steels lead to different slopes in the range below 760 °C than above 850 °C. Because temperature-dependent  $\alpha_i$  are difficult to identify for all steels in Chapter 5 and no general relation of  $\alpha_i$  is identified, it is assumed that all phases expand identically, except for austenite.<sup>17</sup>

### Transformation plasticity

Between 760 °C and 850 °C the volume increase by thermal expansion is compensated by lattice changes, related to the transformation plasticity strains

$$\boldsymbol{\varepsilon}_{tr} = \sum_i \xi_i \boldsymbol{\delta} \quad (73)$$

with transformation plasticity coefficient

$$\boldsymbol{\delta} = [\delta_i \quad \delta_i \quad \delta_i \quad 0 \quad 0 \quad 0]^\top \quad (74)$$

$$\delta_i = \sqrt[3]{\frac{V_i}{V_{bcc}}} - 1 \quad (75)$$

being similarly defined as the coefficient for thermal expansion. During austenitization of steels, the lattice structure changes from the body-centered cubic (bcc) packaging of ferrite/pearlite to face-centered cubic (fcc) packaging of austenite. As depicted in Figure 19, this transformation results in a volume reduction. In contrast to this, a volume increase occurs, if martensite with a body-centered tetragonal (bct) packaging is formed. A major influence on the packing density is the carbon content  $C$ . Totten [88] emphasizes that the transformation of retained austenite can be sufficient to cause cracks in a component.

Table 1: Linear thermal expansion coefficients of the individual phases of C45 carbon steel and of 20MnCr5 case-hardening steel [116, 117]

Phase	Structure	$\alpha$ [ $10^{-6}/\text{K}$ ]	
		C45	20MnCr5
Ferrite	bcc	15.34	14.36
Pearlite	bcc	15.34	14.36
Bainite	bcc	11.71	16.22
Martensite	bct	13.60	11.75
Austenite	fcc	21.78	24.52

<sup>17</sup>When calculating the expansion coefficients, transformation strains must be taken into account.

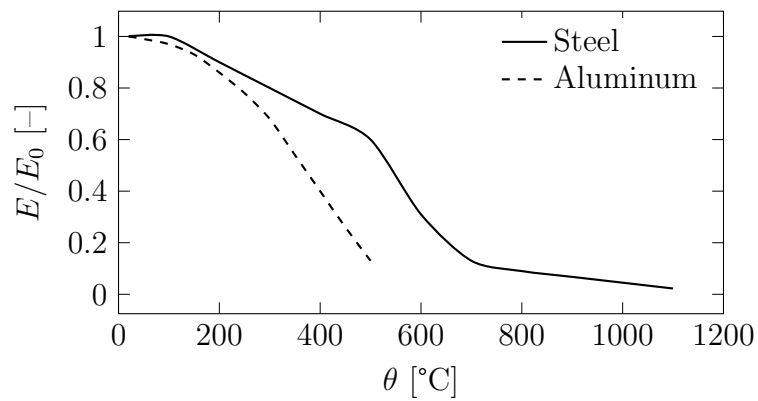
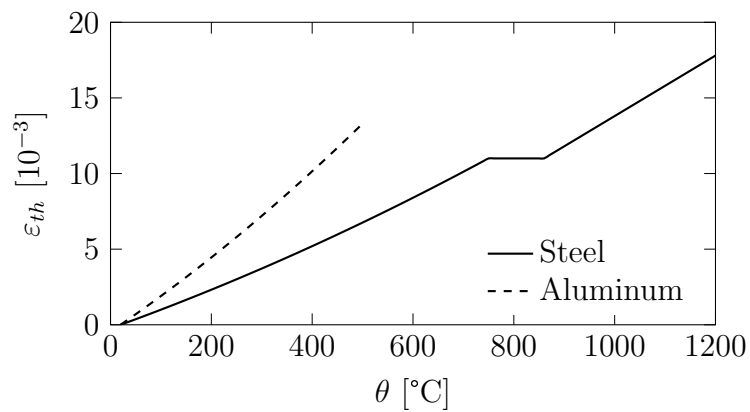
(a) Elastic modulus  $E$ (b) Thermal expansion  $\varepsilon_{th}$ 

Figure 18: Change of the elastic modulus and the thermal strain of steels and aluminum due to elevated temperatures according to Eurocode [114, 115]

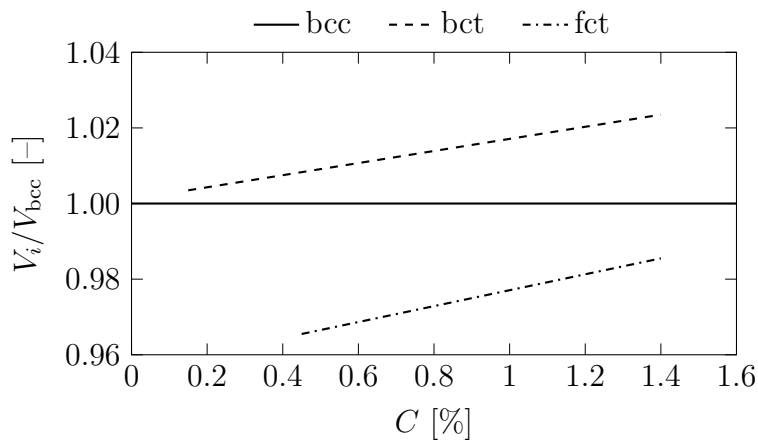


Figure 19: Transformation volume changes depending on percentage of the carbon content of the steel [118]

## 3.2 Finite element modeling

The RFW material and structural simulations are postprocessing steps of the RFW process simulation, which has to be considered in their implementation. Due to the extension of the material model in Section 3.1, a switch from the principle of virtual velocities to the principle of virtual displacements is made. Furthermore, it is sufficient to consider small displacements during cooling and deal with those without the need to remesh the model. In addition to Schmicker [1], standard textbooks are recommended for the fundamentals of finite element modeling [119, 120, 121].

### 3.2.1 Small displacements

Joining by RFW is particularly suitable if the components are axisymmetric. In addition, unlike in other welding methods, the heat distribution is also axisymmetric, because the heat is directly introduced by friction in-between the components. Hence, the vector  $\mathbf{x}$  describing the spatial position of an arbitrary point is provided in cylindrical coordinates

$$\mathbf{x} = \sqrt{r}\mathbf{e}_r + z\mathbf{e}_z. \quad (76)$$

The radial component is quadratic, as this is more suitable for elastoplastic, axisymmetric analyses according to Yu et al. [122]. The displacement vector  $\mathbf{u}$  is formulated the same as the velocities in the RFW process simulation as

$$\mathbf{u} = \frac{u_r}{2\sqrt{r}}\mathbf{e}_r + u_z\mathbf{e}_z + \sqrt{r}u_\varphi\mathbf{e}_\varphi, \quad (77)$$

which simplifies the implementation.

As stresses can be quickly relieved in the RFW process due to the high temperatures, the structural simulation model focuses on the cooling process. At this stage, only small deformations shall occur, if the RFW process is properly designed. The necessary nabla operator for the strain description corresponding to these coordinates is

$$\nabla = \frac{\partial}{\partial x}\mathbf{e}_x + \frac{\partial}{\partial y}\mathbf{e}_y + \frac{\partial}{\partial z}\mathbf{e}_z = 2\sqrt{r}\frac{\partial}{\partial r}\mathbf{e}_r + \frac{\partial}{\partial z}\mathbf{e}_z + \frac{1}{r}\frac{\partial}{\partial \varphi}\mathbf{e}_\varphi. \quad (78)$$

Upon small deformations, the strain tensor  $\boldsymbol{\varepsilon}$  is the symmetric part of the deformation gradient [123]

$$\boldsymbol{\varepsilon} = \frac{1}{2}((\nabla\mathbf{u})^\top + \nabla\mathbf{u}) = \begin{bmatrix} -\frac{u_r}{2r} + \frac{\partial u_r}{\partial r} & \sqrt{r}\frac{\partial u_z}{\partial r} & \frac{r}{\sqrt{r}}\frac{\partial u_\varphi}{\partial r} \\ \sqrt{r}\frac{\partial u_z}{\partial r} & \frac{\partial u_z}{\partial z} & \frac{\sqrt{r}}{2}\frac{\partial u_\varphi}{\partial z} \\ \frac{r}{\sqrt{r}}\frac{\partial u_\varphi}{\partial r} & \frac{\sqrt{r}}{2}\frac{\partial u_\varphi}{\partial z} & \frac{u_r}{2r} \end{bmatrix} \mathbf{e}_i \otimes \mathbf{e}_j. \quad (79)$$

### 3.2.2 Principle of virtual displacements

In contrast to the RFW process simulations by Schmicker [1], virtual displacements  $\delta \mathbf{u}$  are used to obtain an equilibrium solution for each time step. The reason behind this is that the additionally introduced strain components  $\varepsilon_{el}$ ,  $\varepsilon_{th}$  and  $\varepsilon_{tr}$  are more convenient to handle than their strain rates.

The basis of the derivation of the principle of virtual displacement is the strong form of the local balance of momentum

$$\rho \ddot{\mathbf{u}} - \operatorname{div} \boldsymbol{\sigma} - \rho \mathbf{b} = \mathbf{0} \quad (80)$$

with the traction boundary conditions

$$\boldsymbol{\sigma} \mathbf{n} - \mathbf{t} = \mathbf{0}. \quad (81)$$

in which  $\mathbf{b}$  denotes the body force vector,  $\mathbf{n}$  the surface normal vector,  $\mathbf{t}$  the surface stress vector and  $\rho$  the material density. To obtain an approximate solution, in which Equations 80 and 81 are fulfilled on average, they are expressed in the weak form

$$\int \delta \mathbf{u} (\rho \ddot{\mathbf{u}} - \operatorname{div} \boldsymbol{\sigma} - \rho \mathbf{b}) dV + \int \delta \mathbf{u} (\boldsymbol{\sigma} \mathbf{n} - \mathbf{t}) dA = 0, \quad (82)$$

which can be re-written for small deformations as

$$\int \delta \mathbf{u} \rho \ddot{\mathbf{u}} dV + \int \delta \boldsymbol{\varepsilon}^T : \boldsymbol{\sigma} dV = \int \delta \mathbf{u} \mathbf{b} dV + \int \delta \mathbf{u} \mathbf{t} dA. \quad (83)$$

By substituting Equation 70 into 83, the internal work term becomes

$$\delta U = \int_{(e)} \delta \boldsymbol{\varepsilon}^T : \boldsymbol{\sigma} dV = \int_{(e)} \delta \boldsymbol{\varepsilon}^T \mathbf{C} (\boldsymbol{\varepsilon} - \boldsymbol{\varepsilon}_{pl} - \boldsymbol{\varepsilon}_{th} - \boldsymbol{\varepsilon}_{tr}) dV. \quad (84)$$

The right side of Equation 83 bundles the external work term

$$\delta W = \int \delta \mathbf{u} \mathbf{b} dV + \int \delta \mathbf{u} \mathbf{t} dA. \quad (85)$$

Omitting the dynamic term, the equilibrium of the internal and the external work

$$\delta U - \delta W = 0 \quad (86)$$

is solved numerically by applying the Newton method for every time step, which is continued in Section 3.2.5.

### 3.2.3 Element formulation

To numerically solve Equation 86, the weld is discretized by six node triangular elements, depicted in Figure 20. Advantages of these elements are that the meshing algorithm by Persson and Peraire [14] is very robust and their suitability for elastoplastic problems, because there are no locking effects.

The displacements within an element are controlled by the displacements of the element nodes in form of

$$\mathbf{u} = \mathbf{N}\mathbf{u}_e. \quad (87)$$

Both,  $\mathbf{u}$  and  $\mathbf{u}_e$ , are coupled by the quadratic shape functions

$$\mathbf{N} = \begin{bmatrix} N_1\mathbf{1} & N_2\mathbf{1} & N_3\mathbf{1} & N_4\mathbf{1} & N_5\mathbf{1} & N_6\mathbf{1} \end{bmatrix} \quad (88)$$

that are formulated in the natural coordinates  $0 \leq \zeta, \eta \leq 1$

$$\begin{aligned} N_1 &= (\zeta + \eta - 1)(2\zeta + 2\eta - 1) \\ N_2 &= -4\zeta(\zeta + \eta - 1) \\ N_3 &= \zeta(2\zeta - 1) \\ N_4 &= 4\zeta\eta \\ N_5 &= \eta(2\eta - 1) \\ N_6 &= -4\eta(\zeta + \eta - 1). \end{aligned} \quad (89)$$

The shape functions are also used to track the nodal histories over the remeshes of the RFW process simulation and to transfer them to the RFW structural simulation. Referring back to Equation 79, the strain within an element is expressed as a function of the nodal displacements

$$\boldsymbol{\varepsilon} = \mathbf{B}\mathbf{u}_e \quad (90)$$

with the differential operator

$$\mathbf{B} = \begin{bmatrix} \mathbf{B}_1 & \mathbf{B}_2 & \mathbf{B}_3 & \mathbf{B}_4 & \mathbf{B}_5 & \mathbf{B}_6 \end{bmatrix} \quad (91)$$

$$\mathbf{B}_i = \begin{bmatrix} -\frac{N_i}{2\bar{r}} + \frac{\partial N_i}{\partial \bar{r}} & 0 & 0 \\ 0 & \frac{\partial N_i}{\partial z} & 0 \\ \frac{N_i}{2\bar{r}} & 0 & 0 \\ 0 & 0 & \sqrt{\bar{r}} \frac{\partial N_i}{\partial z} \\ 0 & 0 & 2\bar{r} \frac{\partial N_i}{\partial \bar{r}} \\ \frac{1}{2\sqrt{\bar{r}}} \frac{\partial N_i}{\partial z} & 2\sqrt{\bar{r}} \frac{\partial N_i}{\partial \bar{r}} & 0 \end{bmatrix}. \quad (92)$$

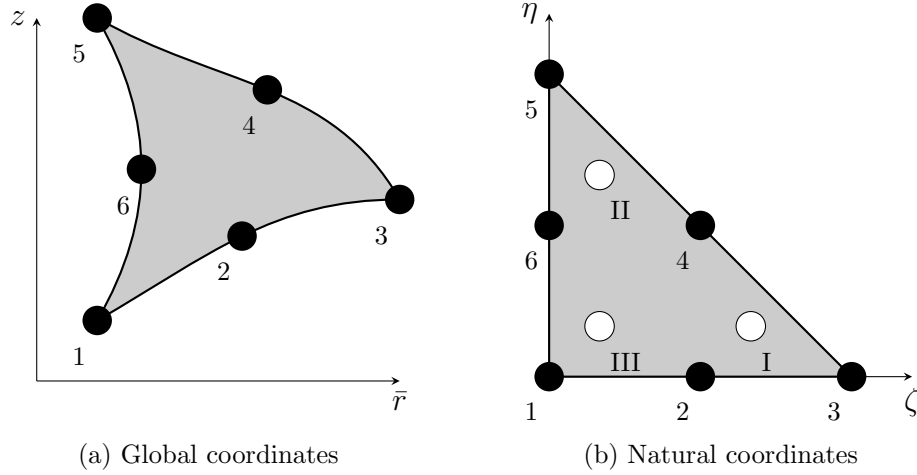


Figure 20: Six node triangular elements having quadratic shape functions, including the numbering of the nodes (black) and of the Gauss points (white)

Using Equation 90, the internal work in Equation 84 is rewritten in accordance to the finite element formulation as

$$\delta U = \delta \mathbf{u}_e^\top \mathbf{K} \mathbf{u}_e - \delta \mathbf{u}_e^\top \int_{(e)} \mathbf{B}^\top \mathbf{C} (\boldsymbol{\varepsilon}_{pl} + \boldsymbol{\varepsilon}_{th} + \boldsymbol{\varepsilon}_{tr}) dV = \delta \mathbf{u}_e^\top \mathbf{f}_{\text{int}} \quad (93)$$

including the element stiffness matrix

$$\mathbf{K} = \int_{(e)} \mathbf{B}^\top \mathbf{C} \mathbf{B} dV, \quad (94)$$

which has to be updated regularly even though the deformations are small, because  $\mathbf{C}$  is temperature dependent. The forging force as well as the forces to hold the components in the toolings are bundled in one force vector  $\mathbf{f}_{\text{ext}}$ , so that the external work is rewritten as

$$\delta W = \delta \mathbf{u}_e^\top \mathbf{f}_{\text{ext}}. \quad (95)$$

To perform the numerical integrations the three point Gauss rule is applied.

### 3.2.4 Contacts and bonding

The implementations of the contact and bonding conditions are handled almost identically. Following the approach of Pascoe and Mottershead [124], the constraints are formulated in reference to the surface normal vector

$$\mathbf{n} = \begin{bmatrix} n_r & n_z & 0 \end{bmatrix} \quad (96)$$

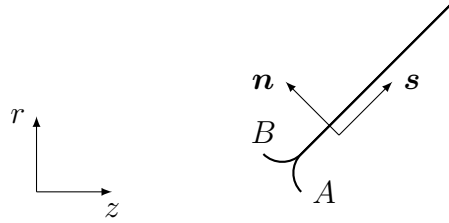


Figure 21: Surface normal and tangential vectors  $\mathbf{n}$  and  $\mathbf{s}$  used in the contact and bonding formulations

and tangential vector  $\mathbf{s}$ , as depicted in Figure 21. For bonding, this trick is not as relevant as for the contact formulation in normal and tangential directions. The conversion between the global coordinates and the surface coordinates is given as<sup>18</sup>

$$\begin{bmatrix} u_n \\ u_s \end{bmatrix} = \begin{bmatrix} n_r & n_z \\ n_z & n_r \end{bmatrix} \begin{bmatrix} u_r \\ u_z \end{bmatrix}. \quad (97)$$

For two components, subsequently indexed  $A$  and  $B$ , a frictionless contact requires only the surface normal displacements to be identical

$$\mathbf{n}^\top \mathbf{N}(\zeta_A, \eta_A) \mathbf{u}_{e,A} - \mathbf{n}^\top \mathbf{N}(\zeta_B, \eta_B) \mathbf{u}_{e,B} = 0. \quad (98)$$

For bonding the same displacements in all directions have to be guaranteed

$$\mathbf{N}(\zeta_A, \eta_A) \mathbf{u}_{e,A} = \mathbf{N}(\zeta_B, \eta_B) \mathbf{u}_{e,B}. \quad (99)$$

Equation 98 and Equation 99 are both realized by a penalty formulation and evaluated at the surface Gauss points of the components to distribute the conditions among the element edge nodes. The penalty value in use is controlled by the maximum matrix element of  $\mathbf{K}$  of the contacting elements. The same frictionless contact procedure is also used for tooling contacts.

### Bonding condition

To estimate the quality of bonding, the evaluation of the *local action* (temperature, contact pressure and plastic deformation) in the WCZ is proposed. The local action of the material points in the WCZ in Figure 22 can be backtracked, which results in the profiles shown in Figure 23. In general, it is desired to superimpose high values of all local action parameters in the WCZ. Figure 22 (a) demonstrates that the material points, which form the WCZ in Figure 22 (b), originate from the inside, proving the self-cleaning effect in the RFW process. The equivalent plastic strains plotted in Figure 23 (a) are

<sup>18</sup>The circumferential direction is left out at this point for clarity.

<sup>18</sup>The widening of the profiles is caused by the radial outwards movement of the tracked material points.



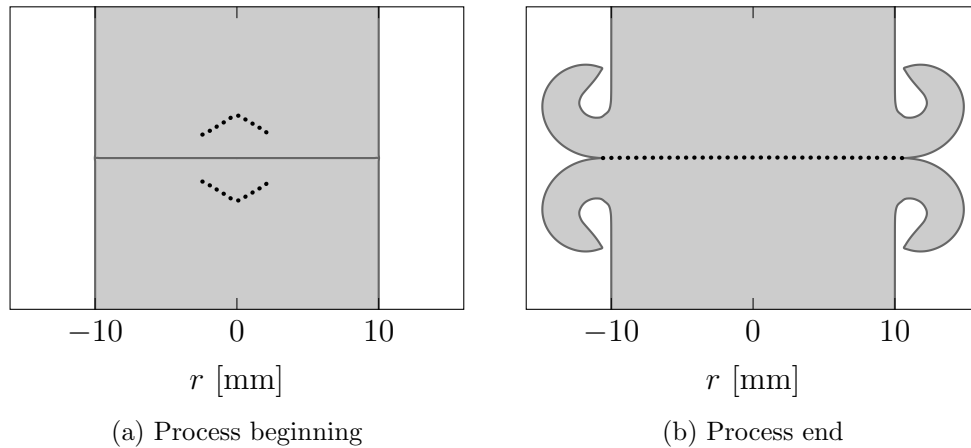


Figure 22: Tracking of the material points in the WCZ (black dots) back to the process beginning

typically greater 1.0 due to the high forces and temperatures in RFW processes and a forged microstructure can be found. This evaluation is also consistent with the film hypothesis criterion discussed in Section 2.1.2 and the bond strength criterion

$$\begin{cases} \infty & \text{for } \varepsilon_{pl} \geq \varepsilon_{\min} \\ 0 & \text{else} \end{cases} \quad (100)$$

is used as a quantitative bonding criterion in the RFW structural simulations. It can be argued that any debonding reduces the residual stresses. Thus, no damaging model is implemented and the ideal bond is used as a conservative assumption in the RFW structural simulation. Another important aspect is the temperature at bonding. Higher bonding temperatures are expected to lead to higher residual stresses due to more shrinkage during cooling. Eventhough the highest temperatures occur in the friction phase, the moment of bonding has to be after the spindle is stopped. As long as the components move relative to each other, any bonds are immediately disrupted. The spindle stop is well visible in Figure 23 (b), at around 8 s, when the temperature begins to drop. The radial distribution of the contact pressure<sup>19</sup> is plotted in Figure 23 (c). At the outer diameter the pressure is lower than in the center, which may cause insufficient bonding. To enhance the aforementioned superposition, the forging phase might be started early, while the spindle is still rotating. The ideal time to release the forging force depends on how fast the WCZ cools down. The contact pressure could be included in an evaluation according to the energy hypothesis for bonding. But during the forging stage, the displacements in the WCZ might also exceed the grid spacing substantially, leading to the disruption of bonds, which is not considered for the sake of conservativity.

<sup>19</sup>Before the material point is in the contact interface, the highest principal stresses are plotted, the direction of which are the normal direction of the weld interface in most cases.

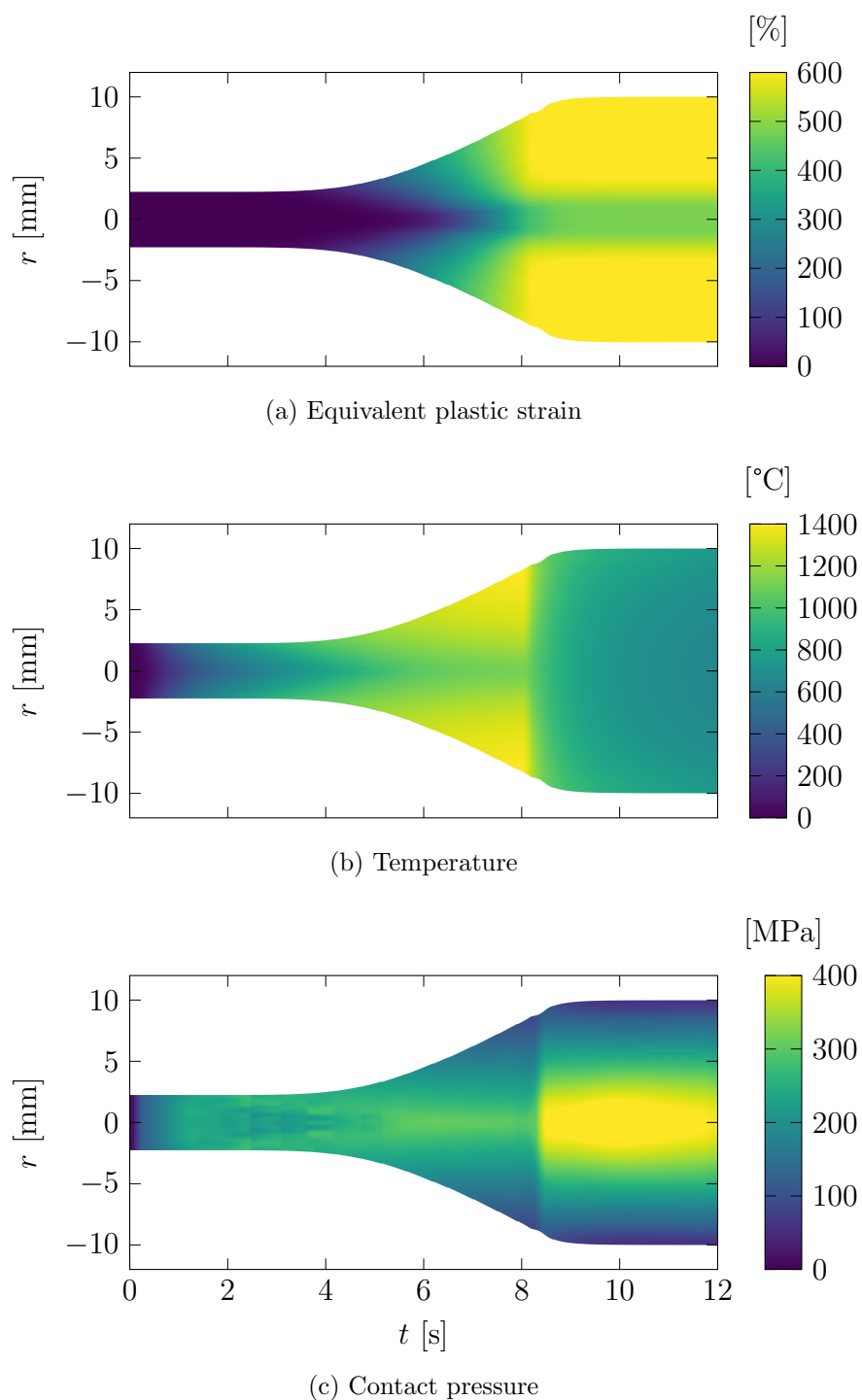


Figure 23: Local action (temperature, contact pressure and plastic strain) in the WCZ extracted from the RFW simulation of the weld in Figure 22

## Simulation model migration

Neither thermal expansion nor bonding are part of the RFW process simulation and are only introduced in the RFW structural simulation. When transferring the interim results after the spindle is stopped from the RFW process simulation to the start of the RFW structural simulation, four steps are essential:

1. The material model is exchanged to include all other strain components on top of  $\varepsilon_{pl}$ . This eventually leads to a stress distributions different from the one in the RFW process simulation.
2. A frictionless contact between both components is established, so that the components can be thermally expanded with the exchanged material model. The components shall be thermally expanded before bonding, as the components are also in an expanded state before bonding.
3. Based on the current temperatures, the components are thermally expanded and the forging force is applied. The temperatures and the forging force are both raised in multiple steps up to the final values. After every step, the contact is updated.
4. The contacting surfaces are converted to ideal bonds. After this, the transient simulation of the cooling process starts.

### 3.2.5 Solver and time integration

To solve Equation 86, an implicit method for the quasi-static time instances is combined with an explicit time integration method. This is necessary, because the material properties keep changing during cooling. Fortunately, the time step size tends to be relatively large as it is mainly determined by the temperature dependence of the material properties.

#### Quasi-static time step solution

Supposing that Equation 86 is fulfilled for arbitrary  $\delta\mathbf{u}$ ,  $\delta\mathbf{u}$  is eliminated from the equation so that

$$\mathbf{\Pi} = \mathbf{f}_{\text{int}} - \mathbf{f}_{\text{ext}} = \mathbf{0} \quad (101)$$

can be solved by Newton method. For every time step, starting with displacements vector  $\mathbf{u}_0$ , the updated displacements vector  $\mathbf{u}_1$  is calculated by developing  $\mathbf{\Pi}(\mathbf{u}_1)$  in a Taylor series

$$\mathbf{\Pi}(\mathbf{u}_0) + \left. \frac{\partial \mathbf{\Pi}}{\partial \mathbf{u}} \right|_{\mathbf{u}_0} (\mathbf{u}_1 - \mathbf{u}_0) = \mathbf{0}, \quad (102)$$

which is repeated until  $\mathbf{\Pi}(\mathbf{u}_1)$  becomes sufficiently small.

### Explicit time integration

The forward Euler method with an adaptive control of the time step  $\Delta t$  is then applied for the time integration, in which the solution is compared to the solution obtained with half the step size.<sup>20</sup> A time step is accepted if

$$2 \geq \left( \frac{2^q}{2^q - 1} \frac{\max(|\mathbf{u}(t + \Delta t, \Delta t) - \mathbf{u}(t + \Delta t, \frac{\Delta t}{2})|)}{\epsilon} \right)^{\frac{1}{q+1}} \quad (103)$$

is fulfilled, in which  $q$  and  $\epsilon$  are fixed numerical parameters [119]. After every accepted time step,  $\boldsymbol{\theta}$  is inspected to determine, if an update of  $\mathbf{K}$  is necessary.

---

<sup>20</sup>The time integration is necessary because the strain components and the stiffness matrix in Equation 93 are time-dependent.

## 4 Material examination

The following chapter focuses on the validation of the model discussed in Section 3.1 and the acquisition of the introduced material parameters using hardness testing and hot tensile testing.

### Investigated carbon steel

A 0.54 % carbon steel is exemplarily investigated, which can be found in automotive applications, for instance. Table 2 lists the chemical composition, of which the carbon content in particular is relevant for the hardening. Based on the conventional CCT diagram in Figure 25, the investigations are carried out for two cooling rates, at which different microstructures are formed.

### Existing data and tests

Körner and Jüttner [125] investigated the frictional characteristics at different rotational speeds in RFW within a research project at Otto von Guericke University Magdeburg. Within the scope of the project, thermal measurements during RFW and hardness mappings of welds have been carried out, which shall be used to validate the RFW material simulation in Section 4.1. Körner and Jüttner [125] also conducted hot tensile tests with continuous heating to investigate the flow properties. In Section 4.2, the evaluation of the tensile tests is enhanced and the testing routine is transferred to tests with continuous cooling for own experiments. The major advantage of using a non-isothermal testing routine is that more data points for the determination of the Carreau model can be gathered in a single test. Deforming the sample is inevitable, but based on the effect of deformation found in Section 3.1, the resulting hardness is less sensitive regarding  $\varepsilon_{pl}$  than regarding to  $\dot{\theta}$ . More than 80 tensile tests are evaluated in total.

Table 2: Chemical composition of the investigated carbon steel according to the material delivery certificate

	C	Si	Mn	P	S
% <sub>mass</sub>	0.54	0.21	0.63	0.008	0.006

## 4.1 Hardness measurements in welds

Carbon steel shafts ( $d_0 = 20.5$  mm,  $A_0 = 330$  mm<sup>2</sup>) were joined using RFW. The different process parameters are listed in Table 3. Beginning with the reference process variant  $\mathcal{A}$ , the friction and forging forces  $F_1, F_2$  have been adjusted by  $\pm 25$  % for the variants  $\mathcal{B}$  and  $\mathcal{C}$ . The rotational speed  $n_0$  is varied in-between 1000 and 2500 min<sup>-1</sup> and the friction feed  $s_3$  is set 4.0 mm for all variants. Thus,  $\mathcal{A}$ ,  $\mathcal{B}$  and  $\mathcal{C}$  have different heat inputs  $Q$ .

### Validation of the process simulation temperatures

On the surface of the stator component of  $\mathcal{C}$ , four type K thermocouples have been installed. The validation of the temperatures predicted by the RFW simulation is essential for the subsequent hardness predictions. The first thermocouple is positioned 10.0 mm away from the initial weld interface and the remaining thermocouples are positioned axially spaced by 2.5 mm from one another. If the thermocouples are installed closer to the WCZ, they detach during welding due to the deformations.

The measured temperatures are plotted together with the RFW simulation results in Figure 24. Based on the match of the curves, the model is capable to predict the heat generated in RFW. The heating rate, the peak temperature and the cooling rate at the first thermocouple are precisely predicted. With an increasing distance from the WCZ and progressing measurement duration, the offset of the temperature curves slightly increases as deviations between the true and the assumed heat exchange with the RFW machine propagate with time. The heat input of process  $\mathcal{C}$  is about 35 kJ and of the processes  $\mathcal{A}$  and  $\mathcal{B}$  about 22 kJ.

Table 3: Excerpt of the RFW process parameters used by Körner and Jüttner [125] to investigate the frictional characteristics at different rotational speeds

Process	$F_1/A_0$ [MPa]	$F_2/A_0$ [MPa]	$s_3$ [mm]	$n_0$ [rpm]
$\mathcal{A}$	120	240	4.0	1000
$\mathcal{B}$	150	300	4.0	1500
$\mathcal{C}$	90	180	4.0	2500

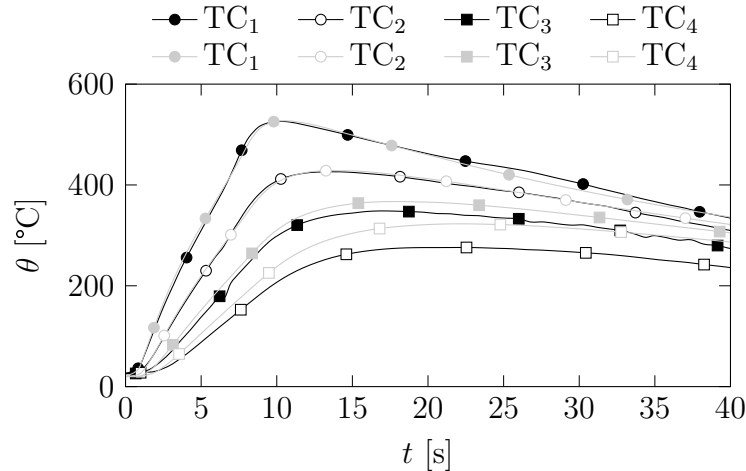


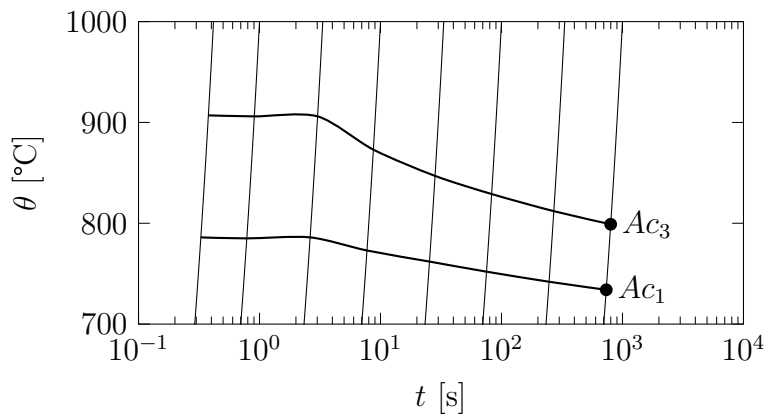
Figure 24: Measured temperatures on the surface of weld  $\mathcal{C}$  during the RFW process using thermocouples ( $TC_i$ , black) and the RFW simulation (grey)

### Material model parameter identification

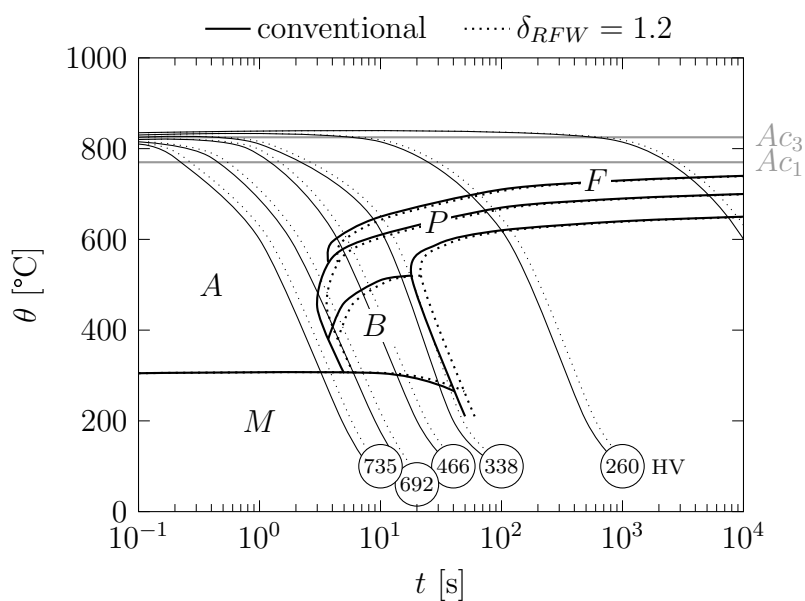
For the hardness estimations by the RFW material simulation, the model is trained on the TTA and CCT diagrams depicted in Figure 25 [86, 126]. Referring to Equation 25 of the RFW material simulation model, the delay times are determined as  $\tau_1 = 0.003$  and  $\tau_3 = 3$  s using aforementioned optimization routine. The simulated austenitization progress for different heat-up rates is illustrated in Figure 26 and it matches well with the start and finish temperatures in Figure 25 (a). To account for the transformation kinetic changes due to deformation and the high peak temperatures during RFW,  $\delta_{RFW} = 1.2$  is assigned. The shifted transformation temperatures are shown as dotted lines in Figure 25 (b). Figure 27 shows the delay times  $\tau_\alpha$  of different cooling rates to reproduce the CCT diagram shifted by  $\delta_{RFW} = 1.2$ . Based on the hardness values in the CCT diagram, the hardnesses of the individual phases are calculated, which are close to those calculated based on the chemical composition that are listed in Appendix B for comparison.

### Hardness results

A mapping of the measured HV1 hardnesses is shown in Figure 28. In the experiments and in the simulations, the HAZ ends at the root of the weld flash. Particularly high hardnesses are measured on the axis of rotation, which should be related to variations in the base material, due to the manufacturing of the round bar material. Overall, the simulations reproduce the hardness fields sufficiently well for the tested RFW process parameters. The size of the HAZ and the hardness trends match quantitatively. As expected, the variants  $\mathcal{A}$  and  $\mathcal{B}$  have similarly high hardnesses, because of to the identical heat input. The variant  $\mathcal{C}$  is comparatively soft, but softening in the HAZ is not observed, as the initial material hardness is only about 240 HV.



(a) TTA diagram



(b) CCT diagram

Figure 25: Phase transformation diagrams (austenitization at 840 °C) [86, 126]. The full CCT diagram with all phase fractions is shown in Figure 10

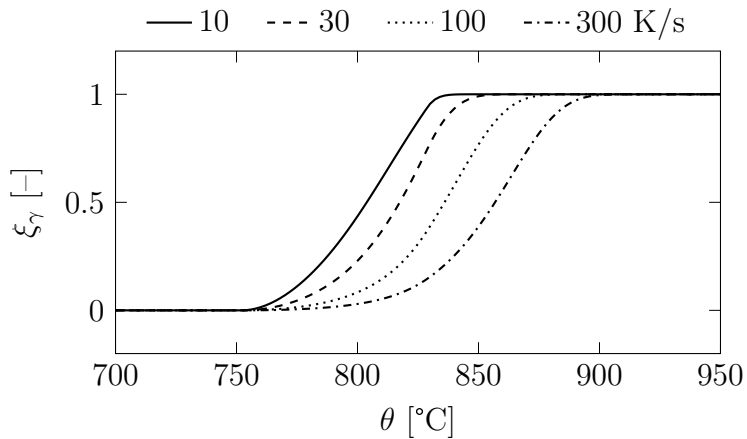


Figure 26: Reproduction of the austenitization progress for different heating rates using the RFW material simulation model with  $\tau_1 = 0.003$  and  $\tau_3 = 3$  s



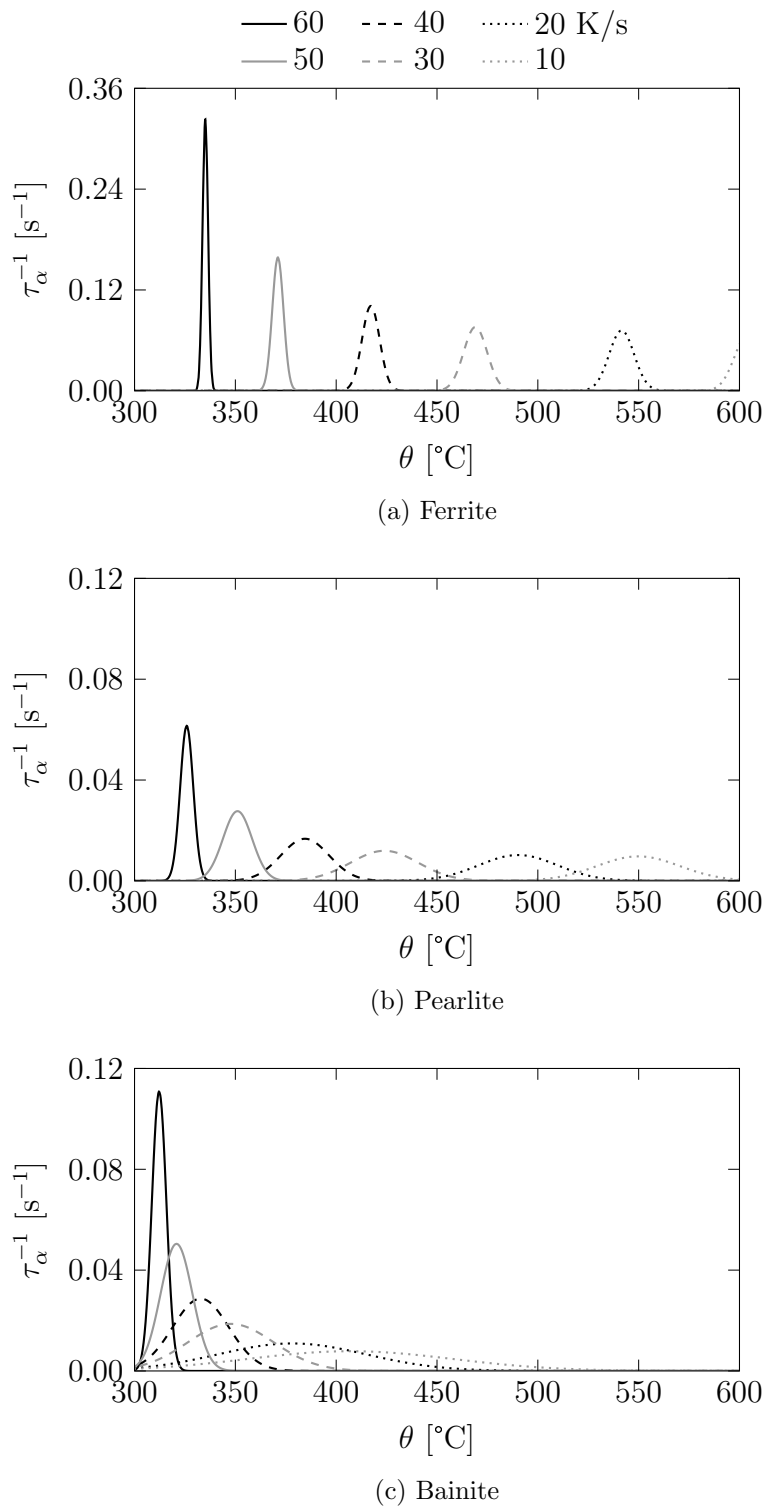


Figure 27: Inverses of the fitted delay times  $\tau_\alpha$  for the diffusive transformations during cooling for selected cooling rates

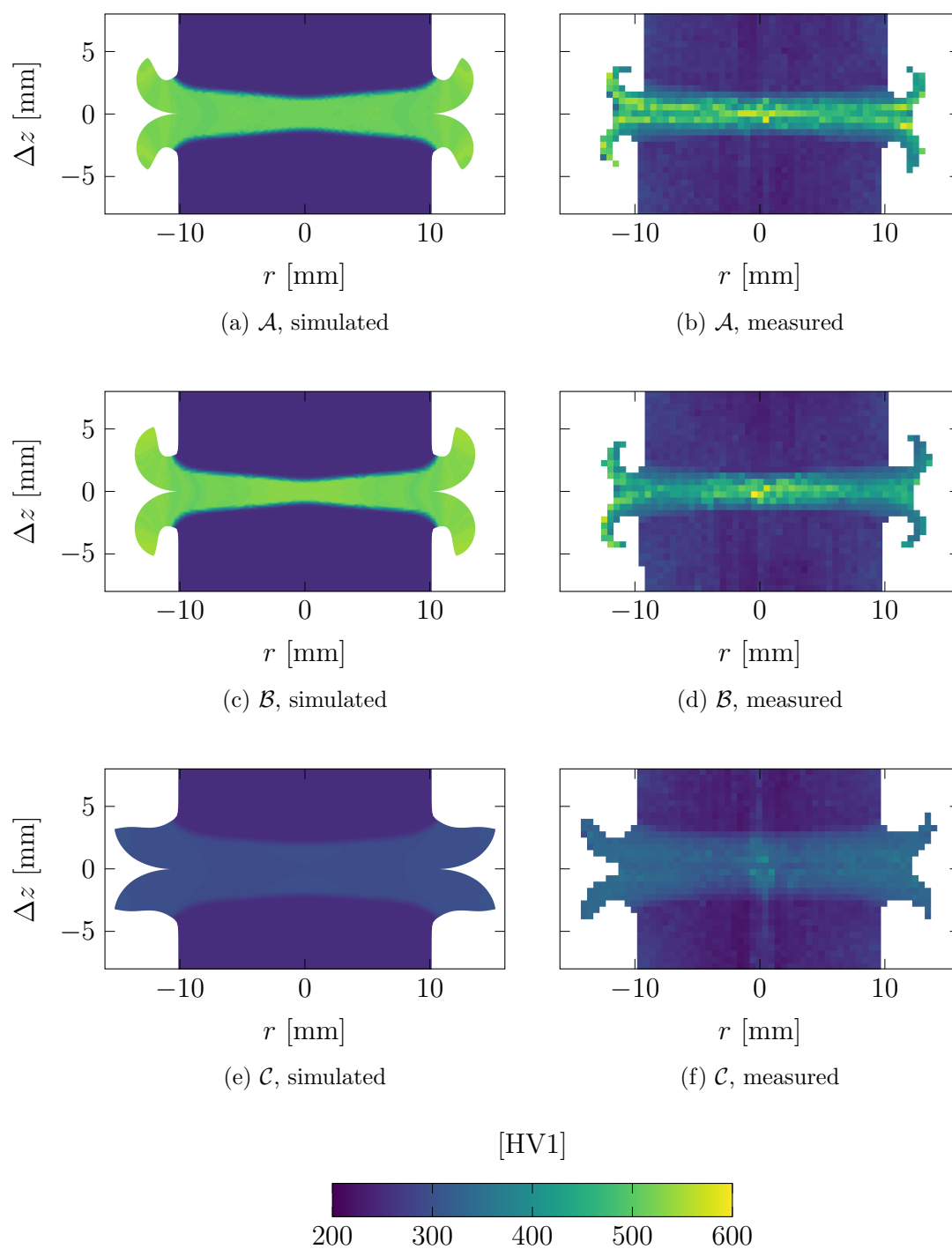


Figure 28: Vickers hardness mappings of welds produced with different RFW process parameter settings by Körner and Jüttner [125] and of the corresponding RFW material simulations

## 4.2 Uniaxial tensile testing

Uniaxial tensile tests with continuous heating and cooling were carried out at Otto von Guericke University Magdeburg. Part of the machine capabilities is the execution of displacement controlled tensile tests, while at the same time the sample temperature can be varied using conductive heating.

### Methodology

The machine setup and the installed specimen are illustrated in Figure 29.<sup>21</sup> Within the machine, the force  $F(t)$  required to produce a specified stroke  $s(t)$  is captured. An additionally installed extensometer monitors the diameter  $d(t)$  in the axial center of the sample. At the axial center, the surface temperature  $\theta(t)$  is measured by a weld-on thermocouple, which is used to control the amperage for the conductive heating. The initial diameter in the monitored area is  $d_0 = 6$  mm, which has been chosen based on the permissible force. To realize cooling rates of 30 K/s, two air cooling jets are positioned at  $120^\circ$  in radial direction, which aim at the full measurement length. If necessary, the conductive heating is used to reheat the sample to maintain a constant  $\dot{\theta}$ .

Table 4 provides an overview of the examined temperatures ranges, the temperature change rates and the stroke rates of all tests. Figure 30 schematically illustrates the temperature and stroke control for the heating and cooling tests. Both have in common that a 0.3 mm pre-stroke is applied to overcome the elastic range. In the heating tests, the pre-stroking is performed at a constant temperature before heating up further. In the continuous cooling tests, the cooling process is not interrupted to apply the prestroke. To determine  $\sigma$ - $\dot{\epsilon}$ - $\theta$  triples, different stroke rates and temperature ranges are combined. Figure 31 lists all tests for 5 K/s cooling. The others are documented in Appendix D.

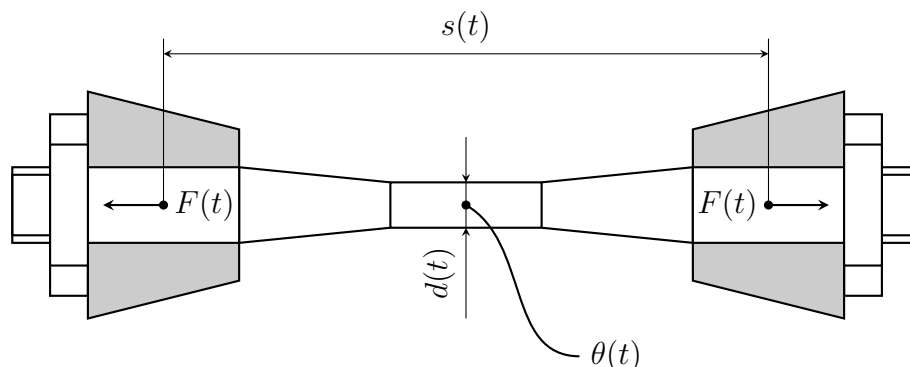


Figure 29: Installed tensile tests specimen for hot tensile tests during continuous heating and cooling and the monitored parameters

<sup>21</sup>A Gleeble 3500 testing system has been used.

Table 4: Summary of test conditions in the non-isothermal tensile tests during continuous heating and cooling

		Heating	Cooling
$\theta$	[°C]	$\geq 300$	$\leq 800$
$\dot{\theta}$	[K/s]	1 – 2000	5, 30
$s_0$	[mm]	0.3	0.3
$\dot{s}$	[mm/s]	0.003 – 30	0.03 – 0.3

The stroke rates  $\dot{s}$  are in the range in-between 0.003 up to 30 mm/s in the continuous heating routines, which is narrowed down to 0.03 and 0.3 mm/s for the continuous cooling routines, because the deformations at temperatures below 800 °C are typically less severe in RFW. The evaluation temperature ranges are estimated as such that the fracture strain is not to be exceeded. In the cooling experiments, the specimen is heated in 5 s to 1200 °C and hold at this temperature for 2 s more. After that, the cooling process is triggered. The temperature range above 800 °C is excluded from the evaluation range in the runs with continuous cooling, since no transformations are to be expected.

### Mathematical evaluation

Based on the measured data, the longitudinal stress

$$\sigma = \frac{4F}{\pi d^2} \quad (104)$$

and the radial plastic strain rate

$$\dot{\epsilon}_{pl,r} = \frac{d}{dt} \left( \ln \frac{d}{d_0} \right) = \frac{\dot{d}}{d} \quad (105)$$

are evaluated. Under the condition of volume constancy, the plastic Mises strain rate

$$\dot{\epsilon}_{pl} = \left| 2 \frac{\dot{d}}{d} \right| \quad (106)$$

is derived. By this, the true stress  $\sigma$ , the equivalent strain rate  $\dot{\epsilon}_{pl}$ , and the temperature  $\theta$  are evaluated in the same cross section, without relying on  $s(t)$ . In order to fit the model according to Section 3.1.2, the characteristic point  $(\sigma_C, \dot{\epsilon}_C)$  and the reference stress  $\sigma_0(\theta, \dot{\epsilon}_0)$  are identified in a one-step optimization through varying  $(\sigma_C, \dot{\epsilon}_C)$ . The stresses  $\sigma_0(\theta, \dot{\epsilon}_0)$  are instantly derived by fitting the best matching isothermal straight lines of the measuring points going through  $(\sigma_C, \dot{\epsilon}_C)$ . To compensate the imbalance of the number of measuring points  $i$  in the evaluation, the triples are grouped in temperature

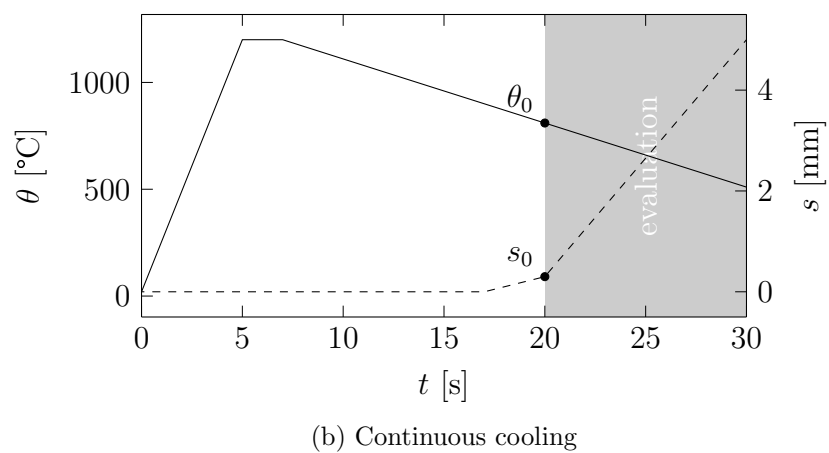
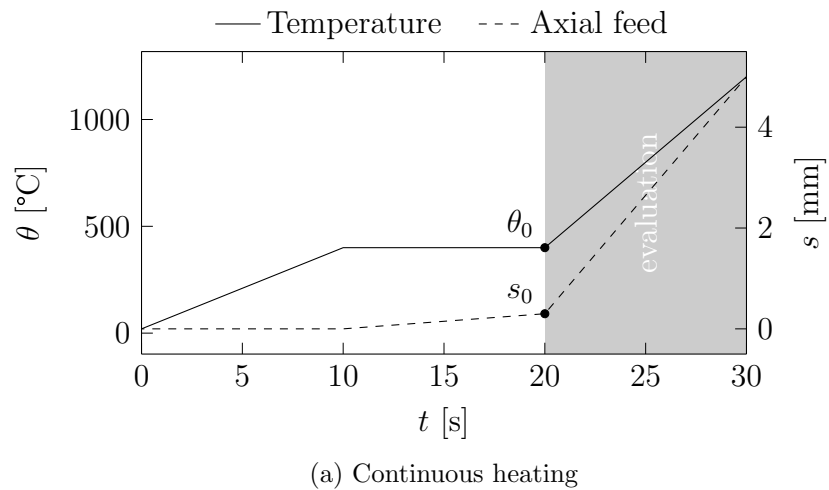


Figure 30: Thermal profiles and axial strokes in the uniaxial tensile testing routines during continuous heating and cooling

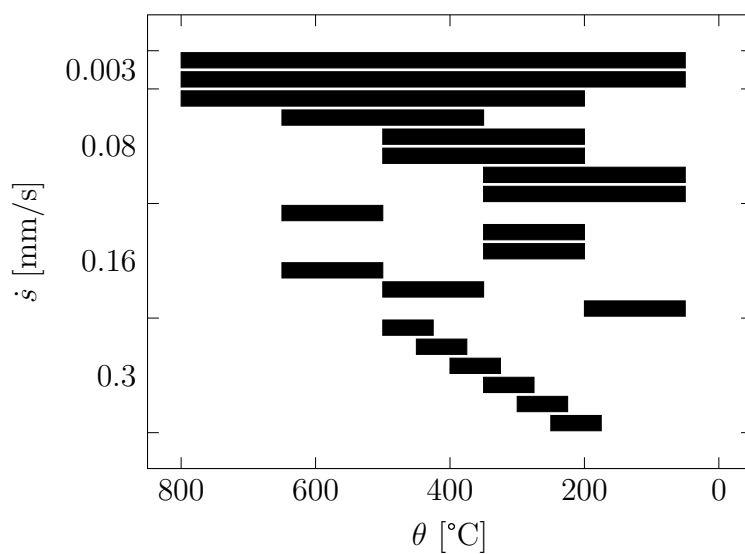


Figure 31: Examined temperature and stroke ranges of all individual tests at a constant cooling rate of 5 K/s

classes  $j$ , each spanning 25 K. The coefficient of determination

$$R_j^2 = \frac{\sum_i (\lg \sigma(\theta_i, \dot{\epsilon}_i) - \lg \bar{\sigma}_j)^2}{\sum_i (\lg \sigma_i - \lg \bar{\sigma}_j)^2} \quad (107)$$

for each classes is evaluated and those are then summarized in the objective function

$$Z = - \sum_j R_j^2 \quad (108)$$

### Homogeneity of cooling

The evaluation of the uniaxial tests requires the homogeneity across the diameter. In the heating experiments this is guaranteed by using conductive heating and a vacuum. In contrast to this, the cooling is realized through a combination of conduction through the specimen itself and convection via its surface, which is more likely to cause a thermal gradient in radial direction. As air is used as the cooling medium, creating a vacuum is not practical. To quantify the homogeneity of cooling, the cross sections of specimens cooled with 5 and 30 K/s have been examined. As seen in the macrographs in Figure 32, two different microstructures are formed that appear to be homogenous in the whole cross section. The measured hardness values are provided in Appendix C. The average hardness in the initial conditions  $\bar{H}_0$  of the base material is 332 HV0.1. In the samples cooled with 5 K/s, this value slightly drops to  $\bar{H} = 311$  HV0.1. The distribution is fairly homogeneous in the measured region, varying in-between 250 and 370 HV0.1. The peak hardness is not on the surface, where the highest cooling rates are expected, but on the center axis of the sample, which shall be attributed to initial inhomogeneities. The air cooling jets are well capable to generate cooling rates of 30 K/s and high hardnesses are found over the whole diameter. Towards the end of the measurement length, 2 mm off-center, high hardnesses of 700 HV0.1 are still reached.

#### 4.2.1 Full heating and cooling evaluation

The best fitting points  $(\sigma_C, \dot{\epsilon}_C)$  for heating and cooling with 5 and 30 K/s are listed in Table 5. For a better comparability of the quality of the models, the  $R^2$  is evaluated based on all triples of the experiments. At values in the range of 0.9, the heating and cooling flow properties are similarly well reproduced, confirming the general suitability of this model for heating and cooling. The resulting Carreau model for heating is plotted in Figure 33, together with 1,000 randomly selected points out of the more than 500,000 measured triples. The equivalent plots for cooling with 5 and 30 K/s are shown in Figure 34. The tabulated values for  $\sigma_0(\theta)$  and  $n(\theta)$  for  $\dot{\epsilon}_0 = 0.001 \text{ s}^{-1}$  can be found in Appendix D.

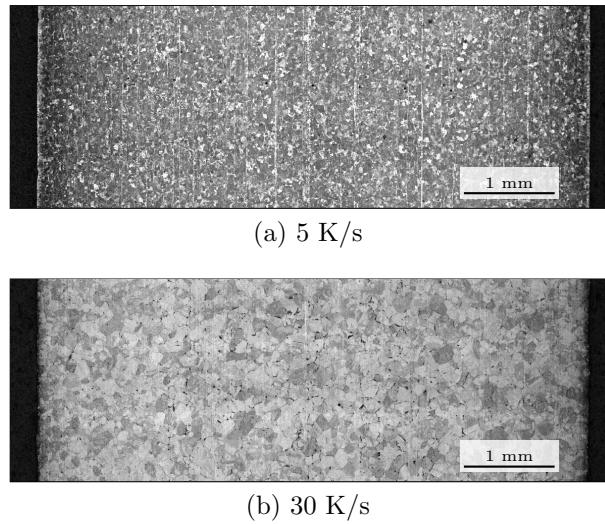


Figure 32: Macrographs of the longitudinal cross sections found after cooling at two different rates

Table 5: Correlation of the experimental data and the individually fitted Carreau models based on Equation 107

	Heating	Cooling	
		5 K/s	30 K/s
$\sigma_C$	$1.53 \cdot 10^3$	$4.03 \cdot 10^3$	$1.21 \cdot 10^5$
$\dot{\epsilon}_C$	$5.51 \cdot 10^6$	$7.06 \cdot 10^6$	$2.80 \cdot 10^8$
$R^2$	0.9084	0.9428	0.8830

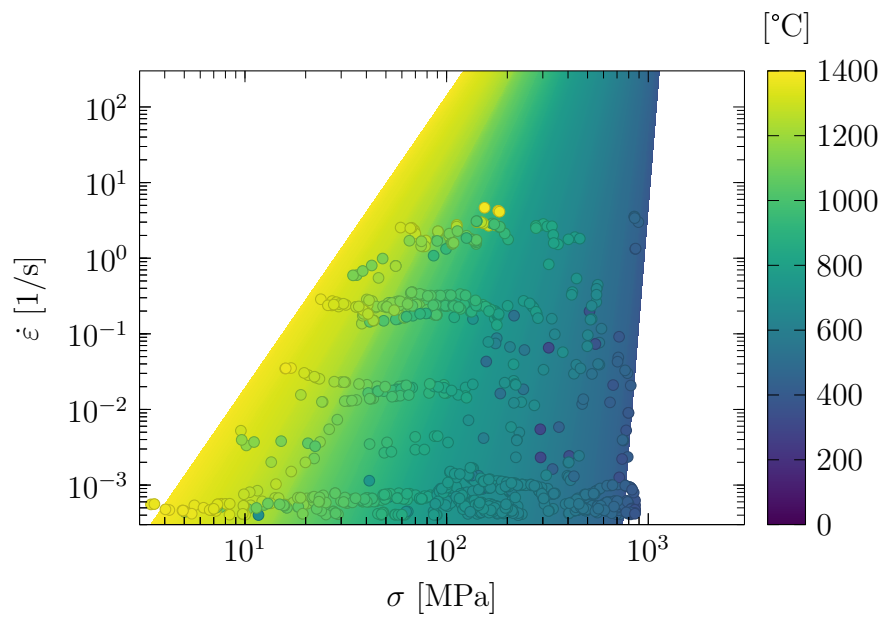
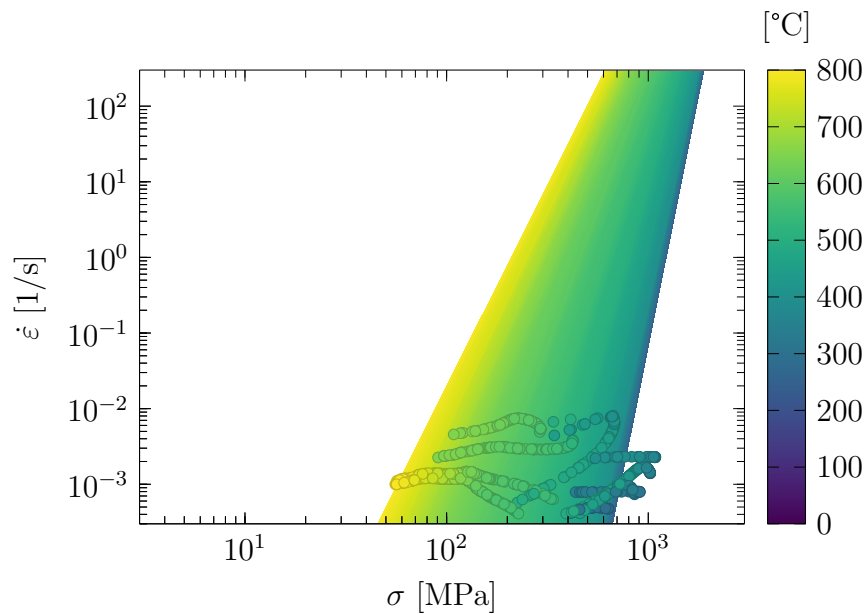
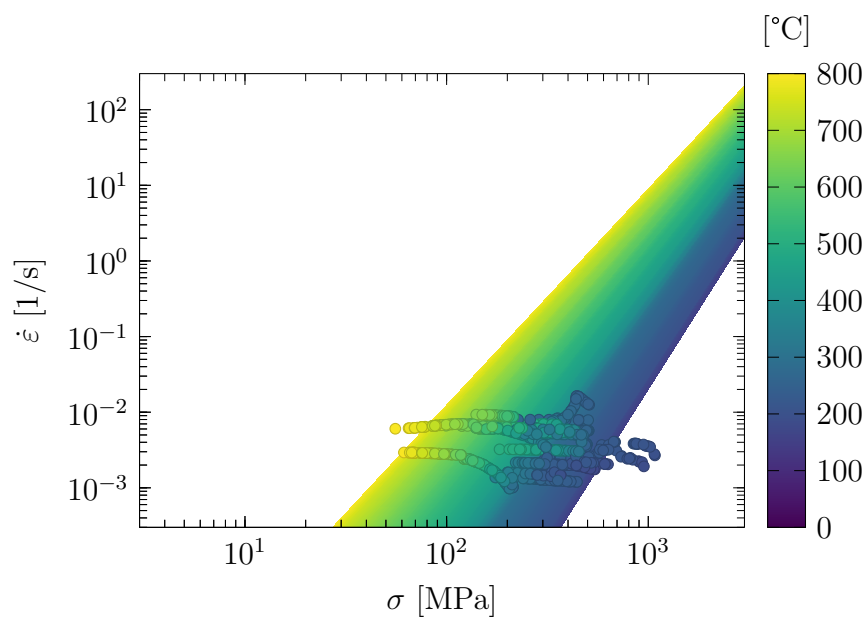


Figure 33: Plastic material characteristics examined during continuous heating the carbon steel specimens



(a) Cooling (5 K/s)



(b) Cooling (30 K/s)

Figure 34: Plastic material characteristics examined during continuous cooling the carbon steel specimens



## 4.2.2 Approximated cooling evaluation

Figure 35 contains a comparison of the reference stresses  $\sigma_0$  of all experimentally fitted models and the approximation models for  $\sigma'_0$  from Section 2.3.2. The experiments confirm that the curves are shifted to the left during cooling, because austenite is still present in the microstructure at lower temperatures. When cooling with 5 K/s, the  $R^2$  is as good as for the experimentally fitted model (Table 6). For 30 K/s, the trend of the reference flow stress in the experiments is also well reflected. Quantitatively,  $R^2$  drops to 0.5, because the steep increase of  $\sigma_0$  starts at 50 °C too high temperatures. For comparison, if the model determined for heating is also applied without any modifications during cooling, a  $R^2$  of 0.78 respectively -1.44 results, the latter implying a scalar flow stress is a better fit. Thus, the approach in Section 3.1.3 offers a significant improvement, when applying the model to cooling, without requiring a big experimental overhead.

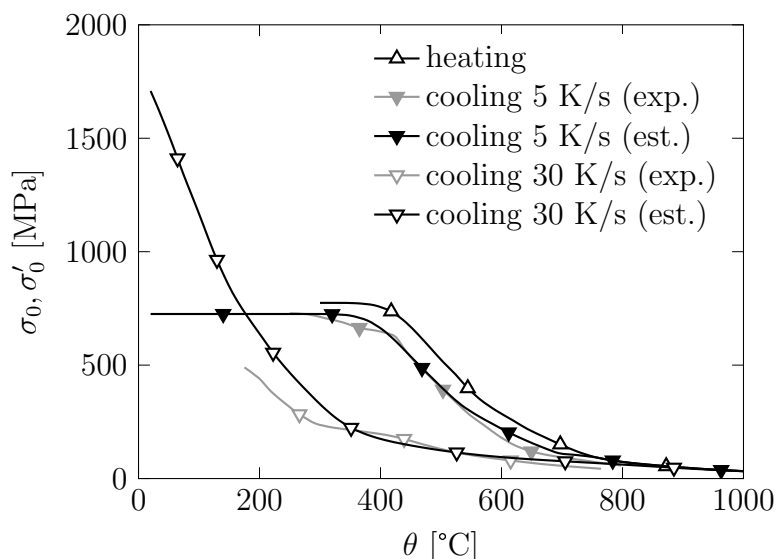


Figure 35: Reference flow stresses  $\sigma_0, \sigma'_0$  at  $\dot{\epsilon}_0 = 1 \cdot 10^{-3} \text{ s}^{-1}$  during heating and cooling determined in the experiments (exp.) and the model established in Section 2.3.2 (est.)

Table 6: Correlation of the experimental data and estimated Carreau models for cooling based on Section 2.3.2

	Heating	Cooling	
		5 K/s	30 K/s
$\sigma_C$ [MPa]	$1.53 \cdot 10^3$	$1.78 \cdot 10^3$	$3.62 \cdot 10^3$
$\dot{\epsilon}_C$ [ $\text{s}^{-1}$ ]	$5.51 \cdot 10^6$	$4.73 \cdot 10^6$	$2.75 \cdot 10^8$
$R^2$ [-]	0.9084	0.8926	0.4836



---

## 5 Application cases

To validate the RFW structural simulation model, it has been used to simulate several RFW applications, which are subsequently presented and for which the residual stress related particularities are pointed out. For confidentiality reasons, some of the presented applications might show an iteration step that has been refined afterwards. For the same reason, not all dimensions and process parameters might be provided. The examples have in common that they are related to lightweight designs, in which residual stress related problems are more susceptible to arise.

Starting with the example *Overlap friction welding of sheets* (Section 5.1.1), the capability of the process simulation and the evaluation of the local action is demonstrated. The *Planetary carrier* (Section 5.1.2) shows a component with a sophisticated design following the same RFW concept and the differences to the example from Section 5.1.1 are pointed out. Residual stress measurements are not available for this application, but theoretical and practical findings are used for a plausibility check of the calculated stress fields. The examples of the *Constant velocity joint* (Section 5.2.1) and the *Hybrid brake disc* (Section 5.2.2) focus on welds in which cracks were found right after welding, before mechanical testing, presumably due to high residual stresses. The examples of *Welding of Al-Fe alloy rods* (Section 5.3.1) and the *Lightweight gear wheel* (Section 5.3.2) highlight the problem of high residual stresses when joining aluminum alloys and steels, the combination of which is possible by using RFW. Because own measurements of residual stress fields are not carried out, the example of *Inertia friction welding of large rings* (Section 5.4) focuses on RFW of a nickel-based superalloy, for which material data and residual stress fields measured using the neutron diffraction method are published.

### 5.1 Overlap friction welding

The patent US 4 087 038 [127] by the Japanese inventor Yagi, published in 1978, describes a RFW process that has recently been referred to as *overlap friction welding* (OFW). As shown in Figure 36, an axial force pushes a rotating inner part of larger outer diameter  $D$  at its planar front side against an outer part of smaller inner diameter  $d$  and through it,

until it reaches its targeted end position. The radial overlap of both parts

$$O = \frac{D - d}{2} \quad (109)$$

shall be selected according to the targeted end position. Figure 36 also shows that the weld flash forms like in conventional RFW on all sides, although a conical WCZ is formed in OFW. To apply OFW, conventional RFW machines can be used as the process parameterization does not have to be altered necessarily (Section 2.1.1). OFW indeed offers several advantages over conventional RFW. Through the conical WCZ, a radial force component

$$F_r \approx \frac{F}{\tan \alpha} \quad (110)$$

is introduced, which keeps increasing in the process and helps to ensure good concentricity of both parts (Figure 37). Additionally, more compact and lighter designs are feasible, profiting from the increased WCZ size. Because the initial interface is comparatively much smaller than conventional and conical friction weldings, the self-cleaning is enhanced and the initial torque peak is lowered too. Yagi [127] specifies appropriate ratios  $d/D$  in-between 20 and 99 %. The aforementioned advantages become greater the smaller the overlap  $O$  is, which on the other hand increases the sensitivity of the RFW process. A risk related to the overlap  $O$  being too small is that the inner component can be pushed through the outer component uncontrollably.

A special characteristic of OFW is that it has similarities to press fitting and deep drawing simultaneously. Because of the diameter difference, the press-fit analogy is more intuitive, which provokes tensile residual stresses in the outer component in the tangential direction and compressive ones in the inner component. In the radial direction, the inner and outer component are both compressively stressed. Regarding the deep drawing analogy, part of

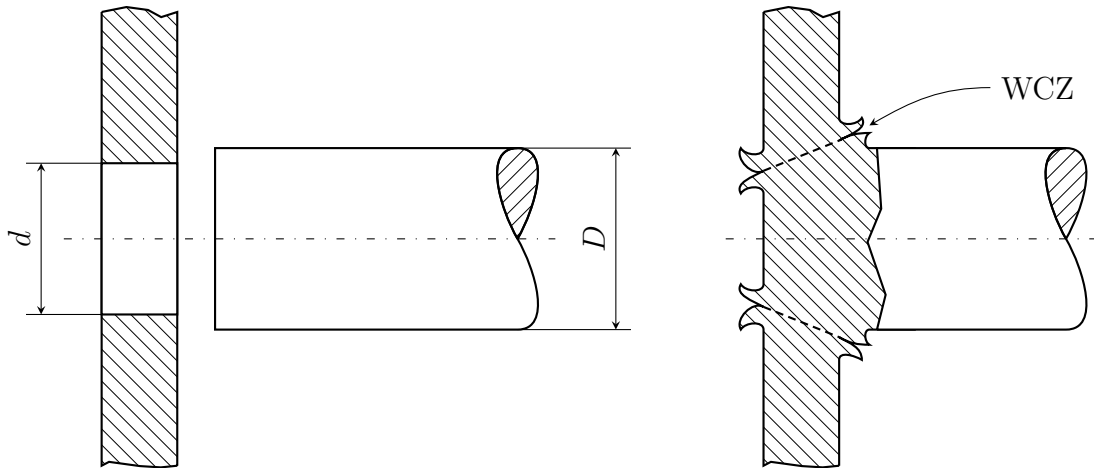


Figure 36: Initial and final part configuration in overlap friction welding (OFW)

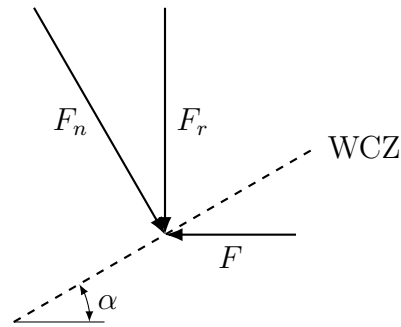


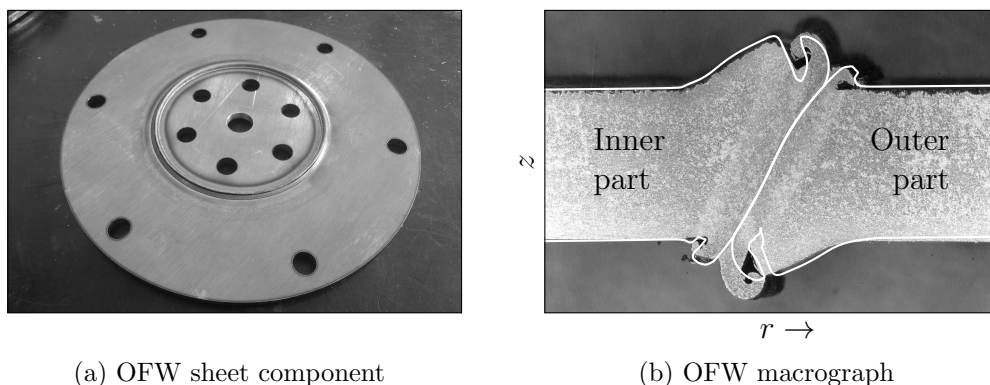
Figure 37: Radial force introduction by the conical WCZ in OFW, which keeps increasing within the RFW process

the material is moved in the reverse direction of the material extrusion direction, in which the weld flash forms in OFW. This deep drawing causes compressive residual stresses in the tangential direction in the outer component, matching the empirical observation that gearing components have reduced outer tothing diameters after OFW.

The application of OFW is not limited to the combination shown in Figure 36 of a solid shaft and a flange element. Powertrain applications with other geometries are a crankshaft of a diesel engine, a drive pinion and a planetary carrier by Daimler AG [128, 129, 130, 131]. This process has also been adapted to weld tubes with different kinds of flanges and to weld constant velocity joints for drive shafts by IFA Group [132, 133]. The planetary carrier and the constant velocity joint will be presented in Section 5.1.2 and Section 5.2.1.

### 5.1.1 Overlap friction welding of sheets

The evaluation of the local action is demonstrated for OFW of two sheet components, allowing to focus on the geometric effects. Pictures of a welded part are provided in Figure 38. The components are lasered out of 4 mm thick sheets made of S235 structural steel. The lasered holes in the inner and outer component are necessary to transmit



(a) OFW sheet component

(b) OFW macrograph

Figure 38: Picture and macrograph an OFW component made of two sheet components

the frictional torque.<sup>22</sup> The contour determined using the RFW simulation is included as a white outline in Figure 38 (b). Especially the deflection of the sheets in the  $z$ -direction is well captured, resulting from the high process forces, the lack of support by the toolings and the thermal softening of the steels. Figure 39 shows the maximum temperature distribution within the RFW process, in which it is seen that the inner component becomes slightly hotter due to its smaller volume. In Figure 40 (a) it is seen that plastic strains in the WCZ rapidly increase at the beginning of the forging stage and then remain almost constant at a level well above  $\varepsilon_{\min}$ . This is also about the same time the spindle completely stops, therefore no more heat is generated by friction, and the component cools down homogeneously along  $r$  as seen in Figure 40 (b). Unlike the contact pressure plot of the solid shaft in Figure 23, there is a contact pressure minimum in the radial center of the WCZ in Figure 40 (c) – instead of a pressure maximum – which is due to the  $S$ -shape of the WCZ seen in Figure 38 (b).

The residual stresses fields identified using the RFW structural simulation are plotted in Figure 41, revealing that the tangential residual stresses are dominating in both sheets. While the RFW-affected zone is completely covered by tensile residual stresses in Figure 41 (c), the more outer region of the outer component is under compression, which corresponds to the aforementioned deep drawing analogy. The tensile radial residual stresses in Figure 41 (a) also confirm that the outer part is pulled inwards in OFW by the inner component. The radial stress profile of the inner component on the other hand indicates bending, causing a slight buckling of the welded components. The axial residual stresses in Figure 41 (b) are insignificantly small in comparison.

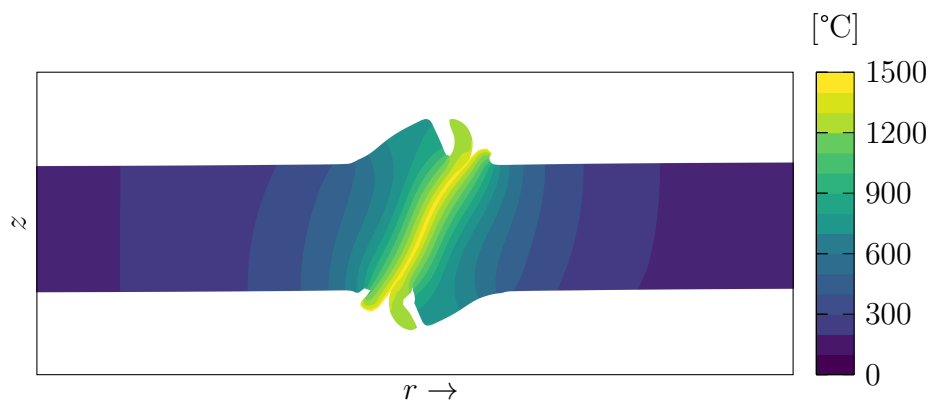
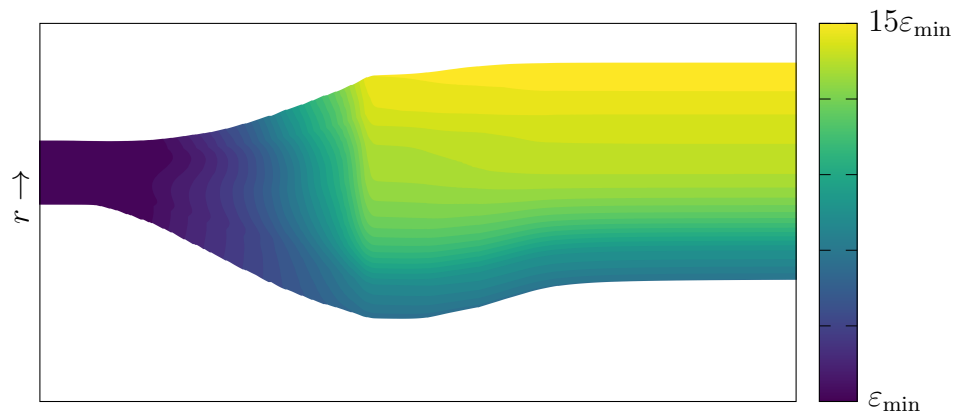
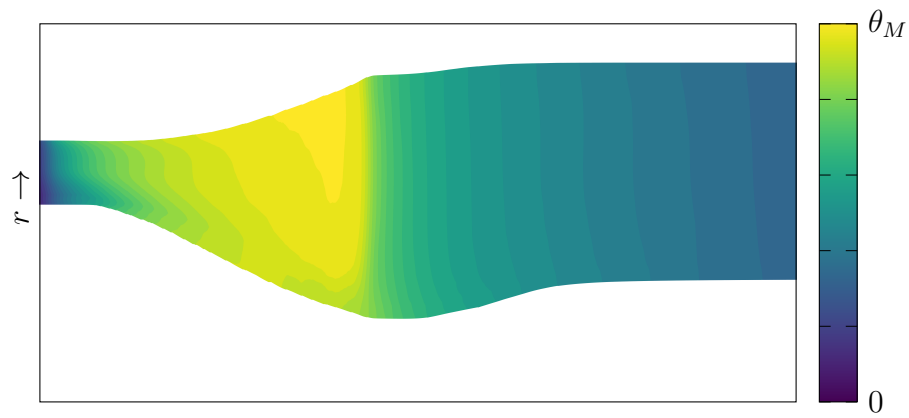


Figure 39: Maximum temperatures in the OFW component reached in the RFW process extracted from the RFW process simulation

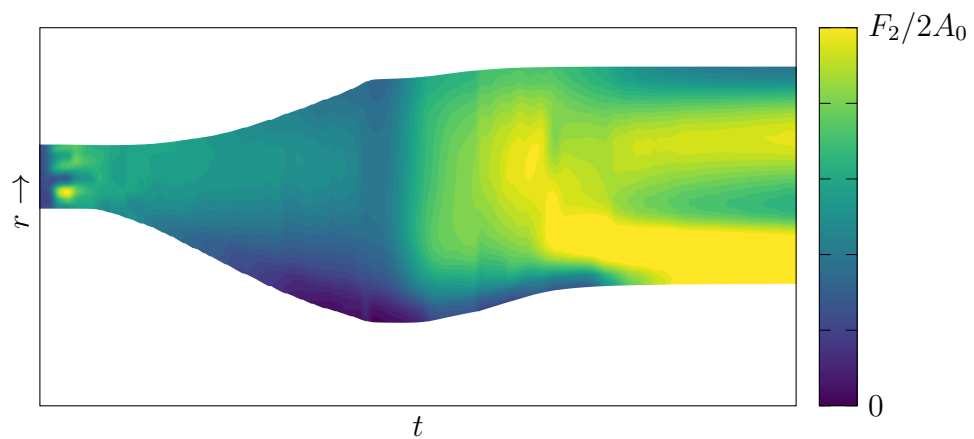
<sup>22</sup>The holes are also necessary to hold the component in the vertical RFW machine.



(a) Equivalent plastic strain



(b) Temperature



(c) Contact pressure

Figure 40: Local action (temperature, contact pressure and plastic strain) in the WCZ extracted from the RFW simulation of the weld in Figure 22

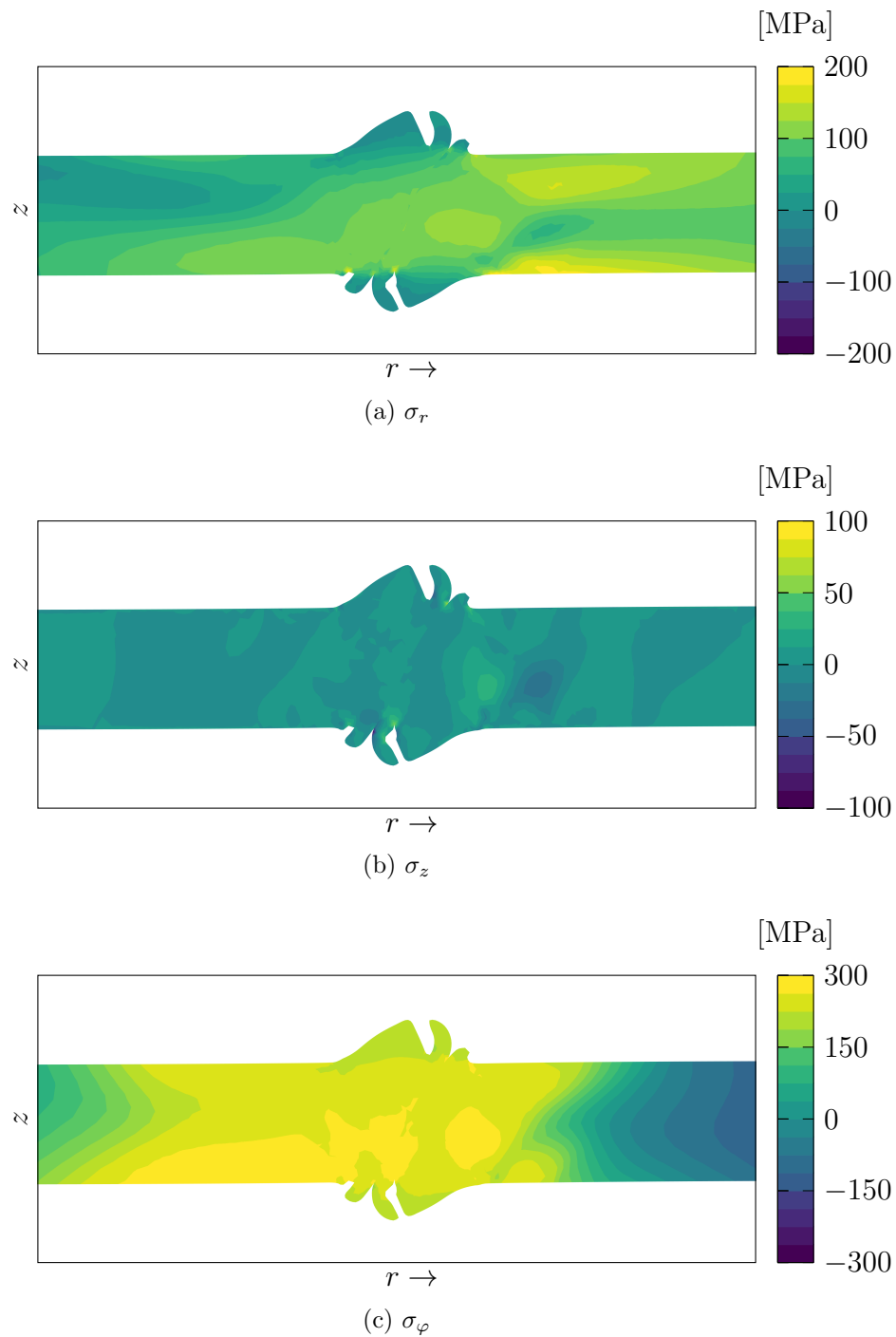


Figure 41: Residual stresses distribution in a sheet component produced by OFW



### 5.1.2 Planetary carrier

A recent OFW application is the planetary carrier, a macrograph of which is shown in Figure 42. The hub is made of micro-alloyed steel 30MnVS6 and the gear holder (outer component) is made of softer, unalloyed steel DD13. While the welding area is axisymmetric, further outside there are four holes to mount the gears and in-between those are four flanges that have to be neglected in the RFW simulations. Further information about this component has been published by Reinhardt [131]. In Figure 42 it can be seen that the weld interface is slightly curved, due to the different flow properties. The weld is well reproduced in the RFW process simulation, with the major difference being in the weld flash curling, which shall have an negligible effect on the residual stresses.

The estimated radial and tangential residual stress fields in the planetary carrier, shown in Figure 43 (a) and (c), are similar to those in the previous OFW sheets component. Again, the tangential residual stresses are of the highest magnitudes in this application, as the RFW-affected zone seeks to shrink more inwards than it actually can. Because the flow stress of the steel of the outer component is lower than that of the inner one, different residual stress levels are present after RFW in both materials. The different properties are also part of the reason for the deflection of the outer component in the  $z$ -direction at its inner diameter, while the flange of the inner component stays intact. The outer component side facing the hub is under higher tensile radial residual stresses than the other side, implying that it becomes slightly bended in the  $z$ -direction. The hub on the other hand is slightly bended inwards due to OFW, in the  $r$ -direction, due to the lack of radial support, which is seen in the axial residual stresses in Figure 43 (b). Meanwhile, the rest of the inner component is not as affected by the RFW induced residual stresses.

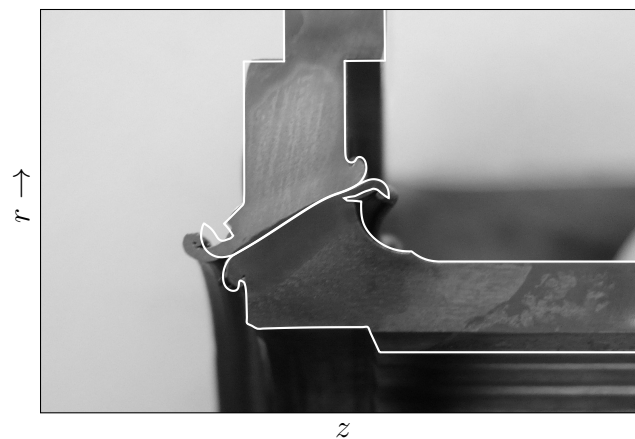


Figure 42: Macrograph of the friction welded planetary carrier by Reinhardt [131] and the RFW simulation results shown as white lines

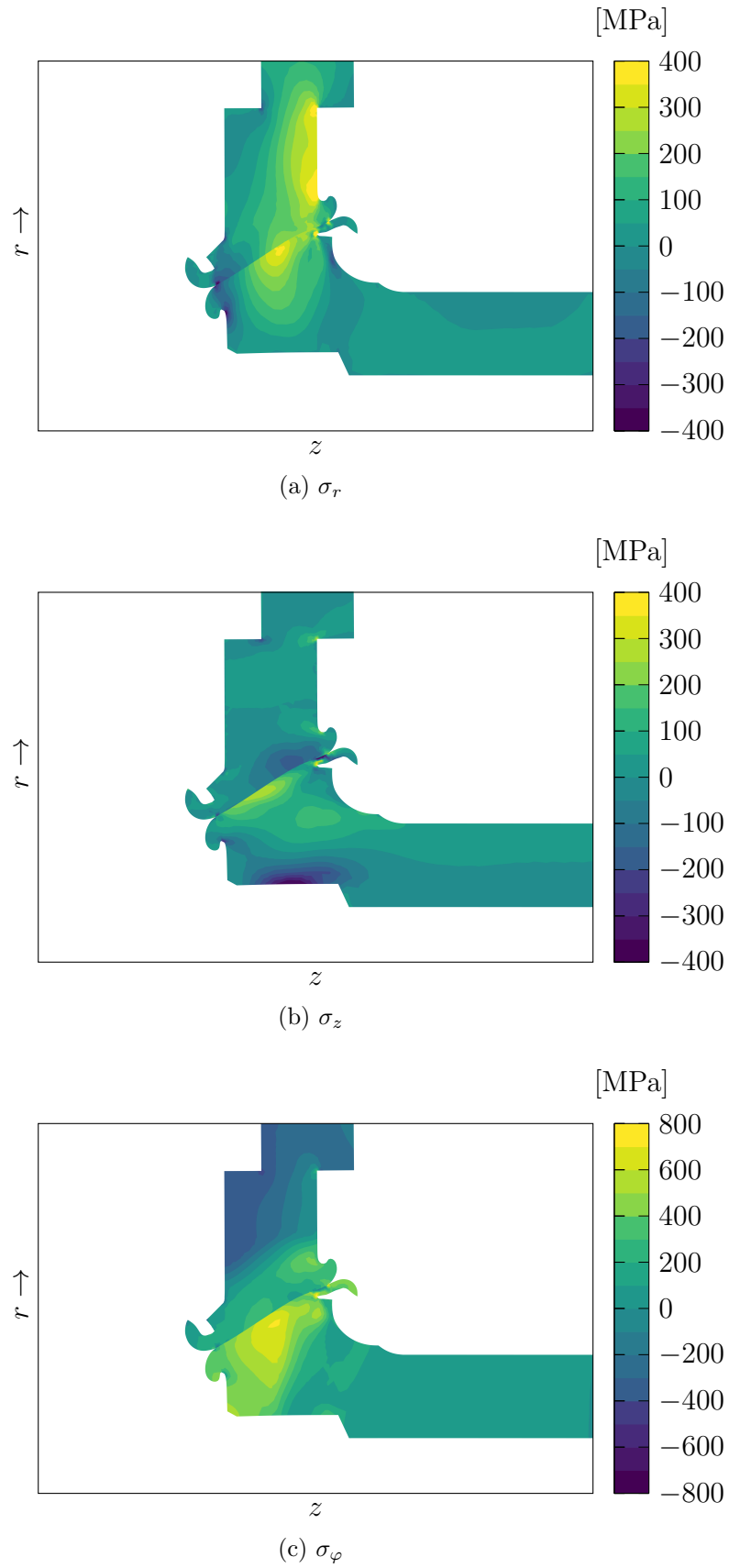


Figure 43: Residual stresses in OFW plate-hub configuration in a commercial planetary carrier

## 5.2 Heat throttle design

As illustrated in Figure 44, a groove can act as a *heat throttle* that minimizes the heat losses within the RFW process, enhancing the WCZ properties. This design feature is especially helpful, if two very different sized components shall be welded or if tempering effects in certain sections have to be prevented. Besides being beneficial in the RFW process, it can also serve the functionality of the welded component, if it is subjected to temperature loadings. The heat throttle can either be in radial or circumferential direction and definitely has to be taken into account in the structural design evaluation, due to its potential notch effect. Furthermore, it has to be considered that the temperature gradient within the components is steepened, increasing the inhomogeneity of the thermal expansions.

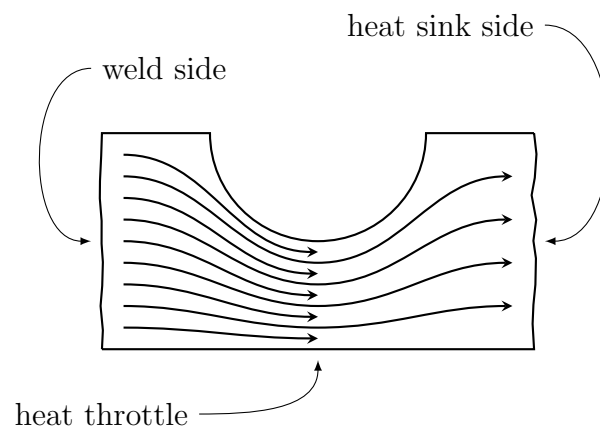


Figure 44: Heat throttle design concept to minimize heat losses in RFW by reducing the heat capacity and redirecting the heat flow

### 5.2.1 Constant velocity joint

One design including such heat throttle is patented in EP 3 241 642 [133] by IFA Group, illustrated in Figure 45. This joint design also makes use of the OFW process, which is ideal for the flux of force in this application. An initial chamfer is a slight modification to the OFW geometries presented in Section 5.1, which shall assist the self-centering of the components in the process beginning.

As introduced, the eponymous function of the heat throttle is the minimization of the heat losses within the RFW process. For the constant velocity joint presented here, the heat flowing into the so-called *support ring* must be kept low. The support ring is supposed to increase the overall stiffness to prevent bulging of the welded component due to the introduced radial force in OFW. Bulging has to be omitted to guarantee the geometric integrity of the welded component and to ensure sufficiently high contact pressures for

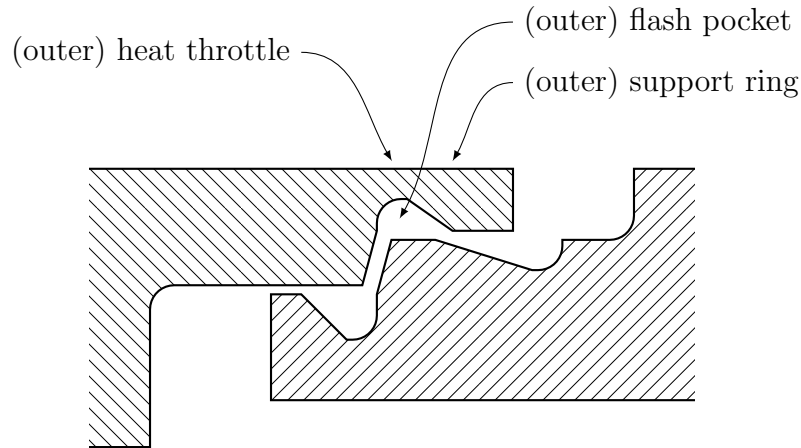


Figure 45: Twin function of the heat throttle as a flash pocket for a constant velocity joint application

bonding. Another design feature is the enclosure of the weld flash within the free space of the heat throttle, which is subsequently called *flash pocket*. The identification of the correct flash pocket dimensions has been done using the RFW process simulation. The flash pockets should not be too small, as otherwise the material flow can be disrupted. In consequence the cone formation might be impeded, which is associated with an unfavorable pressure distribution for bonding. Furthermore, the self cleaning effect can be diminished, increasing the risk of impurities in the WCZ. Too big flash pockets on the other hand weaken the structure without any need. The components shown in Figure 45 have an asymmetric design, in which the outer component is the thinner one. The outer component is made of 16MnCr5 case-hardening steel and the inner one of 25CrMo4 heat treatable steel, which slightly differ in their flow stresses. The experimental welding tests were carried out by the University of Applied Sciences Magdeburg-Stendal in preliminary works.

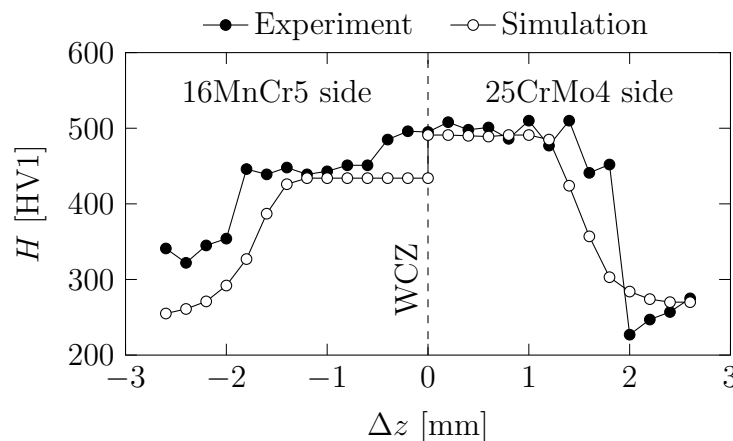
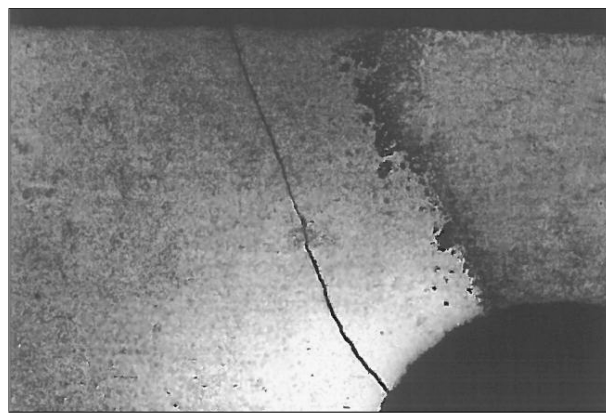


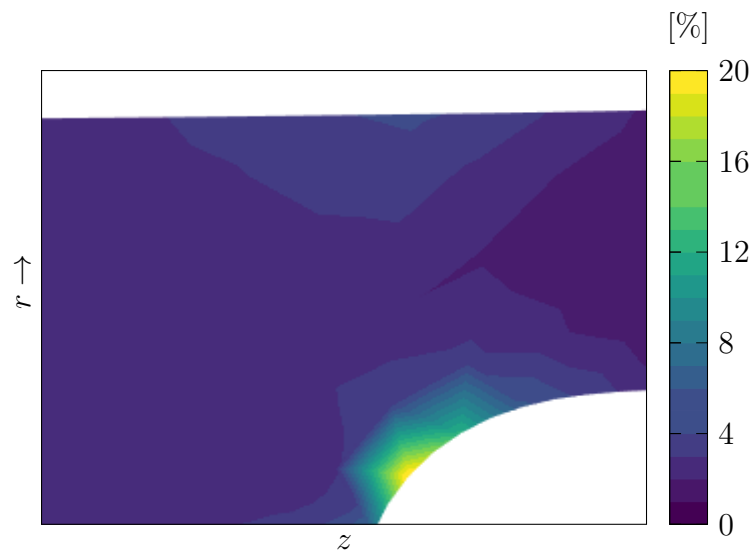
Figure 46: Hardnesses calculated using the RFW simulation and CCT diagrams and a comparison to experimental data perpendicular to the weld interface [134, 135]

## Experimental results

Overall, the flash pockets are working as intended in the experiments. Even though the inner support ring is touched by the weld flash, the material flow does not become stuck, as the weld flash forms in the shortening direction of the spindle. During the forging phase there is no significant axial shortening. Hardness measurements in the center, perpendicular to the WCZ are included in Figure 46, which are close to the maximum values found in the CCT diagrams [134, 135].<sup>23</sup> Unfortunately, there is a crack found in the macrograph of the outer heat throttle of the welded component, shown in Figure 47 (a).



(a) Macrograph of the outer heat throttle



(b) Plastic strain in the structural simulation

Figure 47: Macrograph showing the crack in the outer heat throttle at the location, where high plastic strains occur in the RFW structural simulation

<sup>23</sup>The measurement locations are also included in Figure 50.

## Simulation results

The location of the crack in Figure 47 (a) coincides with the spot of high plastic strains in the RFW structural simulation seen in Figure 47 (b). Even though cracking is not explicitly included in the RFW structural simulation model, the exceeding of the fracture strain of 16MnCr5 ( $A_\epsilon \geq 21\%$ ) is a valid indicator for it. Based on the simulation results, the crack shall grow from the inside to the outside of the heat throttle.

Figure 48 includes the fields of the state variables at the start of the RFW structural simulation, just moments after the spindle is stopped. By including elasticity and the thermal expansion based on the temperature distribution in Figure 48 (a), comparatively high axial stresses occur in the massive section and in the heat throttle of the outer component, which are plotted in Figure 48 (b). The inside of the outer component is dominated by tensile stresses and the outside by compressive stresses, resulting in the visible outward bending of the outer support ring. The bending instantly leads to plastic deformations in the outer heat throttle that are shown in Figure 48 (c), indicating that the crack initiation might already happen during the forging stage and not only after the RFW process. The total strains in the heat throttle increase further up until the end of the RFW structural simulation. For a comparison of the results of the RFW process simulation and the RFW structural simulation, the final total strains from both simulations are displayed in Figure 49. Overall, much higher strains occur in the outer component in the structural simulation. The crack shown in Figure 47 (a) is within the framed section in Figure 49 (a) and (b), in which the largest differences of both simulations are found. Due to the shrinkage during cooling, the outside diameters at the end of the process differ less in Figure 49 (b) than within the RFW process in Figure 48 (c). Besides the test of lower forging forces or the reinforcement of the heat throttle, the modification of the tooling might be considered to minimize the outward bending in Figure 48.

In addition to the hardness values in Figure 46, the estimated hardness distribution is shown in Figure 50 (b), which has been calculated based on the predicted temperatures. The local maximum temperature is shown in Figure 50 (a). Overall, the simulative hardness results match the experimental measurements very well. Due to the more filigree design, the maximum temperatures on the outside are higher than on the inside.

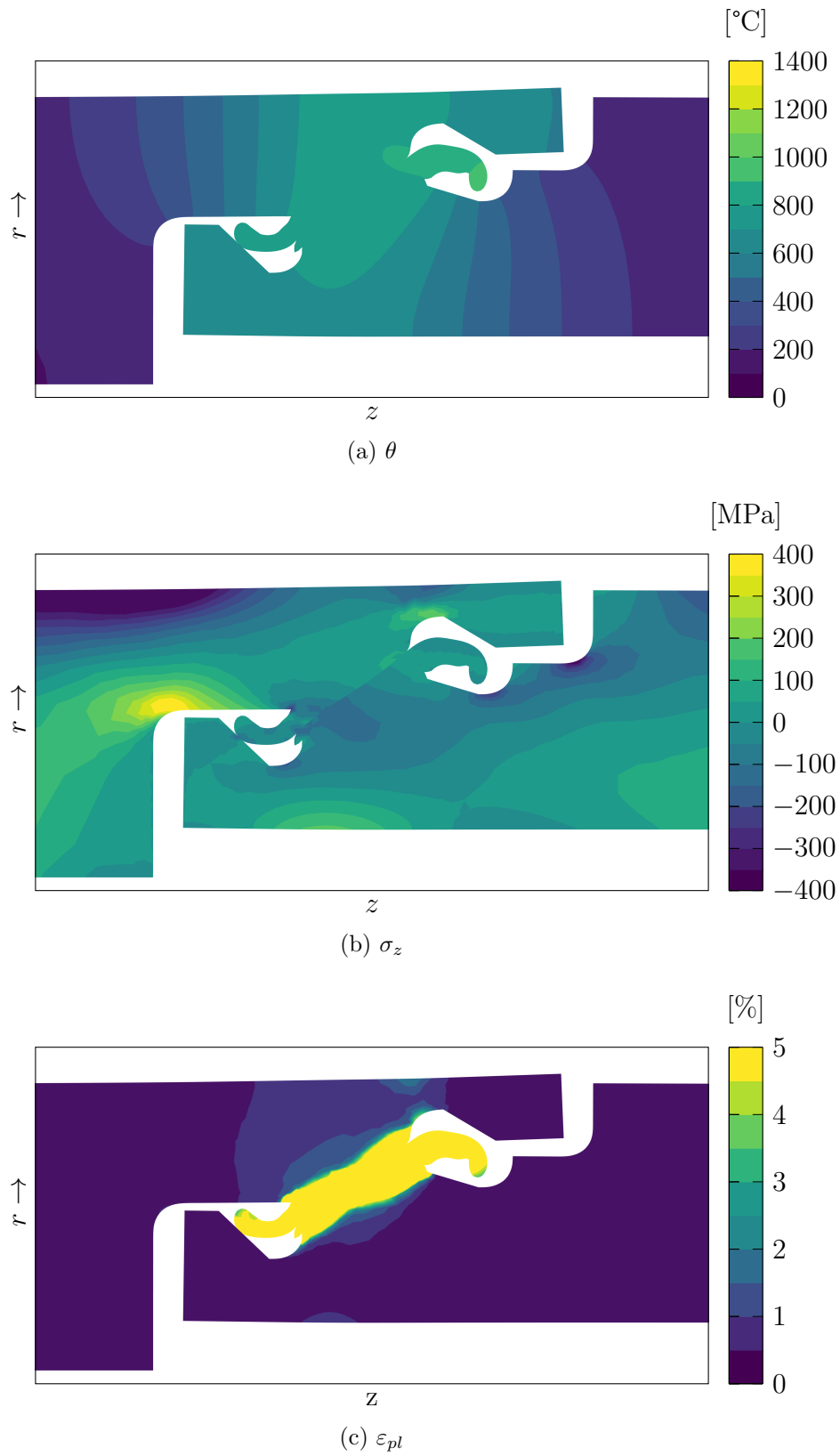
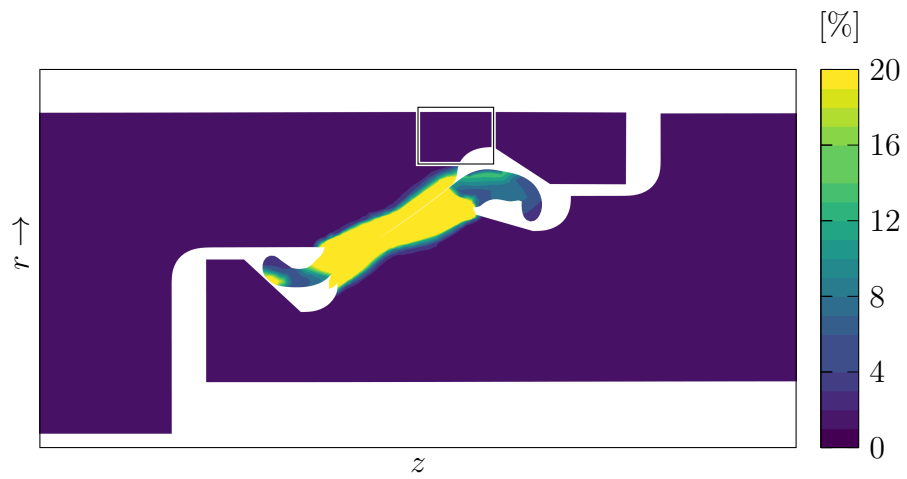
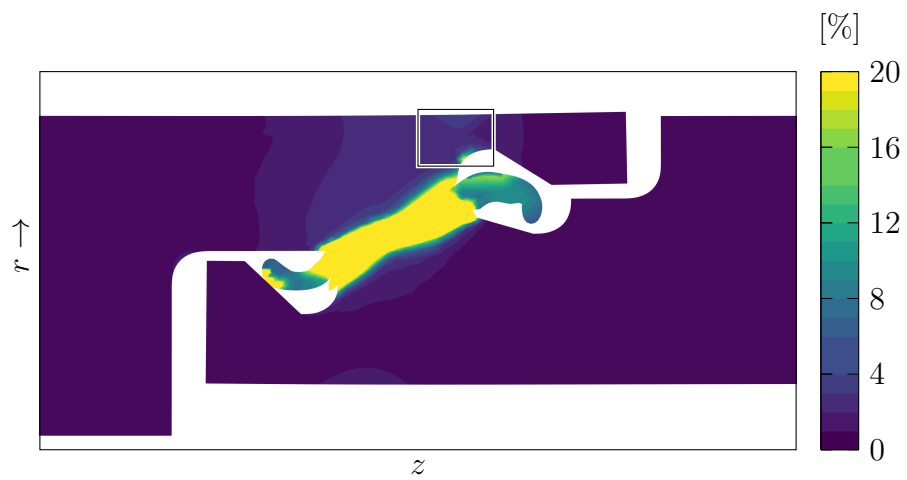


Figure 48: State variables in the forging phase right after the start of the RFW structural simulation



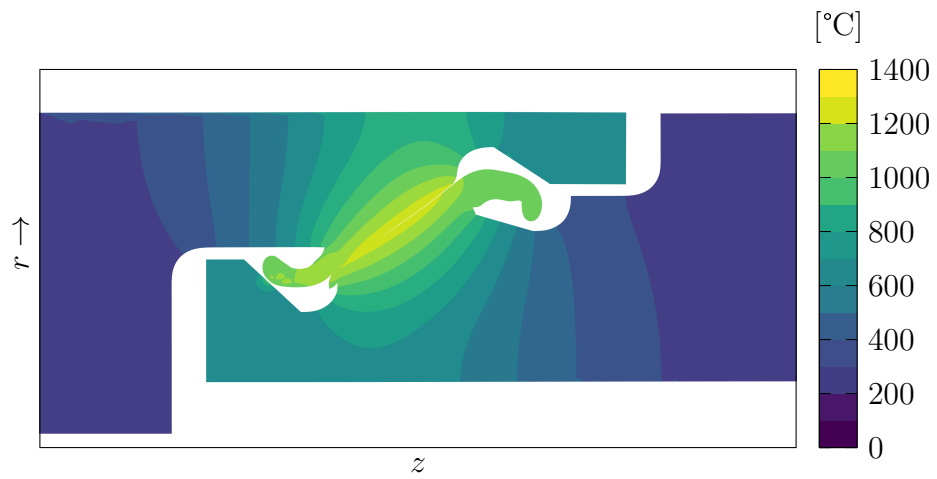
(a)  $\varepsilon_{pl}$ , process simulation



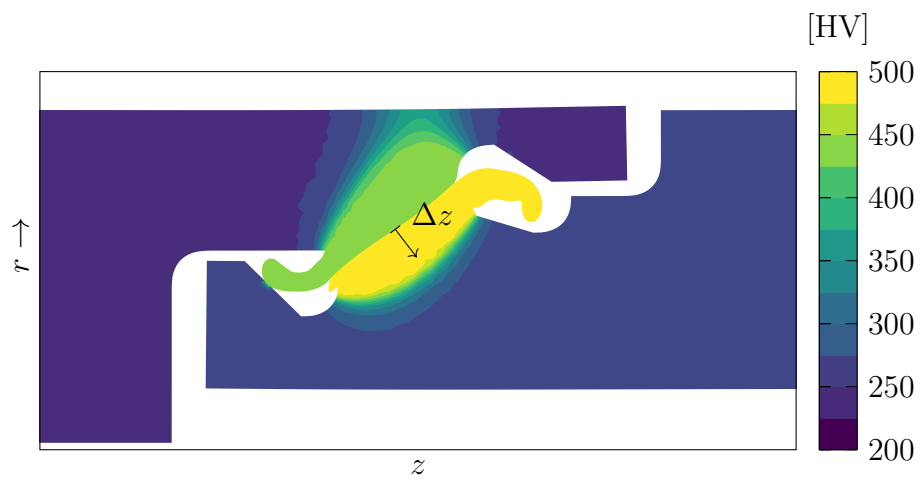
(b)  $\varepsilon_{pl}$ , structural simulation

Figure 49: Equivalent plastic strain at the end of the process simulation and the end of the structural simulation





(a) Simulated maximum temperatures



(b) Simulated hardnesses

Figure 50: Estimated distribution of the maximum temperatures and the resulting hardnesses in the constant velocity joint during RFW

## 5.2.2 Hybrid brake disc

Another concept with a heat throttle is a hybrid brake disc, in which two completely different components, a thin-walled hub and a massive rotor, have to be joined as in Figure 51. The combination is further complicated by the different material choices for the rotor and the hub. In contrast to existing solutions for hybrid brake discs, like in the patents EP 1 128 083 [136] and EP 2 249 055 [137] or in the concept by Füllgrabe [138], the concept here shall not rely on steel inserts casted into the rotor. To identify the RFW process parameters and the component designs, the RFW simulation has been used.

The hub is made of high-strength steel S420MC and the rotor is made of grey cast iron EN-GJL-150, the thermo-mechanical properties of which are listed in Table 7. Joining both materials using RFW is challenging in particular due to the high carbon content of the grey cast iron. Nonetheless, sound bonds have been achieved in primarily tests with this material combination, in which small steel samples have been welded onto cast iron segments. In the attempt to reproduce the local action in the WCZ for the brake disc components using the RFW process simulation, it has become clear that altering the RFW process parameters is not sufficient. The geometry of the disc has to be altered, too, and the heat throttle concept has been favoured over others. A macrograph of the weld is provided in Figure 52, in which it is seen that only on the hub side a flash is formed.

### Experimental results

A recurring phenomenon not observed in the preliminary tests has been an audible clicking sound, about two minutes after the RFW process ended. At this time, the welded component has still been held by the toolings.<sup>24</sup> The visual inspection of the components revealed that they cracked in the heat throttle. Photos of the cracks on the top and

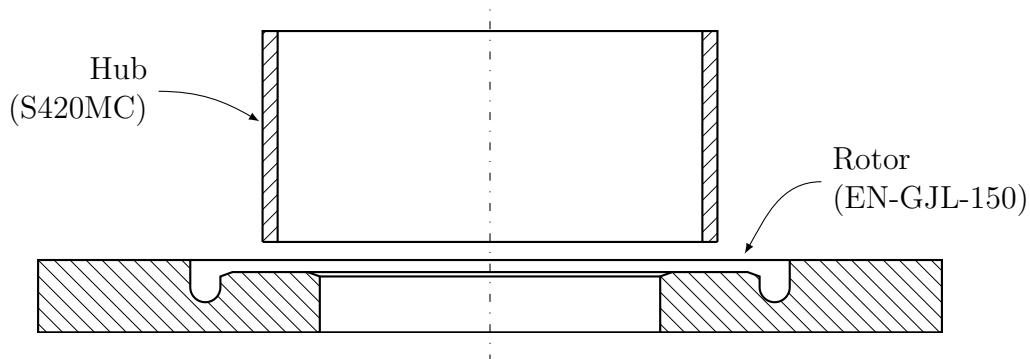


Figure 51: Concept drawing for a RFW brake disc combining a thin-walled hub and a massive rotor

<sup>24</sup>The welded component remains in the toolings for such a long time because torsional load tests are performed after welding directly in the RFW machine to check the bond quality.

Table 7: Material properties of grey cast iron EN-GJL-150 at room temperature according to EN 1561:2011 [139] and high-strength steel S420MC

Property		EN-GJL-150	S420MC
Elastic modulus	$E$	78 – 103 GPa	210 GPa
Poisson's ratio	$\nu$	0.26	0.30
Thermal expansion coefficient	$\alpha$	$13 \cdot 10^{-6}$ 1/K	$12 \cdot 10^{-6}$ 1/K
Flow stress at 20 °C	$\sigma_y$	98 – 165 MPa	$\geq 420$ MPa
Fracture strain	$A_\epsilon$	0.3 – 0.8 %	$\geq 16$ %

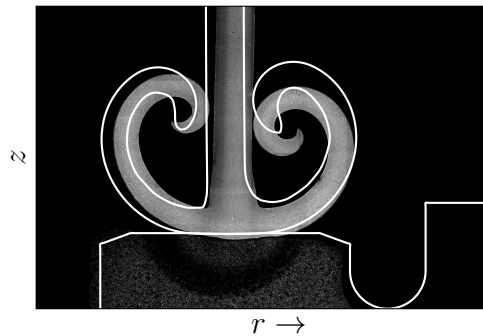


Figure 52: Macrograph of the RFW brake disc and the simulated flash contour extracted from the RFW simulation

the bottom side of the rotor are found in Figure 53. Due to the late occurrence of the clicking sound while cooling, it is plausible to assume that the cracks do not result from too high forging forces, but from the residual stress formation. Other welds of the testing series just crackled, without the distinct clicking sound. Figure 54 shows an image<sup>25</sup> of the periphery of the WCZ of a weld. In the right half of the image fine-grained cast iron material is found sticking to the steel weld flash. It has not been conclusively determined whether this is just extruded cast iron material or a crack running through the TMAZ of the cast iron material. The latter implies that a bond is initially formed in the periphery of the WCZ as well, which is then destroyed by residual stresses. In Figure 54, martensite is found near the lamellar graphite in the HAZ, favouring the formation of cracks. A calculated hardness field from the RFW simulation is displayed in Figure 55, in which the high hardnesses result from the martensite formation.

### Simulation results

Referring to Figure 52, the weld flash dimensions, the weld flash thickness and the weld flash curl are all well reproduced by the simulation. The slight radial offset in Figure 52 is due to the radial offset of the spindle and the stator tooling in the experiments. Figure 55 (a) shows the achieved maximum temperature distribution calculated using the RFW simulation, which helps to understand the cracking. By heating up in the WCZ,

<sup>25</sup>The image has been provided by Delta Sigma Analytics GmbH.

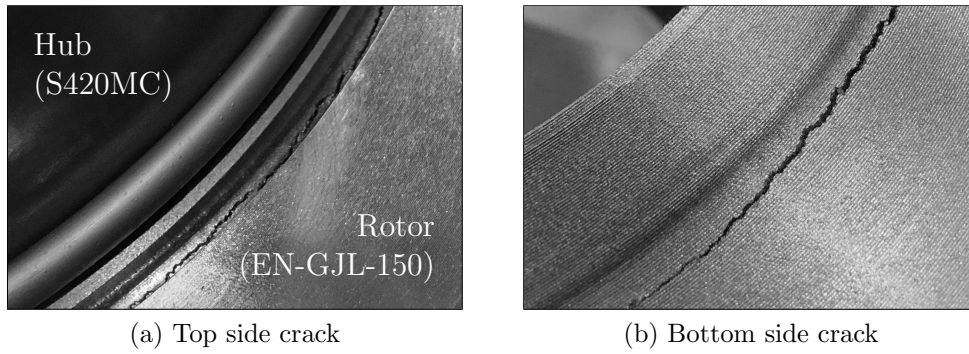


Figure 53: Cracks in the heat throttle of the brake disk rotor repeatedly found after RFW

the hub diameter expands outwards, so the hub becomes conical as a whole. The rotor on the other hand has to expand towards the inside, because the more outer section of the rotor avoids the expansion towards larger diameters. In this condition, the bond between both components forms. During cooling, the thermal expansions of both revert, so that the hub seeks to shrink inwards, while the rotor shrinks outwards. In the RFW structural simulation, it is found that this contraction of both components induces high radial stresses in the heat throttle, leading to the failure because the fracture strain  $A_\epsilon$  is excessively exceeded, as seen in Figure 56 (a). The WCZ is less prone to cracking due to the high strains, because the deformation takes place at much higher temperatures. But it can not be ruled out for now. The deformations in the bottom right corner occur due to the bending of the rotor in the tooling.<sup>26</sup> Figure 56 (b) only shows new deformations that occur 2 minutes after the end of the RFW process and later, highly localized in the heat throttle, where the cracks are found in Figure 53.

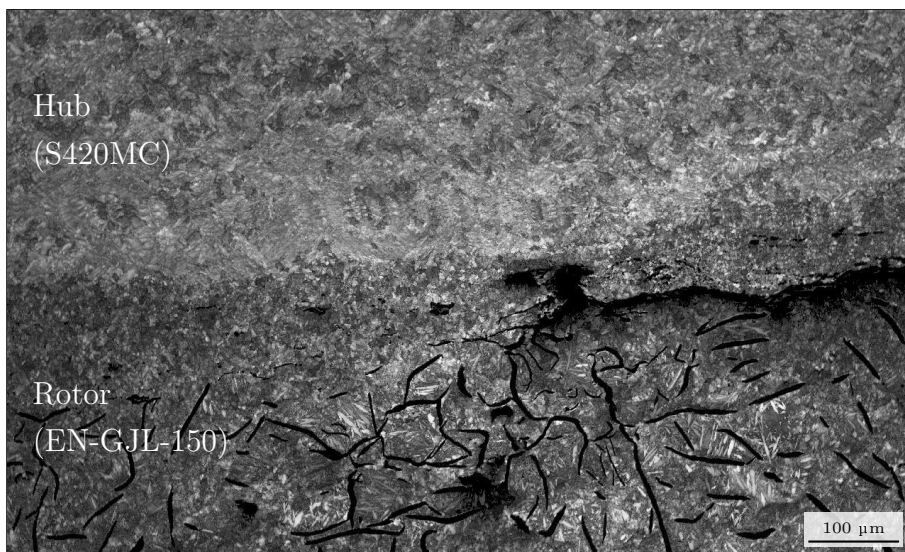
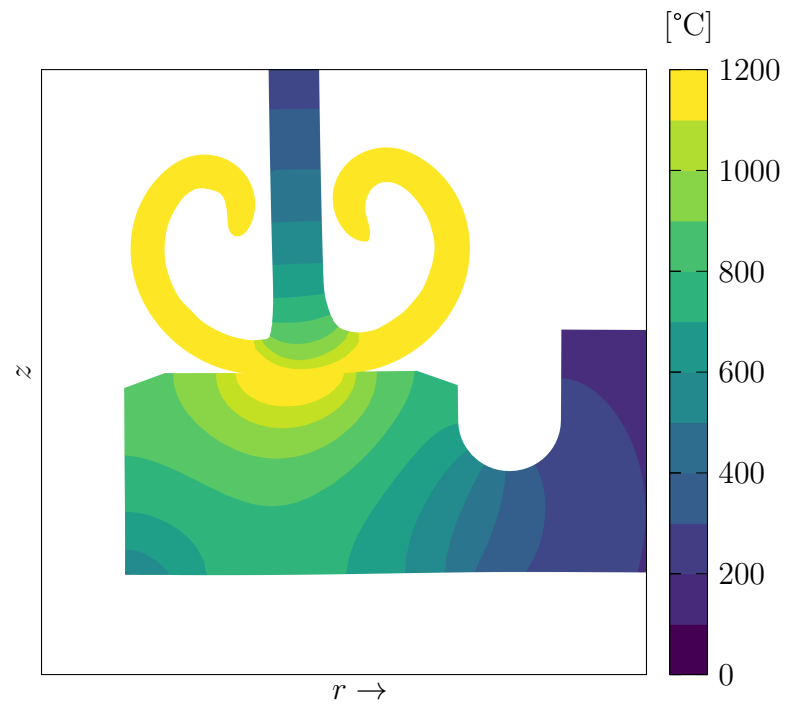
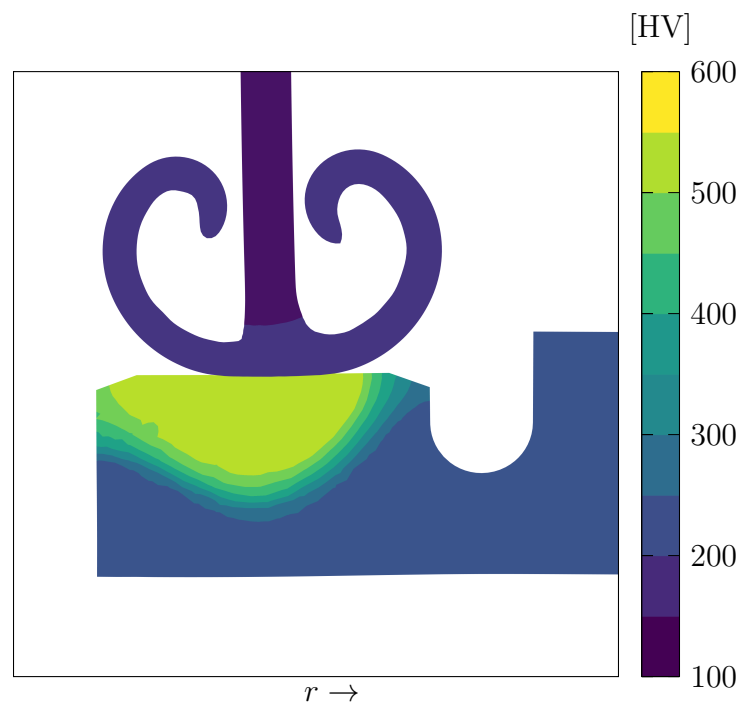


Figure 54: Image of the periphery of the WCZ showing fine-grained cast iron material sticking to the steel weld flash

<sup>26</sup>The toolings are included in the RFW simulations, but not depicted in the results.

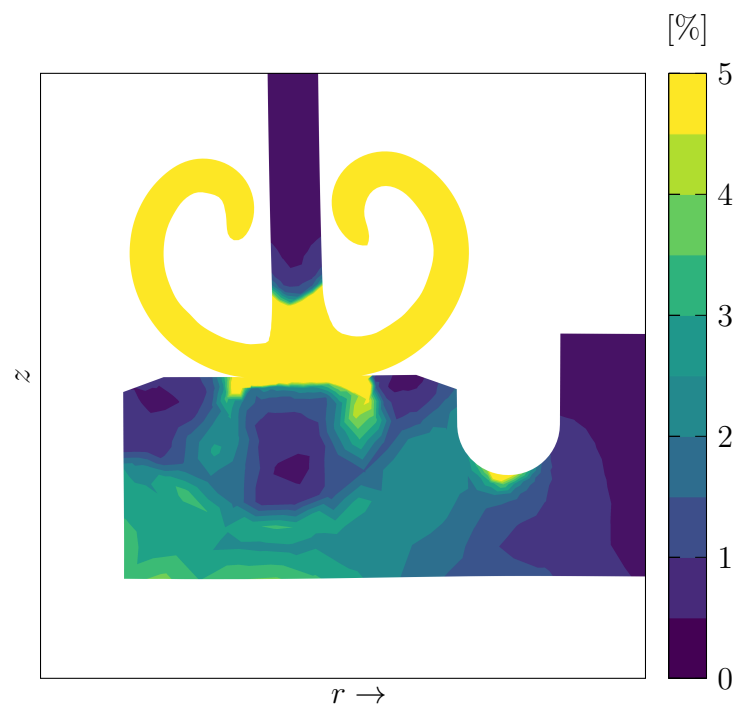


(a) Maximum temperature

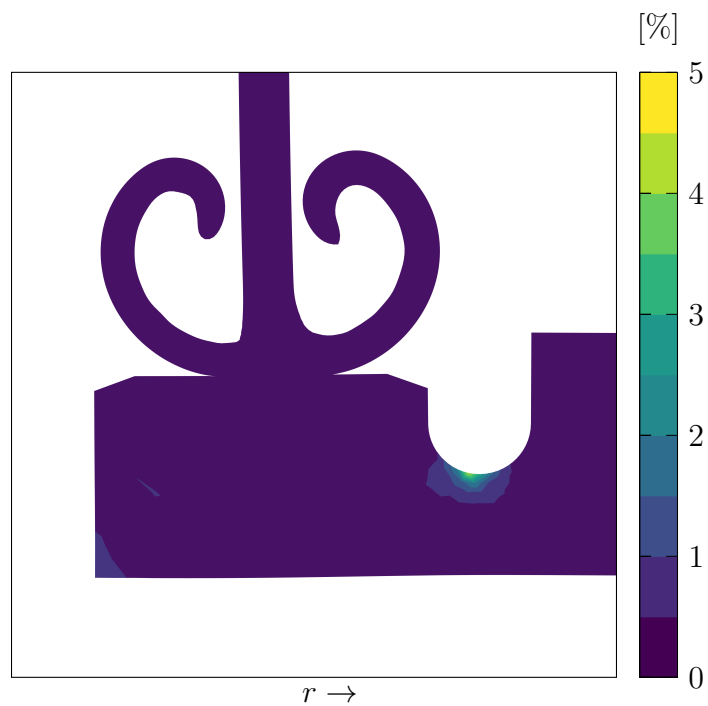


(b) Hardness

Figure 55: Maximum temperature distribution in the RFW brake disc and the hardness field identified using the RFW simulation



(a) Total process



(b) New occurring later than 120 s

Figure 56: Equivalent plastic strain  $\varepsilon_{pl,v}$  excessively exceeding the fracture strain of EN-GJL-150 ( $0.3 \leq A_\varepsilon \leq 0.8$  %) in the heat throttle of the rotor during cooling down after RFW

## 5.3 Hybrid welds

To follow the lightweight construction principle of using the right material in the right spot, very different materials can be joined by RFW. The combination of aluminum and ferrous alloys is among the most popular for structural components. BMW for example produced an aluminum alloy cardan shaft with a steel flange in series [140].

Aluminum alloys and steels are considered challenging to weld, though. One reason is the formation of intermetallic compounds (IMC) in the WCZ. While the IMC formation is necessary to achieve a bond between both materials, due to their brittleness, thin IMC layers are desirable [4, 141, 142]. Secondly, the thermal diffusivities  $a$  and the thermal expansion coefficients  $\alpha$  of aluminum alloys and steel are rather dissimilar. The difference of  $a$  mainly affects the heat distribution within the RFW process, whereas the difference in  $\alpha$  causes distortions and residual stresses during cooling. In theory, the WCZ side with the higher  $\alpha$  shall have tensile residual stresses and the side having the lower  $\alpha$  compressive ones. Because of the comparatively low temperatures in the RFW simulation, the transformation hardening of the steel does not have to be considered in the following.

### 5.3.1 Welding of Al-Fe alloy rods

Gan et al. [47] performed residual stress measurements in rods, whose experiments are reproduced with the RFW simulation in the following. Rods of 24 mm diameter made of a 7000 series aluminum alloy and austenitic stainless steel (AA7020-T6 and 316L) have been joined using RFW. The process parameters are as stated as in Table 8. Compared to structural steels, austenitic steels have higher thermal capacities and conductivities as well as higher linear thermal expansion coefficients. The elastic material properties used in the simulation are listed in Table 9 [114, 115]. Before welding, the steel rods have been pre-heated up to 500 °C.<sup>27</sup>

Table 8: RFW process parameters used by Gan et al. [47]

$p_1$ [MPa]	$p_2$ [MPa]	$s_3$ [mm]	$s_f$ [mm]	$n_0$ [min <sup>-1</sup> ]
190	320	3.2	11.5	1476

<sup>27</sup>Contrary, Tasdemir [143] pre-heats a drilled aluminum plate to 200 °C to make use of the shrinkage to hold a steel insert by a press-fit in case there is no bond established.

Table 9: Material properties used for the simulation for the 7000 series aluminum alloy and the austenitic steel [114, 115]

Aluminum alloy			Austenitic steel	
$\theta$ [°C]	$\alpha$ [10 <sup>-6</sup> /K]	$E$ [GPa]	$\alpha$ [10 <sup>-6</sup> /K]	$E$ [GPa]
20	22.4	70.0	16.5	190.0
100	23.1	67.9	16.7	182.4
200	24.0	60.2	17.3	174.8
300	24.9	47.6	17.0	167.2
400	25.8	28.0	17.0	159.6
500	26.7	9.3	17.9	152.0

### Experimental results

The measurement results by Gan et al. [47] using neutron diffraction are depicted in Figure 57. It should be noted that the measurement fields do not include the radial outer boundary areas. As expected, tensile residual stresses are present in the Al alloy side and compressive residual stresses in the austenitic steel. Examining the three residual stress fields, it is striking that particularly high stresses are found in two spots in the RFW-affected zone of the aluminum alloy, at  $r = 0$  and  $r = 6$  mm, in all directions. In contrast to  $\sigma_r$  and  $\sigma_\varphi$ , the axial residual stress maximum on the steel side is more distanced to the WCZ.

### Simulation results

Overall, the tensile residual stress measurements in the aluminum rod are well reproduced in the RFW structural simulation, although the two high stressed spots at  $r = 0$  and  $r = 6$  mm do not occur. The compressive stresses in the steel rod are also identified in the simulation. The axial residual stress peak is shifted backward from the weld interface compared to the radial and circumferential stresses as in the experimental results, but overall the residual stresses are comparatively low. The radial and axial gradients are slightly steeper than in the measurement and the stresses in the steel higher, which shall be accounted for by the uncertainties of the boundary conditions in the simulation. In the simulation, the whole steel part is heated up to homogenous 500 °C and the process instantly starts, which likely differs in the test setup due to the heat losses through the toolings.



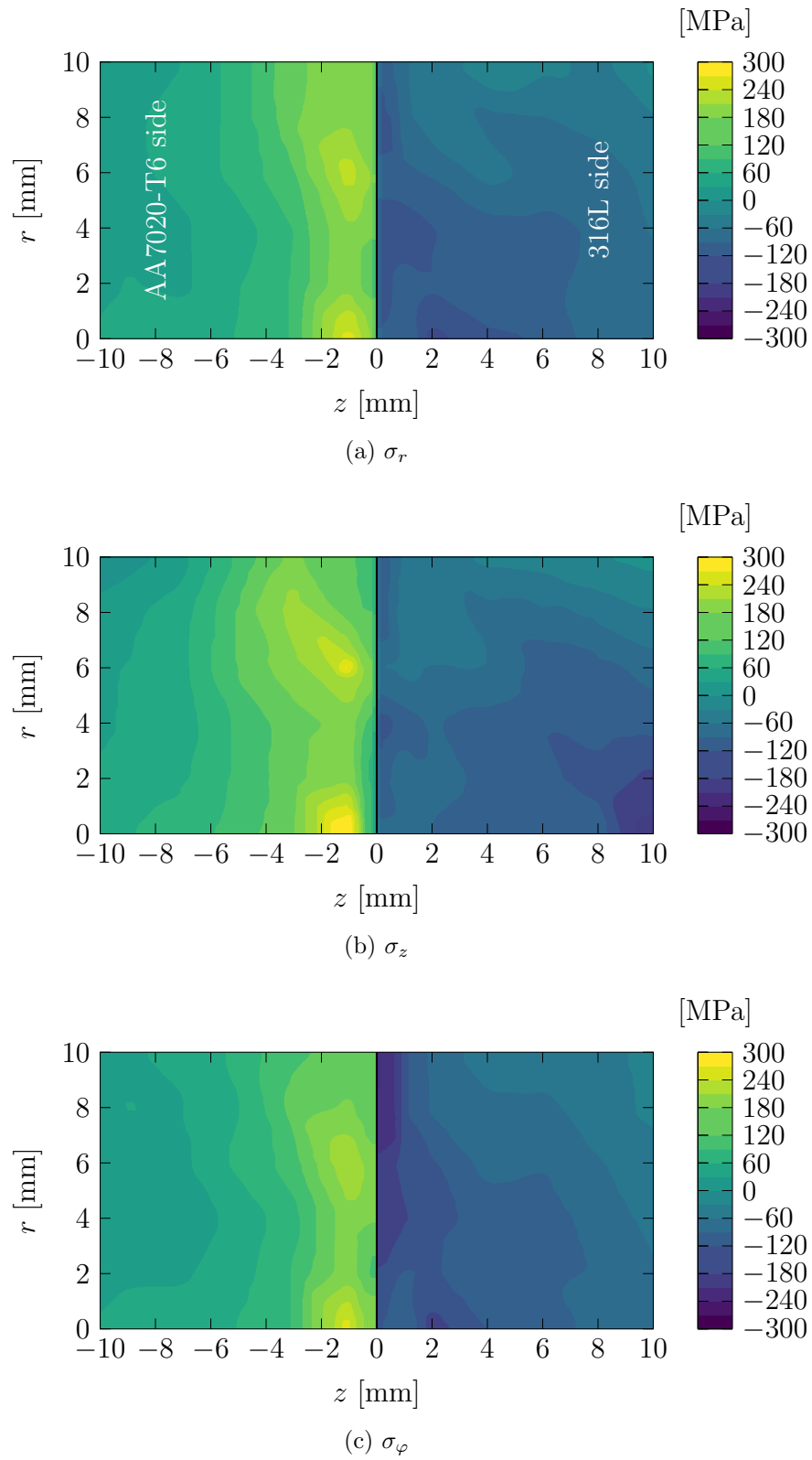


Figure 57: Residual stress measurements in mixed aluminum steel welds in aluminum alloy (left) and steel (right side) by Gan et al. [47]

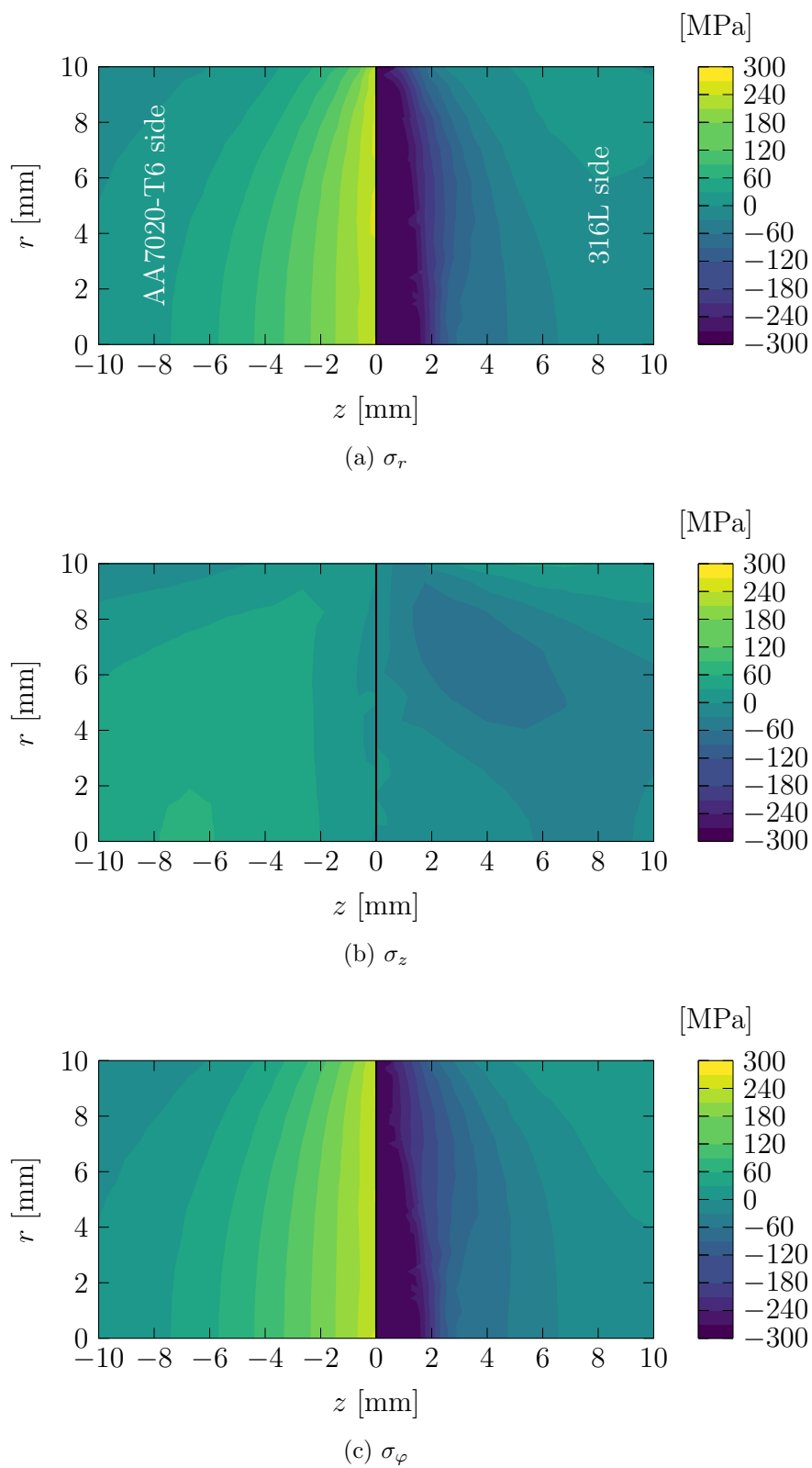


Figure 58: Residual stress calculations in mixed aluminum steel welds in aluminum alloy (left) and steel (right side) using the RFW simulation

### 5.3.2 Lightweight gear wheel

A lightweight gear wheel such as shown in Figure 59 is intended to be used in the power trains of vehicles with electric and internal combustion engines. In order to transmit the required torques, the teeth have to be made of hardened steel, while a softer aluminum alloy core offers superior heat transfer properties and potential weight savings. A conceptual drawing of the components is shown in Figure 60. A large WCZ, in which the local action identified as optimal for the Al-Fe alloy combination is replicated, is achieved by the conical shape of the steel component. A matching conical shape is formed from the two shoulders of the aluminum component in the RFW process. Because the WCZ is also running in  $z$ -direction in this application, axial stresses are induced on top. Therefore, the advantage of the large WCZ in this design is accompanied by the disadvantage that, in theory, higher residual stresses are to be expected.

#### Experimental results

Although the ideal local action is reproduced in the WCZ, the macrograph in Figure 61 reveals that the aluminum alloy core is detached from the hardened steel ring. Other segments across the WCZ have to be bonded, however, because the core is not falling out of the ring. It is assumed that all segments have been bonded, but some debonded due to the residual stress formation. An observation supporting this is that the welded gear wheels emits crackling sounds for long periods, which was not observed in preliminary experiments with this material combination.

#### Simulation results

Figure 62 provides the temperature distribution in the forging stage, when the maximum forging force is reached, determined with the RFW process simulation. The plot in Figure 63 (a) shows that the residual equivalent stresses in the aluminum alloy core after cooling down to room temperature are at the level of the yield stress of the aluminum alloy, explaining the crackling sound emitted by the on-going deformation and the resulting debonding. As seen in the tangential residual stress field in Figure 63 (d), the aluminum alloy core intends to shrink more inwards than the steel ring allows to during cooling. This is aggravated by the fact that the aluminum alloy conducts heat quickly from the weld interface into the rest of the core, which increases the total thermal expansion of the core. The hardened steel ring is covered by compressive residual stresses, as two thirds of the ring are pulled inwards by the bonded aluminum alloy core. In the axial stress field in Figure 63 (c), the effect of the incompatibility of the thermal expansion coefficients that causes the radial and tangential residual stresses in Section 5.3.1 can be observed. The radial residual stresses in turn are similar to the axial ones in Section 5.3.1.



Figure 59: Lightweight gear wheel combining a toothed ring of hardened steel and a softer aluminum alloy core

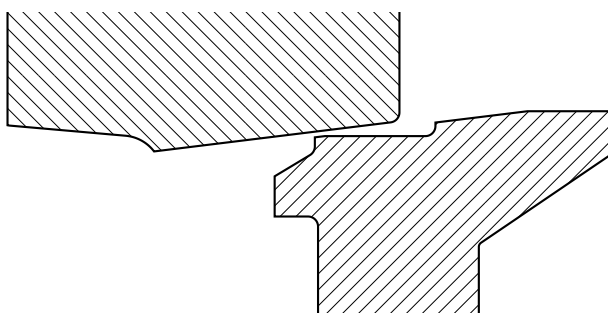


Figure 60: Conical RFW design concept for the lightweight gear wheel, in which the aluminum alloy core is allowed to deform to adapt the conical shape of the steel ring

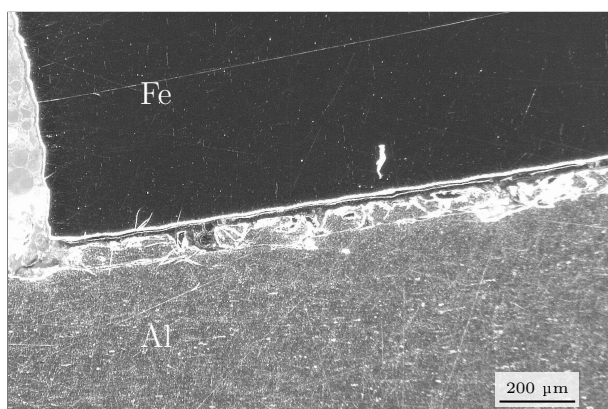


Figure 61: Macrograph of the WCZ of the lightweight gear wheel showing the separation on the inside

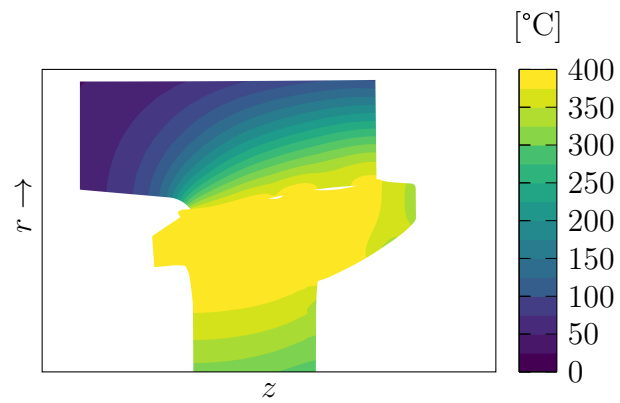


Figure 62: Temperature distribution in the forging stage after the spindle stop

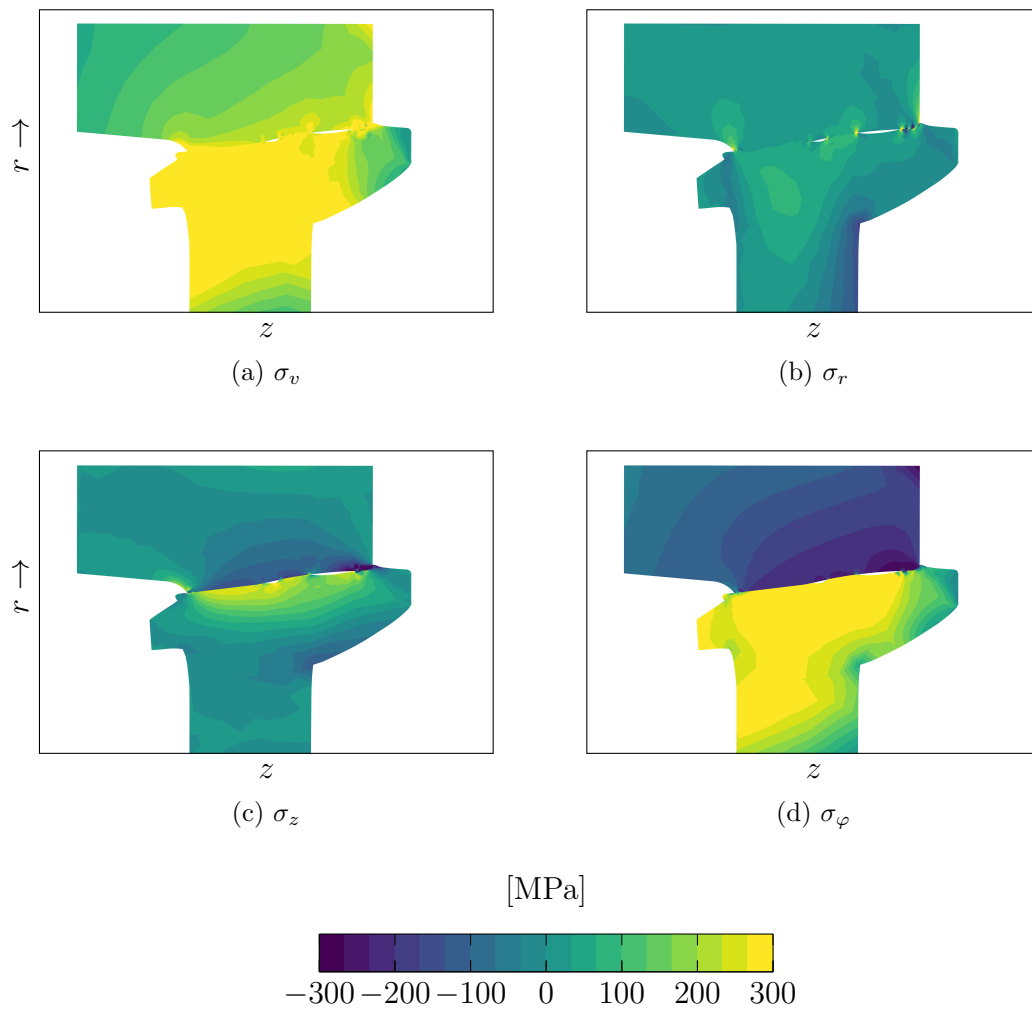


Figure 63: Distributions of the individual residual stress components in the lightweight gear wheel after RFW

## 5.4 Inertia friction welding of large rings

The ring elements depicted in Figure 64 have been investigated by Grant et al. [42] in detail, which have to be considered the most comprehensive studies that deal directly with residual stress measurements in RFW welds, and are intended to serve as a benchmark for simulation here. The following is a summary of the RFW process and the findings related to the residual stresses. The outer diameter of the rings is 143 mm and their wall thickness is 10 mm. The industrial application hidden behind these rings is a high pressure compressor drum being part of jet engines by Rolls-Royce plc [36]. Compared to the results published by Rößler et al. [83, 144] earlier, an improvement of the results is achieved by pushing the start of the simulation more forwards, including the tooling in the simulation and using a more refined mesh.

The rings are made of the nickel-based superalloy RR1000. Most of its material information has been published. Wang et al. [13] and Grant et al. [42] provide the temperature-dependent mechanical material parameters  $\sigma(\theta)$ ,  $n(\theta)$  and  $E(\theta \leq 800 \text{ }^\circ\text{C})$ , which tend to be most relevant for the RFW simulation. For higher temperatures,  $E(\theta > 800 \text{ }^\circ\text{C})$  is assumed to be identical to the elastic modulus of similar Inconel alloy 718, whose thermal material parameters are used, too [145, 146]. The hardening of RR1000 is based on the precipitation of  $\gamma'$  and  $\gamma''$  phases, which is why the hardening model presented in Section 2.3.2 is not applicable.

An IFW process is used, whose exact parameters are not published by Grant et al. [42] due to confidentiality. The available weld flashes and process times, however, allow to reverse engineer the RFW process and indicate a potential set of process parameters. The initial flywheel energy is expected to be 1.2 MJ and the welding pressure 250 MPa. Based on the outer diameter, the flywheel inertia is accelerated up to an initial rotational speed of  $500 \text{ min}^{-1}$ . The residual stress mappings determined using the neutron diffraction method are compared with the results of the simulation in Figure 66, in which  $\Delta z$  denotes the axial distance from the weld interface. Overall, the residual stress levels are well estimated by the simulation for this specific example. The quantitative validation of the model is difficult in the sense that the RFW process parameters in use are estimations.

For the interpretation of the residual stress fields, it is more convenient to zoom out as in Figure 67 and evaluate the whole part.<sup>28</sup> By this, it becomes evident that the tensile residual stresses in the upper right corner in Figure 67 (b) result from the notch effect of the weld, which is machined off prior to the measurements. Referring to the residual stress causes, presented in Section 2.2, Figure 65 shows the temperature distribution

<sup>28</sup>Although both rings are shown, the symmetry of the components is utilized to shorten the simulation times. The necessary boundary conditions are applied to the weld interface.

at the moment the spindle stops. At this time, the material model is swapped, then including elasticity and thermal expansion. Due to the inhomogeneous temperature field, the rings expand in the weld area more than in other areas. The rings become conical and their bond is established. For the fulfillment of symmetry, the bond has to be perpendicular to the rotational axis, forcing more material to be extruded on the inside than on the outside of the rings. In the subsequent cooling, the thermal expansion reverts, but because of the material extrusion difference the component shape remains slightly conical. In consequence, the stresses of highest magnitudes are found in the tangential direction, whereby the RFW-affected zone is under tension. To keep the stresses in self-balance, the other areas are under compressive residual stresses. The second highest residual stresses are the axial stresses. Resulting from the bond restricting the inward shrinkage, the residual stresses are compressive on the outside and tensile on the inside. The smallest stresses in terms of the magnitude are the radial residual stresses.

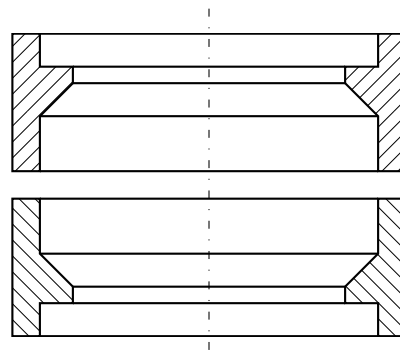


Figure 64: Ring element geometry used by Grant et al. [42] as a substitute for the compressor drums by Rolls-Royce plc

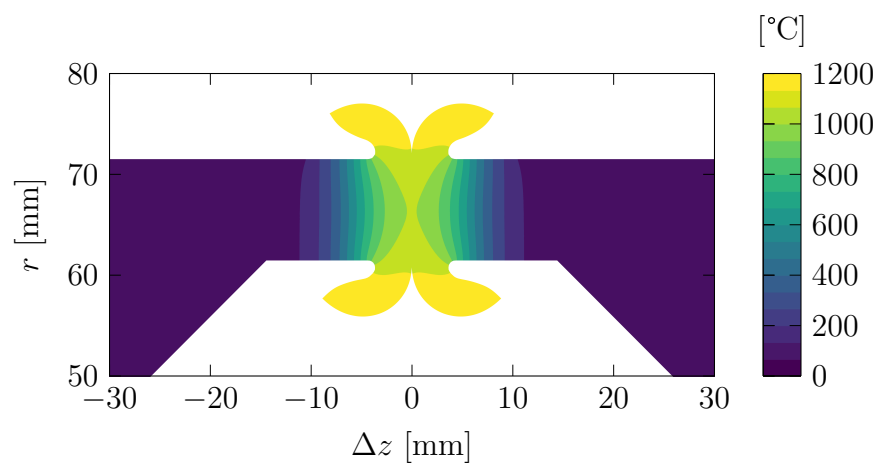


Figure 65: Simulative determined temperature field in the ring element at the beginning of the RFW structural simulation

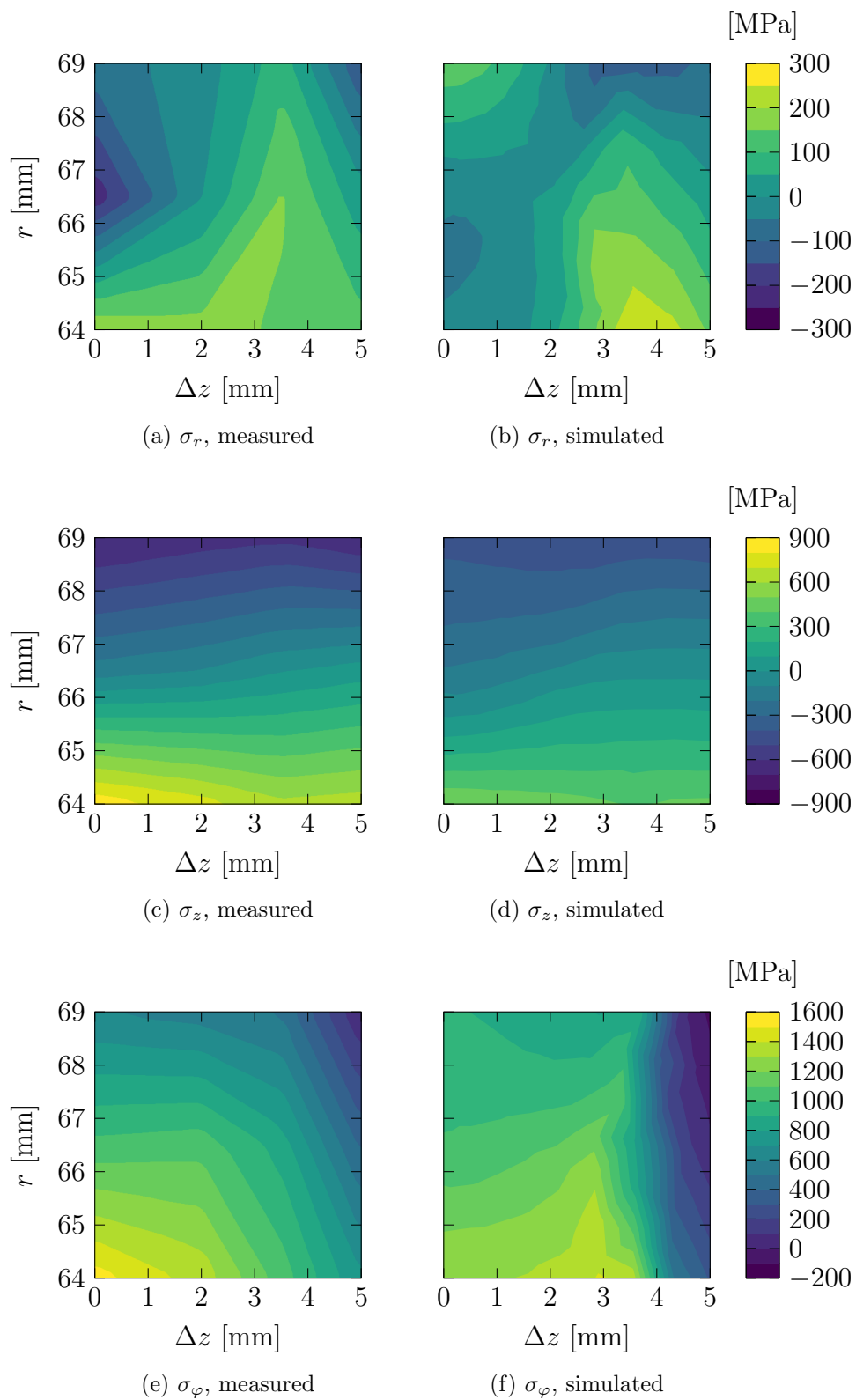


Figure 66: Residual stress measurements by Grant et al. [42] and the estimated stress fields by the simulation



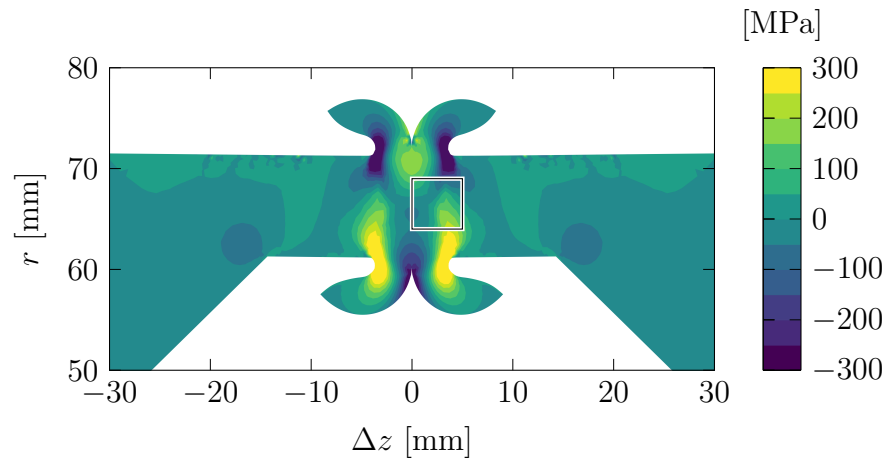
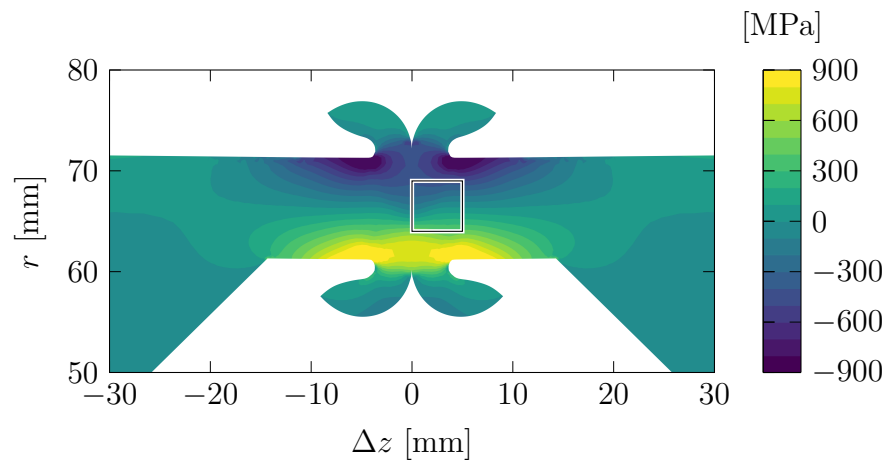
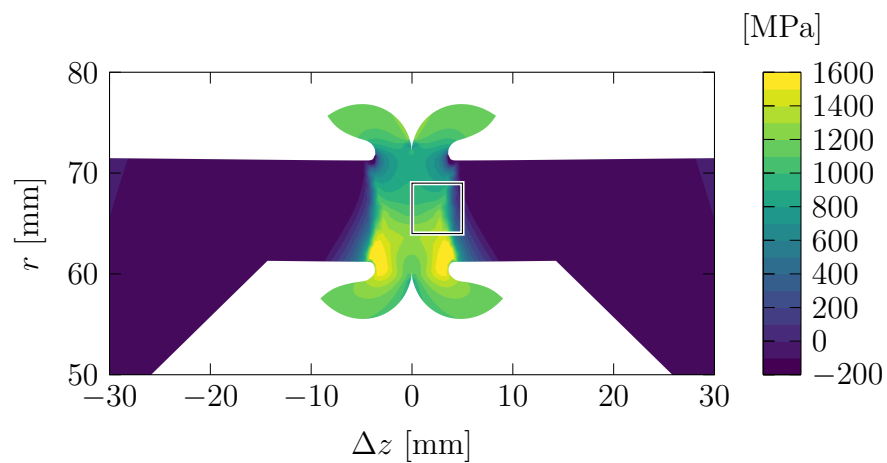
(a)  $\sigma_r$ , simulated(b)  $\sigma_z$ , simulated(c)  $\sigma_\varphi$ , simulated

Figure 67: Residual stress fields in the welded ring elements zoomed out the measurement fields (box) in Figure 66



## 6 Conclusion

A structural simulation model has been set up for a better understanding of RFW. The focus has been on the effects observed right after the actual process, during cooling, which can not be simulated by the RFW process simulation by Schmicker [1].

### 6.1 Added value to the RFW simulation

The RFW simulation reliably reproduces various RFW examples and helps to analyze the residual stress formation in RFW, which has not been possible to this extend so far. One of the most compelling features of the presented model extensions is that once the RFW process simulation model is set up for an application, the additional effort to perform the RFW structural simulation is as low as possible. This has been successfully achieved by only adding a few parameters – for thermal expansion and for elasticity and optionally for phase transformations for steels. The former parameters are typically provided as tabulated data. The phase transformation model can be fully parameterized using data from TTA and CCT diagrams without additional experiments. Besides residual stresses, hardness fields can be estimated, too. The bonding model assumes a permanent bond, if the plastic strains are above a threshold value, which is a simple yet conservative criterion in regards to the residual stress formation. Based on the results, it seems necessary to include the bonding model in the RFW process simulation. For one example the initial hypothesis that the cracks outside of the WCZ are related to residual stresses is disproved. The RFW structural simulation shows that the cracks already occur within the RFW process, because of too high process forces.

Model limitations are in part a result of the material model being mainly tailored for steels. In other applications, microstructural effects have to be neglected for now. It has also not been tested, how well the used phase transformation model for steels is suited for processes, in which the cooling paths deviate significantly from the Newtonian cooling curve – for instance if PWHT is performed within the RFW machine. Other topics not discussed in this work are the effects of non-axisymmetric geometries and initial stresses, which are important in case of RFW components failing outside of the WCZ.

## 6.2 Guidelines for residual stress compliance

Based on the presented simulation results, some general takeaways for designing RFW processes are listed in the following.

1. To counteract shrinkage in the cooling process, the friction time shall be kept low. This is not feasible for all materials (and material combinations) without reducing the quality of the weld, because the bonding mechanism depends on the superposition of high pressures, high plastic strains and high temperatures.
2. For certain material combinations, high residual stresses seem inevitable, since both materials shrink differently during cooling, after the welding process, which is related to the thermal expansion coefficients. Analytically, in mixed weld solid shafts, tensile residual stresses are expected on the material side with the larger coefficient of expansion. The limiting factor for combinations such as aluminum and steel seems to be the yield stress.
3. Wherever possible, the geometries shall be designed to force the thermal expansion of the components to be in the same direction.
4. Machining off of the weld flash while the parts are hot is advised, since the weld flash might act as a notch. This is especially problematic, if the region is under tensile residual stresses.
5. Design elements like the heat throttle provide a solution to minimize the heat losses in the RFW process. Attention must be paid to the proper dimensioning. Even if the heat throttle is not directly in the flux of force, it can be highly stressed within the RFW process as well as during cooling due to the inhomogenous temperature fields in the components.

## 6.3 Outlook

The RFW structural simulation significantly extends the possibilities of using the RFW simulation as a development tool already. Three development directions are considered particularly important for the near future.

The most urgent need is the development of a bonding strength estimator for RFW, which is versatile enough for the very different material combinations in RFW. It seems promising to implement an energy-based criterion, as the necessary local action variables are available and the evaluation of the self-cleaning in the RFW process is already well estimated by tracking the material point movements. Besides the quantitative strength, the moment of bonding seems equally important for the residual stress formation. The

debonding due to excessive residual stresses might also be discussed at the same time. As stated earlier, the worst case of a permanent bond is used in the current RFW structural simulation model, respectively a frictional contact in the RFW process simulation model.

Secondly, dealing with three dimensional geometries seems inevitable in certain applications. The examples presented are all axisymmetric, but there are various other applications, in which this is not the case, or, in which the part is only partially supported by the toolings. Another aspect is the extension of the material model for lightweight alloys, such as aluminum alloys. As the hardening mechanism in this work is based on the phase transformation of steels, effects like grain size changes, recrystallization and precipitation have not been directly implemented yet. The coupling of the RFW microstructural simulation model and the RFW process simulation model also seems feasible, to account for latent heat effects and the change of the thermal material properties within RFW. Concerning the model application, options such as preheating in the machine or the preloading of components by the tooling to counteract the residual stress formation should be argued.



# Nomenclature

$A$	$\text{mm}^2$	Area size
$A_0$	$\text{mm}^2$	Initial area size
$A_\varepsilon$	–	Fracture strain
$Ac_1$	$^\circ\text{C}$	Lower transformation temperature while heated
$Ac_3$	$^\circ\text{C}$	Upper transformation temperature while heated
$C$	%	Carbon content
$E$	MPa	Elastic modulus
$E_\phi$	MPa	Elastic modulus of the transformed phase
$E_\psi$	MPa	Elastic modulus of the untransformed phase
$E_0$	MPa	Elastic modulus at room temperature
$F$	N	Axial force
$F_1$	N	Friction force
$F_2$	N	Forging force
$F_n$	N	Normal force
$F_r$	N	Radial force
$H$	HV	Vickers hardness
$H_0$	HV	Reference hardness
$H'_0$	HV	Modified hardness
$H_i$	HV	Hardness of phase $i$
$J$	$\text{tmm}^2$	Flywheel inertia
$K_H$	–	Thermal history hardening factor
$K_i$	–	Hardening term $i$
$N_i$	–	Shape function
$O$	mm	Radial overlap
$Q$	$\text{tmm}^2/\text{s}^2$	Frictional heat
$Q_g$	$\text{tmm}^2/\text{s}^2$	Activation energy
$R$	$\text{JK}^{-1}\text{mol}^{-1}$	Gas constant
$R^2$	–	Coefficient of determination
$T$	Nm	Frictional torque

---

$U$	$\text{tmm}^2/\text{s}^2$	Internal work
$U_{\min}$	s	Threshold energy input
$V$	$\text{mm}^3$	Volume
$W$	$\text{tmm}^2/\text{s}^2$	External work
$Z$	–	Objective function
$a$	$\text{mms}^2$	Thermal diffusivity
$a_H$	MPa/HV	Plastic hardness slope
$b_H$	MPa	Plastic hardness offset
$c$	–	Chemical composition
$d$	mm	Diameter
$d_0$	mm	Initial diameter
$d_L$	$\mu\text{m}$	Lattice spacing
$f_i$	–	Temperature rate dependent function of phase $i$
$g$	$\mu\text{m}$	Grain size
$k$	MPa	Yield stress in pure shear
$k$	–	Transformation parameter in the JMAK equation
$k_\alpha$	s/K	Diffusive transformation peak factor
$k_i$	s/K	Transformation peak factor phase $i$
$i$	–	Index variable
$j$	–	Index variable
$m$	–	Transformation parameter
$m_i$	–	Hot deformation constant $i$
$n$	–	Strain rate sensitivity exponent
$n$	–	Transformation parameter in the JMAK equation
$n$	–	Transformation parameter in the Kirkaldy's equation
$n'$	–	Hardened strain rate sensitivity exponent
$n$	$\text{min}^{-1}$	Rotational speed
$n_0$	$\text{min}^{-1}$	Initial rotational speed
$n_2$	$\text{min}^{-1}$	Rotational speed to trigger the forging stage
$n_r$	–	Radial component of the normal vector
$n_z$	–	Axial component of the normal vector forging stage
$p$	MPa	Hydrostatic pressure
$q$	–	Time integration exponent parameter
$r$	mm	Radial position
$s$	mm	Axial feed
$\dot{s}$	mm	Axial feed rate
$s_0$	mm	Initial axial feed
$s_3$	mm	Axial friction feed
$s_F$	mm	Final axial feed



---

$t$	s	Time
$t_1$	s	Beginning of the friction stage
$t_2$	s	Beginning of the forging stage
$t_3$	s	Beginning of the spindle braking
$t_4$	s	End of the forging stage
$t_i$	s	CCT transformation time
$t'_i$	s	Modified CCT transformation time
$\Delta t$	s	Time step
$\Delta t_{8/5}$	s	Cooling time from 800 to 500 °C
$u$	mm	Displacement
$w_j$	–	Weighting parameter at time $j$
$z$	mm	Axial position
$\Delta z$	mm	Axial offset
$\alpha$	1/K	Thermal expansion factor
$\alpha_i$	1/K	Thermal expansion factor of phase $i$
$\beta$	1/K	Exponent in the Koistinen-Marburger equation
$\gamma$	–	Austenite content
$\delta_i$	–	Transformation plasticity coefficient of phase $i$
$\delta_{RFW}$	–	CCT time corrector
$\epsilon$	mm	Time integration error parameter
$\varepsilon$	–	Strain
$\dot{\varepsilon}$	s <sup>-1</sup>	Strain rate
$\dot{\varepsilon}_0$	s <sup>-1</sup>	Reference flow strain rate
$\dot{\varepsilon}_C$	s <sup>-1</sup>	Characteristic flow strain rate
$\varepsilon_c$	–	Total strain of the transformed phase
$\varepsilon_r$	–	Total strain of the remaining phase
$\varepsilon_{el}$	–	Elastic strain
$\varepsilon_{pl}$	–	Plastic strain
$\dot{\varepsilon}_{pl}$	s <sup>-1</sup>	Plastic strain rate
$\varepsilon_{th}$	–	Thermal strain
$\varepsilon_{tr}$	–	Transformation strain
$\varepsilon_v$	–	Mises strain
$\varepsilon_{\min}$	–	Cleaning threshold strain
$\zeta$	–	Natural coordinates
$\eta$	–	Natural coordinates
$\theta$	°C	Temperature
$\dot{\theta}$	K/s	Rate of temperature change
$\theta_0$	°C	Room temperature
$\theta_M$	°C	Melting temperature

---

$\theta_i$	°C	Modified CCT transformation temperature
$\theta_\alpha$	°C	Diffusive transformation peak temperature
$\theta_{\alpha,f}$	°C	Diffusive transformation finish temperature
$\theta_{\alpha,s}$	°C	Diffusive transformation start temperature
$\theta_{\alpha',f}$	°C	Displacive transformation finish temperature
$\theta_{\alpha',s}$	°C	Displacive transformation start temperature
$\theta_\gamma$	°C	Austenitization temperature
$\theta'_\gamma$	°C	Shifted austenitization temperature
$\theta_\delta$	°C	Back transformation temperature
$\theta_\kappa$	°C	Hardening offset
$\bar{\theta}$	°C	Isothermal temperature
$\vartheta$	–	Incidence angle
$\kappa$	–	Hardening factor
$\kappa_0$	–	Hardening factor at $\theta_0$
$\lambda$	nm	X-ray wave length
$\mu$	MPa s	Effective viscosity
$\mu_0$	MPa s	Upper saturation viscosity
$\mu_\infty$	MPa s	Lower saturation viscosity
$\nu$	–	Poisson's ratio
$\xi$	–	Relative phase content
$\dot{\xi}$	s <sup>-1</sup>	Phase content change rate
$\xi_\infty$	–	Equilibrium phase content
$\xi_i$	–	Relative phase content of phase $i$
$\dot{\xi}_j$	s <sup>-1</sup>	Relative phase content change rate at time $j$
$\xi_\gamma$	–	Relative austenite content
$\xi_\alpha$	–	Relative diffusive formed phase content
$\xi_{\alpha'}$	–	Relative displacive formed phase content
$\rho$	t/mm <sup>3</sup>	Density
$\sigma_0$	MPa	Reference flow stress at $\dot{\epsilon}_0$
$\sigma_C$	MPa	Characteristic flow stress
$\sigma_H$	MPa	Plastic hardness
$\sigma_c$	MPa	Stress in the transformed phase
$\sigma_{K,i}$	MPa	Yield stress raise contributor $i$
$\sigma_r$	MPa	Stress in the remaining phase
$\sigma_r$	MPa	Radial stress
$\sigma_n$	MPa	Surface normal stress
$\sigma_v$	MPa	Mises stress
$\sigma_y$	MPa	Yield stress
$\sigma_{y,\phi}$	MPa	Yield stress of the transformed phase

---

$\sigma_{y,\psi}$	MPa	Yield stress of the untransformed phase
$\sigma_z$	MPa	Axial stress
$\sigma_\varphi$	MPa	Tangential stress
$\sigma_\alpha$	°C	Diffusive transformation exponent
$\sigma_\gamma$	1/K	Austenitization shift offset
$\tau$	MPa	Friction shear stress
$\tau$	s	Delay time
$\tau_1$	s	Austenitization start delay time
$\tau_3$	s	Austenitization finish delay time
$\tau_i$	s	Delay time for phase $i$
$\tau_\gamma$	s	Austenitization delay time
$\tau_\alpha$	s	Diffusive transformation delay time
$\tau_{\alpha'}$	s	Displacive transformation delay time
$\phi$	–	Volume fraction of transformed phases
$\varphi$	–	Angular position
$\psi$	–	Atomic concentration
$\psi$	–	Volume fraction of untransformed phases
<b>0</b>	–	Zero vector
<b>1</b>	–	Identity matrix
<b><math>B</math></b>	–	Differential operator
<b><math>C</math></b>	N/mm	Material stiffness
<b><math>D</math></b>	–	Rate of deformation
<b><math>K</math></b>	MPa	Tangent stiffness
<b><math>N</math></b>	–	Shape functions
<b><math>\Pi</math></b>	N	Force balance residuum
<b><math>b</math></b>	mm/s <sup>2</sup>	Body forces
<b><math>f_{\text{ext}}</math></b>	N	External forces
<b><math>f_{\text{int}}</math></b>	N	Internal forces
<b><math>n</math></b>	–	Surface normal
<b><math>q</math></b>	t/s <sup>3</sup>	Thermal flux
<b><math>s</math></b>	MPa	Surface tangent
<b><math>t</math></b>	MPa	Surface stresses
<b><math>u</math></b>	mm	Nodal displacements
<b><math>\ddot{u}</math></b>	mm/s <sup>2</sup>	Nodal accelerations
<b><math>u_0</math></b>	mm	Time step start displacements
<b><math>u_1</math></b>	mm	Time step end displacements
<b><math>u_e</math></b>	mm	Nodal displacements of a single element
<b><math>x</math></b>	mm	Nodal positions

$\alpha$	1/K	Thermal expansions coefficient
$\delta$	–	Volume coefficient
$\theta$	°C	Nodal temperatures
$\sigma$	MPa	Cauchy stress tensor
$\sigma'$	MPa	Deviatoric stress tensor

---

# Bibliography

- [1] D. Schmicker. “A Holistic Approach on the Simulation of Rotary Friction Welding”. Dissertation. Otto von Guericke University Magdeburg, 2015.
- [2] ISO 15620:2019. *Welding – Friction Welding of Metallic Materials*.
- [3] J. Ruge. *Handbuch der Schweißtechnik: Band II: Verfahren und Fertigung*. 3rd Edition. Springer, 1993.
- [4] B. A. Humphreys. *A Practical Guide to Friction Welding*. 2004.
- [5] C. R. G. Ellis. “Continuous Drive Friction Welding of Mild Steel”. In: *Welding Research Supplement 4* (1972), pp. 183–197.
- [6] G. Schäfer, A. Dietzel, D. Schober and S. Buchholz. *Handbuch Reibschweißen: Richtlinien für technologische Konstruktion und Anwendung*. VVB Getriebe und Kupplungen, 1976.
- [7] A. Neumann and D. Schober. *Reibschweißen von Metallen: Konstruktion, Technologie, Qualitätssicherung*. Verlag Technik, 1991.
- [8] V. I. Vill’. *Friction Welding of Metals*. American Welding Society, 1962.
- [9] M. Futamata and A. Fuji. “Friction Welding of Titanium and SUS 304L Austenitic Stainless Steel”. In: *Welding International* 4.10 (1990), pp. 768–774.
- [10] D. Schmicker, S. Paczulla, S. Nitzschke, S. Groschopp, K. Naumenko, S. Jüttner and J. Strackeljan. “Experimental Identification of Flow Properties of a S355 Structural Steel for Hot Deformation Processes”. In: *The Journal of Strain Analysis for Engineering Design* 50.2 (2015), pp. 75–83.
- [11] E. Heppner and E. Woschke. “Modelling Approach to the Microstructure Evolution in Commercially Pure Aluminium during the RFW Process”. In: *Mathematical modelling of weld phenomena 12*. TU Graz, 2019.

- [12] C. Rößler, D. Schmicker, O. Sherepenko, T. Halle, M. Körner, S. Jüttner and E. Woschke. “Identification of the Flow Properties of a 0.54% Carbon Steel during Continuous Cooling”. In: *Metals* 10.1 (2020).
- [13] L. Wang, M. Preuss, P. J. Withers, G. Baxter and P. Wilson. “Energy-Input-Based Finite-Element Process Modeling of Inertia Welding”. In: *Metallurgical and Materials Transactions B* 36.4 (2005), pp. 513–523.
- [14] P.-O. Persson and J. Peraire. “Curved Mesh Generation and Mesh Refinement using Lagrangian Solid Mechanics”. In: *47th AIAA Aerospace Sciences Meeting including The New Horizons Forum and Aerospace Exposition*. American Institute of Aeronautics and Astronautics, 2009, pp. 239–249.
- [15] D. Schmicker, P.-O. Persson and J. Strackeljan. “Implicit Geometry Meshing for the Simulation of Rotary Friction Welding”. In: *Journal of Computational Physics* 270 (2014), pp. 478–489.
- [16] D. R. Cooper and J. M. Allwood. “The Influence of Deformation Conditions in Solid-State Aluminium Welding Processes on the Resulting Weld Strength”. In: *Journal of Materials Processing Technology* 214.11 (2014), pp. 2576–2592.
- [17] N. F. Kazakov. *Diffusion Bonding of Materials*. Elsevier, 1985.
- [18] M. Ashfaq, N. Sajja, H. Khalid Rafi and K. Prasad Rao. “Improving Strength of Stainless Steel/Aluminum Alloy Friction Welds by Modifying Faying Surface Design”. In: *Journal of Materials Engineering and Performance* 22.2 (2013), pp. 376–383.
- [19] M. Sahin. “Joining of Stainless-Steel and Aluminium Materials by Friction Welding”. In: *The International Journal of Advanced Manufacturing Technology* 41.5-6 (2009), pp. 487–497.
- [20] A. P. Semenov. “The Phenomenon of Seizure and its Investigation”. In: *Wear* 4.1 (1961), pp. 1–9.
- [21] M. Plata and J. Piwnik. “Theoretical and Experimental Analysis of Seam Weld Formation in Hot Extrusion of Aluminum Alloys”. In: *Proceedings of the 7th International Aluminum Extrusion Technology Seminar*. Aluminum Association, 2000, pp. 205–212.
- [22] L. Donati and L. Tomesani. “The Prediction of Seam Welds Quality in Aluminum Extrusion”. In: *Journal of Materials Processing Technology* 153-154 (2004), pp. 366–373.

- 
- [23] M. Saby, P.-O. Bouchard and M. Bernacki. “Void Closure Criteria for Hot Metal Forming: A Review”. In: *Journal of Manufacturing Processes* 19 (2015), pp. 239–250.
- [24] Y. Zhou. *Microjoining and Nanojoining*. Woodhead Publishing, 2008.
- [25] E. Heppner, E. Woschke and S. Jüttner. *Modellentwicklung zur Vorauslegung von reibgeschweißten Aluminium-Stahl Hybridverbindungen durch ganzheitliche Abbildung der Verbindungsbildung mittels FEM*. 2019.
- [26] H. Reißner. “Eigenspannungen und Eigenspannungsquellen”. In: *Zeitschrift für Angewandte Mathematik und Mechanik* 11.1 (1931), pp. 1–8.
- [27] V. Hauk and H. Behnken. *Structural and Residual Stress Analysis by Nondestructive Methods: Evaluation - Application - Assessment*. Elsevier, 1997.
- [28] D. Radaaj. *Heat Effects of Welding: Temperature Field, Residual Stress, Distortion*. Springer, 1992.
- [29] J. P. Davim. *Machining: Fundamentals and Recent Advances*. Springer, 2008.
- [30] W. E. Nickola. “Practical Subsurface Residual Stress Evaluation by the Hole Drilling Method”. In: *Proceedings of the SEM Spring Conference on Experimental Mechanics*. Society for Experimental Mechanics, 1986, pp. 47–58.
- [31] R. Weiss. “Residual Stresses and Strength of Friction Welded Ceramic/Metal Joints”. In: *Welding Research Supplement* 3 (1998), pp. 115–122.
- [32] M. B. Prime and A. T. DeWald. “The Contour Method”. In: *Practical Residual Stress Measurement Methods*. John Wiley & Sons, 2013, pp. 109–138.
- [33] M. Preuss, P. J. Withers, J. W. L. Pang and G. J. Baxter. “Inertia Welding Nickel-Based Superalloy: Part I. Metallurgical Characterization”. In: *Metallurgical and Materials Transactions A* 33.10 (2002), pp. 3215–3225.
- [34] M. Preuss, J. W. L. Pang, P. J. Withers and G. J. Baxter. “Inertia Welding Nickel-Based Superalloy: Part II. Residual Stress Characterization”. In: *Metallurgical and Materials Transactions A* 33.10 (2002), pp. 3227–3234.
- [35] A. M. Korsunsky, G. Regino and D. Nowell. “Variational Determination of Eigenstrain Sources of Residual Stress”. In: *Proceedings of the 4th International Conference on Computational and Experimental Engineering and Science*. ICCES, 2004.

- [36] A. M. Korsunsky, T.-S. Jun and P. Road. “Eigenstrain Analysis of Residual Stresses due to Welding and Post-Weld Heat Treatment of Aerospace Materials”. In: *Proceedings of the 3rd International Conference on Processing Materials for Properties*. Curran Associates, 2009, pp. 738–743.
- [37] T.-S. Jun and A. M. Korsunsky. “Evaluation of Residual Stresses and Strains using the Eigenstrain Reconstruction Method”. In: *International Journal of Solids and Structures* 47.13 (2010), pp. 1678–1686.
- [38] B. Suthoff, H. Hentschel and A. Schaaf. “Reibschweißartige Fügung von Magnesium mit Stählen und Nichteisenmetallen”. DE 19 711 236. 1997.
- [39] F. Lai, S. Qu, Y. Duan, R. Lewis, T. Slatter, L. Yin, X. Li, H. Luo and G. Sun. “The Wear and Fatigue Behaviours of Hollow Head & Sodium Filled Engine Valve”. In: *Tribology International* 128 (2018), pp. 75–88.
- [40] M. Preuss, P. J. Withers and G. J. Baxter. “A Comparison of Inertia Friction Welds in Three Nickel Base Superalloys”. In: *Materials Science and Engineering: A* 437.1 (2006), pp. 38–45.
- [41] N. Iqbal, J. Rolph, R. Moat, D. Hughes, M. Hofmann, J. Kelleher, G. Baxter, P. J. Withers and M. Preuss. “A Comparison of Residual Stress Development in Inertia Friction Welded Fine Grain and Coarse Grain Nickel-Base Superalloy”. In: *Metallurgical and Materials Transactions A* 42.13 (2011), pp. 4056–4063.
- [42] B. Grant, M. Preuss, P. J. Withers, G. Baxter and M. Rowson. “Finite Element Process Modelling of Inertia Friction Welding Advanced Nickel-based Superalloy”. In: *Materials Science and Engineering: A* 513-514 (2009), pp. 366–375.
- [43] C. J. Bennett, T. H. Hyde and E. J. Williams. “Modelling and Simulation of the Inertia Friction Welding of Shafts”. In: *Journal of Materials: Design and Applications* 221.4 (2007), pp. 275–284.
- [44] C. J. Bennett, M. M. Attallah, M. Preuss, P. H. Shipway, T. H. Hyde and S. Bray. “Finite Element Modeling of the Inertia Friction Welding of Dissimilar High-Strength Steels”. In: *Metallurgical and Materials Transactions A* 44.11 (2013), pp. 5054–5064.
- [45] C. J. Bennett. “Finite Element Modelling of the Inertia Friction Welding of a CrMoV Alloy Steel including the Effects of Solid-State Phase Transformations”. In: *Journal of Manufacturing Processes* 18 (2015), pp. 84–91.



- 
- [46] O. Iracheta, C. J. Bennett and W. Sun. “A Sensitivity Study of Parameters affecting Residual Stress Predictions in Finite Element Modelling of the Inertia Friction Welding Process”. In: *International Journal of Solids and Structures* 71 (2015), pp. 180–193.
- [47] W. M. Gan, M. Hofmann, V. Ventzke, C. Randau, Y. D. Huang, A. Kriele, H. G. Brokmeier and M. Mueller. “Microstructure and Residual Stress in Rotary Friction Welded Dissimilar Metals of AA7020 Aluminium Alloy with 316L Steel”. In: *Materials Science Forum* 879 (2016), pp. 572–577.
- [48] J. W. Evancho and J. T. Staley. “Kinetics of Precipitation in Aluminum Alloys during Continuous Cooling”. In: *Metallurgical Transactions* 5 (1974), pp. 43–47.
- [49] P. Archambault, J. C. Chevrier, G. Beck and J. Bouvaist. “A Contribution to the Optimization of the 7075 Heat Treatment”. In: *Materials Science and Engineering* 43.1 (1980), pp. 1–6.
- [50] G. E. Totten, M. Tiryakioğlu and O. Kessler, eds. *Encyclopedia of Aluminum and its Alloys*. CRC Press, 2019.
- [51] M. Avrami. “Kinetics of Phase Change. I. General Theory”. In: *Archiv für das Eisenhüttenwesen* 7.12 (1939), pp. 1103–1112.
- [52] M. Avrami. “Kinetics of Phase Change. II. Transformation-Time Relations for Random Distribution of Nuclei”. In: *The Journal of Chemical Physics* 8.2 (1940), pp. 212–224.
- [53] M. Avrami. “Kinetics of Phase Change. III. Granulation, Phase Change and Microstructure”. In: *The Journal of Chemical Physics* 9.2 (1941), pp. 177–184.
- [54] B. Donnay, J. C. Herman, V. Leroy, U. Lotter, R. Grossterlinden and H. Pircher. “Microstructure Evolution of C-Mn Steels in the Hot Deformation Process: The Stripcam Model”. In: *Proceedings of the 2nd International Conference on Modelling of Metal Rolling Processes*. Institute of Materials, 1996, pp. 23–35.
- [55] M. Umemoto, K. Horiuchi and I. Tamura. “Pearlite Transformation during Continuous Cooling and its Relation to Isothermal Transformation”. In: *Transactions of the Iron and Steel Institute of Japan* 23.8 (1983), pp. 690–695.
- [56] E. Scheil. “Anlaufzeit der Austenitumwandlung”. In: *Archiv für das Eisenhüttenwesen* 8.12 (1935), pp. 565–567.

- [57] J. S. Kirkaldy and D. Venugopalan. “Prediction of Microstructure and Hardenability in Low Alloy Steels”. In: *Proceedings of the International Conference on Phase Transformation in Ferrous Alloys*. Metallurgical Society of AIME, 1983, pp. 125–148.
- [58] N. Saunders, Z. Guo, X. Li, A. P. Miodownik and J. P. Schillé. *The Calculation of TTT and CCT Diagrams for General Steels*. 2004.
- [59] J. B. Leblond and J. Devaux. “A New Kinetic Model for Anisothermal Metallurgical Transformations in Steels Including Effect of Austenite Grain Size”. In: *Acta Metallurgica* 32.1 (1984), pp. 137–146.
- [60] L. F. Shampine and M. W. Reichelt. “The Matlab ODE Suite”. In: *SIAM Journal on Scientific Computing* 18.1 (1997), pp. 1–22.
- [61] L. Kertsch and D. Helm. “A Thermodynamically Consistent Model for Elastoplasticity, Recovery, Recrystallization and Grain Coarsening”. In: *International Journal of Solids and Structures* 152-153 (2018), pp. 185–195.
- [62] M. Pietrzyk, Ł. Madej, L. Rauch and D. Szeliga. *Computational Materials Engineering: Achieving High Accuracy and Efficiency in Metals Processing Simulations*. Elsevier, 2015.
- [63] M. Spittel and T. Spittel. *Metal Forming Data: Ferrous Alloys*. Vol. 2C1. Advanced Materials and Technologies. Springer, 2009.
- [64] G. R. Johnson and W. H. Cook. “A Constitutive Model and Data for Metals subjected to Large Strains, High Strain Rates and High Temperatures”. In: *Proceedings of the 7th International Symposium on Ballistic*. American Defense Preparedness Association, 1983, pp. 541–545.
- [65] P. Ludwik. *Elemente der Technologischen Mechanik*. Springer, 1909.
- [66] N. Hussain, K. Khozeimeh and T. Toridis. “Inelastic Behavior of Structural Components”. In: *Research in Nonlinear Structural and Solid Mechanics*. NASA, 1980, pp. 237–250.
- [67] E. O. Hall. “The Deformation and Ageing of Mild Steel III: Discussion of Results”. In: *Proceedings of the Physical Society. Section B* 64.9 (1951), pp. 747–753.
- [68] N. Hansen. “The Effect of Grain Size and Strain on the Tensile Flow Stress of Aluminium at Room Temperature”. In: *Acta Metallurgica* 25.8 (1977), pp. 863–869.

- 
- [69] J. H. Schneibel and M. Heilmaier. “Hall–Petch Breakdown at Elevated Temperatures”. In: *Materials Transactions* 55.1 (2014), pp. 44–51.
- [70] R. Fleischer. “Solution Hardening”. In: *Acta Metallurgica* 9.11 (1961), pp. 996–1000.
- [71] R. Fleischer. “Substitutional Solution Hardening”. In: *Acta Metallurgica* 11.3 (1963), pp. 203–209.
- [72] R. Labusch. “A Statistical Theory of Solid Solution Hardening”. In: *Physica Status Solidi B* 41.2 (1970), pp. 659–669.
- [73] M. Lugovy, V. Slyunyayev and M. Brodnikovskyy. “Solid Solution Strengthening in Multiprincipal Element fcc and bcc Alloys: Analytical Approach”. In: *Progress in Natural Science: Materials International* 31.1 (2021), pp. 95–104.
- [74] G. E. Totten and R. Colas. *Encyclopedia of Iron, Steel, and their Alloys*. CRC Press, 2016.
- [75] L. Prandtl. “Über die Härte plastischer Körper”. In: *Nachrichten von der Gesellschaft der Wissenschaften zu Göttingen* (1920), pp. 74–85.
- [76] ISO 6507-1:2018. *Metallic Materials – Vickers Hardness Test – Part 1: Test Method*.
- [77] ISO 18265:2013. *Metallic Materials – Conversion of Hardness Values*.
- [78] J. R. Cahoon, W. H. Broughton and A. Kutzak. “The Determination of Yield Strength from Hardness Measurements”. In: *Metallurgical Transactions* 2.7 (1971), pp. 1979–1983.
- [79] I. Saeed. “Untersuchungen über die Streuung und Anwendung von Fließkurven”. In: *Fortschrittberichte der VDI-Zeitschriften*. VDI-Verlag, 1984, pp. 204–215.
- [80] P. A. Stathers, A. K. Hellier, R. P. Harrison, M. I. Ripley and J. Norrish. “Hardness-Tensile Property Relationships for HAZ in 6061-T651 Aluminum”. In: *Welding Journal* 93 (2014), pp. 301–311.
- [81] M. Tiryakioğlu, J. S. Robinson, M. A. Salazar-Guapuriche, Y. Y. Zhao and P. D. Eason. “Hardness-Strength Relationships in the Aluminum Alloy 7010”. In: *Materials Science and Engineering: A* 631 (2015), pp. 196–200.
- [82] A. P. Sekhar, S. Nandy, K. Kumar Ray and D. Das. “Hardness-Yield Strength Relation of Al-Mg-Si Alloys”. In: *IOP Conference Series: Materials Science and Engineering* 338 (2018).

- [83] C. Rößler. “Erstellung und Analyse eines Simulationsmodells zur Bestimmung der Eigenspannungen in reibgeschweißten Bauteilen”. Master thesis. Otto von Guericke University Magdeburg, 2015.
- [84] H. Bhadeshia. “The Bainite Transformation: Unresolved Issues”. In: *Materials Science and Engineering: A* 273-275 (1999), pp. 58–66.
- [85] L. C. D. Fielding. “The Bainite Controversy”. In: *Materials Science and Technology* 29.4 (2013), pp. 383–399.
- [86] Saarstahl. *Material Specification Sheet – C55R (Cm55)*. 2004.
- [87] D. P. Koistinen and R. E. Marburger. “A General Equation Prescribing the Extent of the Austenite-Martensite Transformation in Pure Iron-Carbon Alloys and Plain Carbon Steels”. In: *Acta Metallurgica* 7.1 (1959), pp. 59–60.
- [88] G. E. Totten, ed. *Steel Heat Treatment Handbook*. 2nd Edition. CRC Press, 2007.
- [89] R. H. Byrd, M. E. Hribar and J. Nocedal. “An Interior Point Algorithm for Large-Scale Nonlinear Programming”. In: *SIAM Journal on Optimization* 9.4 (1999), pp. 877–900.
- [90] P. Seyffarth, B. Meyer and A. Scharff. *Großer Atlas Schweiss-ZTU-Schaubilder*. DVS-Verlag, 1992.
- [91] W. Piekarska, M. Kubiak and M. Żmindak. “Issues in Numerical Modeling of Phase Transformations in Welded Joint”. In: *Procedia Engineering* 177 (2017), pp. 141–148.
- [92] J. E. Lewis, J. J. Jonas and B. Mintz. “The Formation of Deformation Induced Ferrite during Mechanical Testing”. In: *Isij International* 38.3 (1998), pp. 300–309.
- [93] H. Dong and X. Sun. “Deformation Induced Ferrite Transformation in Low Carbon Steels”. In: *Current Opinion in Solid State and Materials Science* 9.6 (2005), pp. 269–276.
- [94] X.-G. Zhou, Z.-Y. Liu, Di Wu, W. Wang and S.-H. Jiao. “Modeling of Incubation Time for Austenite to Ferrite Phase Transformation”. In: *Journal of Iron and Steel Research International* 13.4 (2006), pp. 32–34.
- [95] A. Barcellona and D. Palmeri. “Effect of Plastic Hot Deformation on the Hardness and Continuous Cooling Transformations of 22MnB5 Microalloyed Boron Steel”. In: *Metallurgical and Materials Transactions A* 40.5 (2009), pp. 1160–1174.

- 
- [96] F. Nürnberger, O. Grydin, M. Schaper, F.-W. Bach, B. Koczurkiewicz and A. Milenin. “Microstructure Transformations in Tempering Steels during Continuous Cooling from Hot Forging Temperatures”. In: *Steel Research International* 81.3 (2010), pp. 224–233.
- [97] F. Nürnberger, O. Grydin, Z. Yu and M. Schaper. “Microstructural Behaviour of Tempering Steels during Precision Forging and Quenching from Hot-Forming Temperatures”. In: *Metallurgical and Mining Industry* (2011), pp. 79–86.
- [98] J. C. Ion, K. E. Easterling and M. F. Ashby. “A Second Report on Diagrams of Microstructure and Hardness for Heat-Affected Zones in Welds”. In: *Acta Metallurgica* 32.11 (1984), pp. 1949–1962.
- [99] P. Khoral. “Coupling Microstructure to Heat Transfer Computation in Weld Analysis”. Master Thesis. Carleton University, 1989.
- [100] P. Maynier, B. Jungmann and J. Dollet. “Creusot-Loire System for the Prediction of the Mechanical Properties of Low Alloy Steel Products”. In: *Hardenability Concepts with Applications to Steel* (1978), pp. 518–545.
- [101] C. M. Sellars and W. J. M. Tegart. “Hot Workability”. In: *International Metallurgical Reviews* 17.1 (2013), pp. 1–24.
- [102] K. Naumenko and H. Altenbach. *Modeling High Temperature Materials Behavior for Structural Analysis: Part I: Continuum Mechanics Foundations and Constitutive Models*. Springer, 2016.
- [103] E. Doege, H. Meyer-Nolkemper and I. Saeed. *Fließkurvenatlas metallischer Werkstoffe*. Hanser, 1986.
- [104] M. Spittel and T. Spittel. *Metal Forming Data: Non-Ferrous Alloys – Light Metals*. Vol. 2C2. Advanced Materials and Technologies. Springer, 2011.
- [105] M. Spittel and T. Spittel. *Metal Forming Data: Non-Ferrous Alloys – Heavy Metals*. Vol. 2C3. Advanced Materials and Technologies. Springer, 2016.
- [106] D. Deng and H. Murakawa. “Influence of Transformation Induced Plasticity on Simulated Results of Welding Residual Stress in Low Temperature Transformation Steel”. In: *Computational Materials Science* 78 (2013), pp. 55–62.
- [107] G. Sachs. “Zur Ableitung einer Fließbedingung”. In: *Mitteilungen der deutschen Materialprüfungsanstalten*. Springer, 1929, pp. 94–97.

- [108] A. Reuss. “Berechnung der Fließgrenze von Mischkristallen auf Grund der Plastizitätsbedingung für Einkristalle”. In: *Zeitschrift für Angewandte Mathematik und Mechanik* 9.1 (1929), pp. 49–58.
- [109] W. Voigt. “Über die Beziehung zwischen den beiden Elastizitätskonstanten isotroper Körper”. In: *Annalen der Physik* 274.12 (1889), pp. 573–587.
- [110] K. Naumenko, H. Altenbach and A. Kutschke. “A Combined Model for Hardening, Softening, and Damage Processes in Advanced Heat Resistant Steels at Elevated Temperature”. In: *International Journal of Damage Mechanics* 20.4 (2011), pp. 578–597.
- [111] J. B. Leblond, G. Mottet and J. C. Devaux. “A Theoretical and Numerical Approach to the Plastic Behaviour of Steels during Phase Transformations – I. Derivation of General Relations”. In: *Journal of the Mechanics and Physics of Solids* 34.4 (1986), pp. 395–409.
- [112] J. B. Leblond, G. Mottet and J. C. Devaux. “A Theoretical and Numerical Approach to the Plastic Behaviour of Steels during Phase Transformations – II. Study of Classical Plasticity for Ideal-Plastic Phases”. In: *Journal of the Mechanics and Physics of Solids* 34.4 (1986), pp. 411–432.
- [113] M. E. Fine, L. D. Brown and H. L. Marcus. “Elastic Constants versus Melting Temperature in Metals”. In: *Scripta Metallurgica* 18.9 (1984), pp. 951–956.
- [114] EN 1993-1-2:2005. *Eurocode 3: Design of Steel Structures – Part 1-2: General Rules*.
- [115] EN 1999-1-1:2007. *Eurocode 9: Design of Aluminium Structures – Part 1-1: General Structural Rules*.
- [116] Z. Lütjens, V. Heuer, F. König, T. Lübben, V. Schulze and N. Trapp. “Computer Aided Simulation of Heat Treatment”. In: *HTM Härtereitechnische Mitteilungen* 61.1 (2006), pp. 10–17.
- [117] J. Winczek and A. Kulawik. “Dilatometric and Hardness Analysis of C45 Steel Tempering with Different Heating-Up Rates”. In: *Metallurgija* 51 (2012), pp. 9–12.
- [118] J. Gobrecht. *Werkstofftechnik – Metalle*. 3rd Edition. Oldenbourg, 2009.
- [119] O. C. Zienkiewicz and R. L. Taylor. *The Finite Element Method for Solid and Structural Mechanics*. 6th Edition. Butterworth-Heinemann, 2005.
- [120] P. Wriggers. *Nonlinear Finite Element Methods*. Springer, 2008.

- 
- [121] T. Belytschko, W. K. Liu, B. Moran and K. I. Elkhodary. *Nonlinear Finite Elements for Continua and Structures*. 2nd Edition. John Wiley & Sons, 2014.
- [122] H. S. Yu, G. T. Houlsby and H. J. Burd. “A Novel Isoparametric Finite Element Displacement Formulation for Axisymmetric Analysis of Nearly Incompressible Materials”. In: *International Journal for Numerical Methods in Engineering* 36.14 (1993), pp. 2453–2472.
- [123] E. Specht. *Einführung in die Vektoranalysis*. 2003.
- [124] S. K. Pascoe and J. E. Mottershead. “Linear Elastic Contact Problems Using Curved Elements and Including Dynamic Friction”. In: *International Journal for Numerical Methods in Engineering* 26.7 (1988), pp. 1631–1643.
- [125] M. Körner and S. Jüttner. *Entwicklung eines Reibgesetzes zur Erfassung des Drehzahleinflusses bei der Reibschweißprozesssimulation*. 2018.
- [126] H. Hügel and T. Rudlaff. *Arbeiten zur Optimierung des Umwandlungshärtens mit Laserstrahlen*. Vieweg & Teubner, 1993.
- [127] Y. Yagi. “Friction Welding Method”. US 4 087 038. 1978.
- [128] H. Steinmetz, R. Reinhardt and F. Trommer. “Aufgleitendes Reibschweißen eröffnet neue Anwendungsgebiete im Automobilbau”. In: *19. Erfahrungsaustausch Reibschweißen*. SLV München, 2011.
- [129] S. Mohammadzadeh Polami, R. Reinhardt, M. Rethmeier and A. Schmid. “Joint-Site Structure Friction Welding Method as a Tool for Drive Pinion Light Weighting in Heavy-Duty Trucks”. In: *Journal of Materials Processing Technology* 214.9 (2014), pp. 1921–1927.
- [130] S. Mohammadzadeh Polami. “Alternative Production Methods for Drive Pinion in Heavy Duty Trucks”. Dissertation. TU Berlin, 2015.
- [131] R. Reinhardt. “50 Jahre Reibschweißen bei Daimler – eine Erfolgsgeschichte”. In: *22. Erfahrungsaustausch Reibschweißen*. SLV München, 2017.
- [132] P. Marter, P. Seidler, H. Kriese, A. Krüger and D. Schmicker. “Advanced Friction Welding Applications at IFA”. In: *23. Erfahrungsaustausch Reibschweißen*. SLV München, 2019.
- [133] D. Schmicker, M. Kreibich, F. Trommer and A. Krüger. “Components to be Connected by Friction Welding with a Joint-Site Structure and Method of Connecting Components by Means of Friction Welding”. EP 3 241 642. 2017.

- [134] Saarstahl. *Material Specification Sheet – 25CrMo4*. 2004.
- [135] P. Suwanpinij, N. Togobytsk, C. Keul, W. Weiss, U. Prahl, D. Hömberg and W. Bleck. “Phase Transformation Modeling and Parameter Identification from Dilatometric Investigations”. In: *Steel Research International* 79.10 (2008), pp. 793–799.
- [136] J. Spörer, H. Stimpel, J. Götz, S. Kirmse and G. Blechinger. “Method for Manufacturing a Brake Disc”. EP 1 128 083. 2001.
- [137] H. Zametica, J. Schmitz and I. Hoffmann. “Brake Disc and Method for its Manufacture”. EP 2 249 055. 2010.
- [138] F. Füllgrabe. “Neue Konzepte für Leichtbau-Bremsscheiben auf Basis metallischer Werkstoffe”. Dissertation. TU Darmstadt, 2012.
- [139] EN 1561:2011. *Founding – Grey Cast Irons*.
- [140] GSI SLV. *Internationaler Schweißfachingenieurlehrgang*. 2008.
- [141] H. Kreye. *Gefüge und Eigenschaften von Reibschweißverbindungen aus Stahl/Stahl und Stahl/NE-Metallen*. 1986.
- [142] H. Grünauer. *Reibschweißen von Metallen*. Expert Verlag, 1987.
- [143] C. Tasdemir. “Investigations for Joining Aluminum Chill Casting using Inertia Friction Welding”. Dissertation. RWTH Aachen University, 2019.
- [144] C. Rößler, D. Schmicker, K. Naumenko and E. Woschke. “Adaption of a Carreau Fluid Law Formulation for Residual Stress Determination in Rotary Friction Welds”. In: *Journal of Materials Processing Technology* 252 (2017), pp. 567–572.
- [145] Special Metals. *Data Sheet Inconel Alloy 718SPF*. 2007.
- [146] D. Basak, R. A. Overfelt and D. Wang. “Measurement of Specific Heat Capacity and Electrical Resistivity of Industrial Alloys Using Pulse Heating Techniques”. In: *International Journal of Thermophysics* 24.6 (2003), pp. 1721–1733.



## A Material matrices

The full material stiffness matrix

$$\mathbf{C} = \frac{E}{(1+\nu)(1-2\nu)} \begin{bmatrix} 1-\nu & \nu & \nu & 0 & 0 & 0 \\ & 1-\nu & \nu & 0 & 0 & 0 \\ & & 1-\nu & 0 & 0 & 0 \\ & & & 1-2\nu & 0 & 0 \\ \text{sym.} & & & & 1-2\nu & 0 \\ & & & & & 1-2\nu \end{bmatrix}$$

which depends on the elastic modulus  $E$  and the Poisson's ratio  $\nu$ , links the stress vector

$$\boldsymbol{\sigma} = \left[ \sigma_r \quad \sigma_z \quad \sigma_\varphi \quad \sigma_{z\varphi} \quad \sigma_{r\varphi} \quad \sigma_{rz} \right]^T$$

to the elastic part of the strain vector

$$\boldsymbol{\varepsilon} = \left[ \varepsilon_r \quad \varepsilon_z \quad \varepsilon_\varphi \quad \varepsilon_{z\varphi} \quad \varepsilon_{r\varphi} \quad \varepsilon_{rz} \right]^T .$$

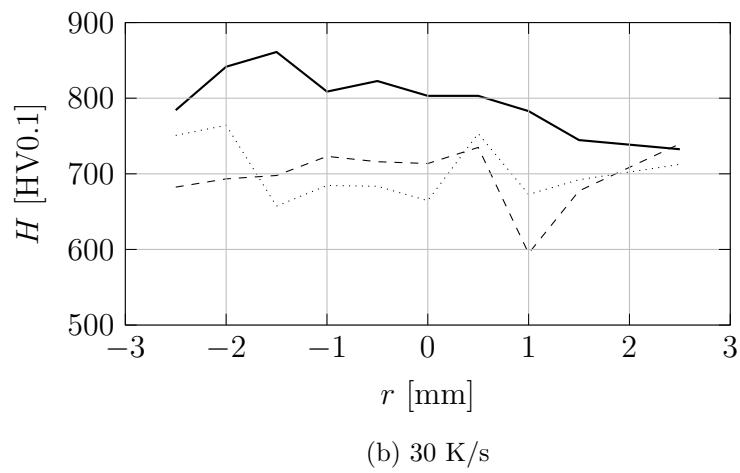
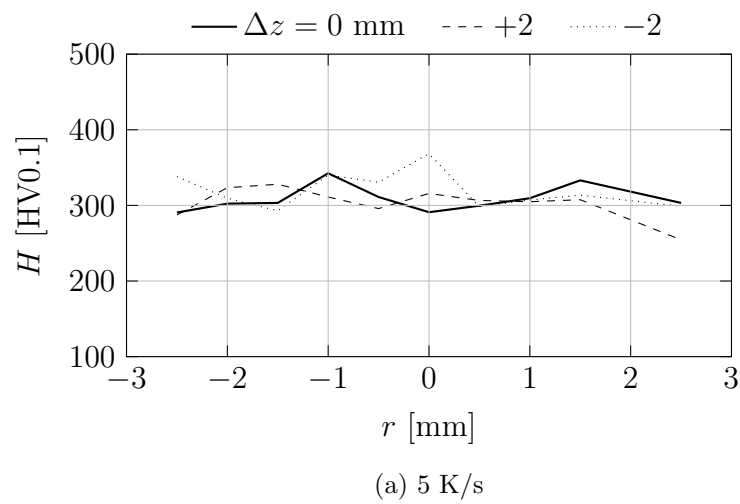
## B Hardness composition

The table contains the phase hardnesses identified from the CCT diagram as best-fitting for the overdetermined linear system and calculated with Maynier formulas based on the chemical composition.

Model		CCT	Maynier
$H_{F,P,A}$	[HV]	250	208
$H_B$	[HV]	250	252
$H_M$	[HV]	710	714

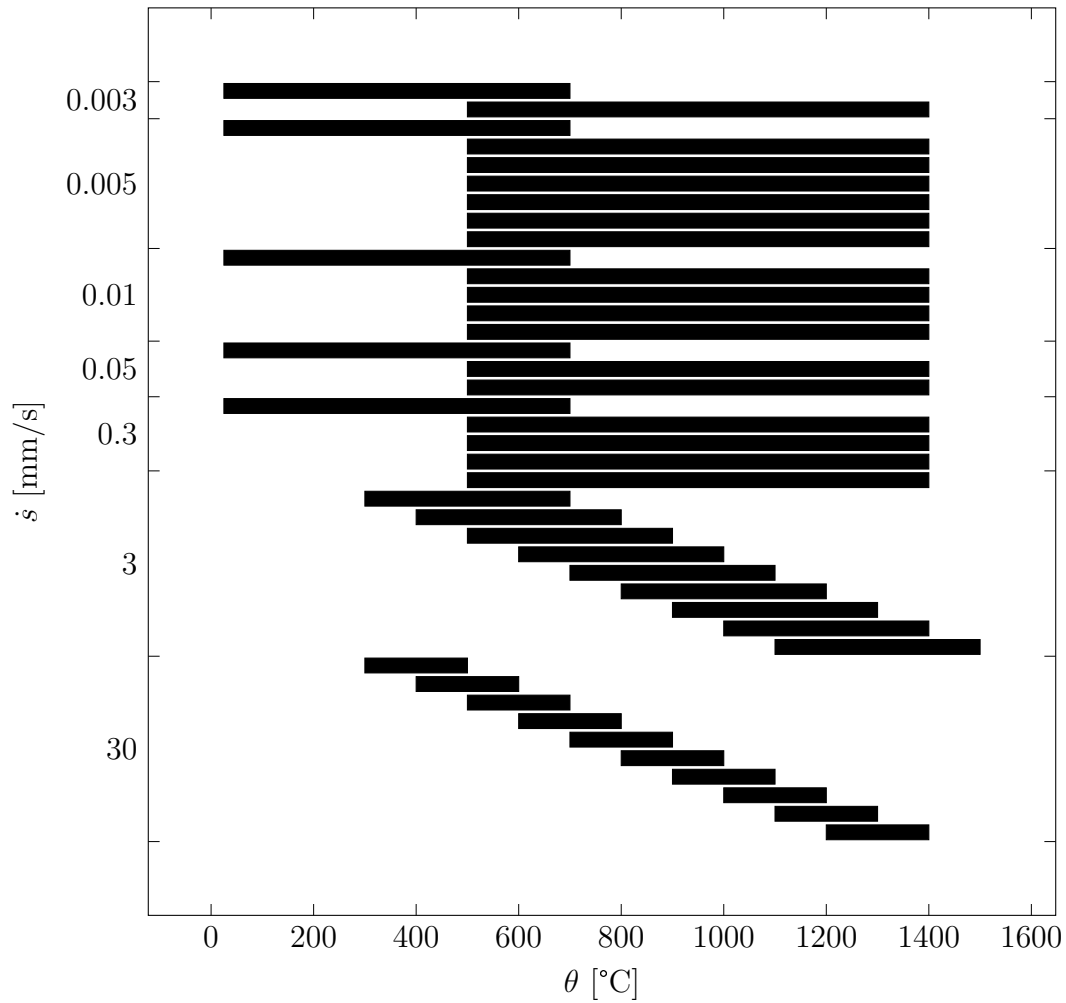
## C Hardness distribution

Both plots show the hardness measurements in the cross sections at room temperature after cooling down with 5 K/s and 30 K/s.

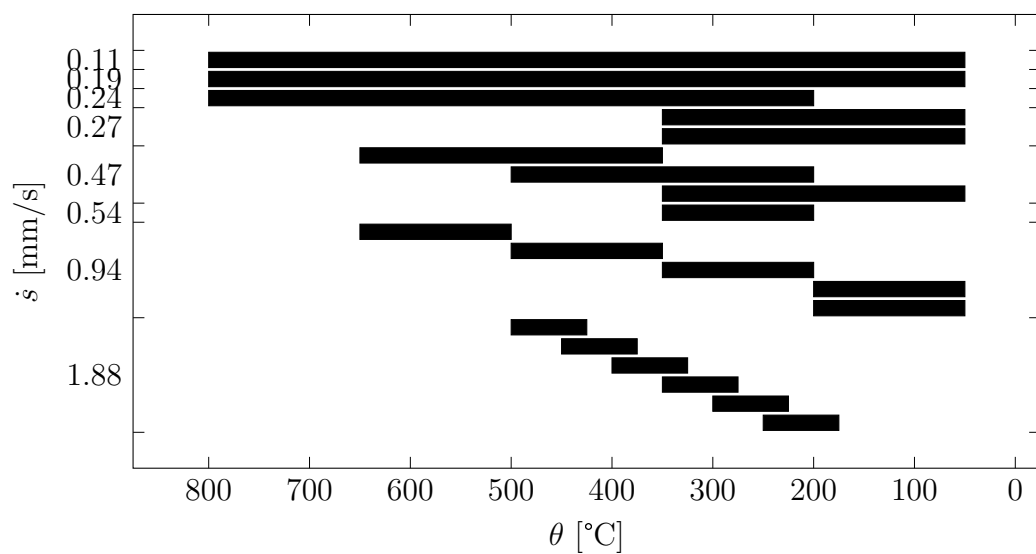


## D Hot tensile testing

The examined temperature and stroke ranges in the hot tensile tests are visualized below.



(c) Heating



(d) Cooling, 30 K/s

## E Flow stress properties

The experimentally determined flow properties for  $\dot{\epsilon}_0 = 0.001 \text{ s}^{-1}$  for the investigated carbon steel are presented as tabulated data in the following.

$\theta$ [°C]	Heating		Cooling			
	$\sigma_0$ [MPa]	$n$ [-]	5 K/s		30 K/s	
			$\sigma_0$ [MPa]	$n$ [-]	$\sigma_0$ [MPa]	$n$ [-]
200	–	–	–	–	440.4	4.13
250	–	–	728.3	13.26	315.7	3.88
300	774.3	32.93	706.8	13.03	232.8	3.69
350	774.3	32.93	670.3	12.64	215.1	3.64
400	759.3	32.01	648.4	12.41	196.4	3.59
450	669.9	27.16	530.6	11.19	165.9	3.49
500	523.3	20.90	399.8	9.82	129.9	3.36
550	381.1	16.14	274.0	8.44	102.8	3.24
600	285.0	13.35	178.9	7.28	84.6	3.15
650	207.0	11.21	118.6	6.43	68.8	3.06
700	147.1	9.58	93.1	6.02	56.0	2.98
750	97.2	8.14	74.6	5.68	46.0	2.90
800	73.0	7.37	56.9	5.32		
850	59.6	6.91				
900	48.6	6.50				
950	39.4	6.13				
1000	32.7	5.83				
1050	26.5	5.53				
1100	22.0	5.29				
1150	18.4	5.08				
1200	17.0	4.98				
1250	13.5	4.74				
1300	10.1	4.47				